Doctoral Dissertation (Censored)

博士論文（要約）

A comprehensive study on seasonal variations of low-level clouds and associated air-sea interactions in the South Indian Ocean

（南インド洋上の下層雲の季節変動とそれに関わる大気海洋相互作用の包括的研究）

A Dissertation Submitted for the Degree of Doctor of Philosophy

December 2019

令和元年１２月博士（理学）申請

Department of Earth and Planetary Science, Graduate School of Science,
The University of Tokyo

東京大学大学院理学系研究科地球惑星科学専攻

Ayumu Miyamoto

宮本　歩

Abstract

Low-level clouds strongly cool the earth as they reflect a large fraction of insolation while emitting longwave radiation nearly as much as the earth's surface. Since their formation is governed by small-scale turbulent processes and microphysics, however, low-level clouds are not well represented in global climate models, introducing uncertainties into future climate projections. Climatologically, low-level clouds prevail over the eastern portion of the basins, and several studies suggested the active roles of such low-level clouds on the maintenance of subtropical highs through their albedo effect and/or longwave radiative cooling from their cloud-top.

The present study focuses on the South Indian Ocean. The subtropical high resides over the eastern portion of the basin in summer, while it strengthens and shifts westward in winter. Correspondingly, the area of large low-cloud fraction (LCF) over the South Indian Ocean also shows westward extension from summer. Such distinct seasonality of the subtropical high and low-level clouds cannot be seen in the other subtropical ocean basins. In addition, there is a prominent sea surface temperature (SST) front along the Agulhas Return Current in the South Indian Ocean (hereafter referred to as the Agulhas SST front). The associated cross-frontal gradient of surface sensible heat flux (SHF) maintains a surface baroclinic zone, forming a storm track. Thus the storm-track activity in the

South Indian Ocean is active throughout the year, and maximized in winter. Furthermore, the Asian summer monsoon located to the north, which is one of the strongest seasonal variations in the Earth, may affect the subtropical high in the South Indian Ocean remotely in austral winter. Considering those intriguing points, however, the coupling between the subtropical high and low-level clouds via SST as well as its modulation by the storm-track activity maintained by the Agulhas SST front and the Asian summer monsoon in austral summer have not been assessed yet. The present study elucidates those by using satellite observations and a series of dynamical and general circulation model experiments.

In summer, we have found that low-level clouds are essential for the maintenance of the subtropical high. Our sensitivity experiments with a coupled general circulation model (CM2.1) confirmed that low-level clouds reinforce the summertime subtropical high ($\sim +5$ hPa) so that the high as the planetary wave component would almost vanish without the radiative effects of the subtropical low-level clouds. During the warm season, the albedo effect of low-level clouds strongly lowers SST under the strong summertime insolation, especially in the eastern portion of the basin (~ -4 °C in the CM2.1 experiments). The lowered SST hinders the southward displacement (or expansion) of the intertropical convergence zone (ITCZ), reducing precipitation from deep clouds in the equatorward portion of the subtropical South Indian Ocean. The anomalous diabatic cooling associated with the reduced precipitation induces an anticyclonic response to its southwest, reinforcing the surface subtropical high. Our dynamical model experiments have elucidated that the reinforcement through the anomalous condensation heating is predominant in the feedback from low-level clouds. The high is also modestly reinforced by the augmented in-atmosphere radiative cooling, which is attributable to the reduced longwave radiative heating by high-level clouds associated with the reduced deep convection as well as the cloud-top longwave cooling from low-level clouds. The dynamical model experiments with individual diabatic heating component taken from an atmospheric reanalysis data (JRA-55) have also confirmed the predominance of the reduced precipitation for the maintenance of the high as the planetary wave component. Still, the shallow cooling-heating couplet between the cool South Indian Ocean and the heated Australian continent acts to suppress deep convection by invoking surface divergence and alongshore winds, which act to lower SST by enhanced evaporation, upper-ocean mixing, coastal upwelling and weakening of the Leeuwin Current off the west coast of Australia. The analysis has also revealed that forcing from sub-monthly eddies as well as remote influences from the tropics is negligible for the maintenance of the summertime subtropical high over the South Indian Ocean.

In winter, the westward-shifted subtropical high contributes to the wintertime enhancement and westward expansion of low-cloud cover by invoking the mid-tropospheric subsidence, which enhances lower-tropospheric stability, and the southeasterly Trades, which enhance upward SHF, both across the entire subtropical basin. Our sensitivity experiments with CM2.1 have elucidated that those low-level clouds feed back onto the equatorward portion of the subtropical high ($\sim +1.5$ hPa) through augmenting cloud-top longwave cooling. They also reinforce the high modestly through the reduced turbulent heating associated with the lowered SST. In contrast to the summertime case, suppression of deep convection by low-level clouds is weak, leading to a smaller contribution to the maintenance of the high. This is probably because the reduced lowering of SST ($\sim -2\,^{\circ}$C) due to the weaker cloud radiative forcing under reduced wintertime insolation along with climatologically low SST and the enhanced winter-hemisphere Hadley cell, suppressing precipitation even in the absence of low-level clouds. Nevertheless, it has been demonstrated that there exists a coupling between the subtropical high and low-level clouds also in winter.

This study has also revealed the modulations of the aforementioned coupling by the seasonally enhanced storm-track activity maintained by the Agulhas SST front. We have shown that the enhanced storm-track activity maintained by the Agulhas SST front is also important for the enhanced LCF, because migratory synoptic-scale eddies along the storm track augment upward SHF by enhancing cold advection over the warmer side of the wintertime subtropical SST front located at $\sim$30°S and increasing the climatological-mean scalar wind speed where climatological-mean southerlies are weak (25°S-30°S). This is presumably one of the reasons why SHF emerges as an important cloud-controlling factor for the seasonal cycle of LCF in the subtropical South Indian Ocean. The storm-track activity is even more important for the maintenance of the poleward portion of the subtropical high through the convergences of eddy heat and vorticity fluxes and the resultant acceleration of the climatological-mean westerlies on the poleward side of the high, as shown by the dynamical model experiments. The atmospheric general circulation model experiments further indicate that the Agulhas SST front acts to reinforce the high by energizing the storm-track activity.

The dynamical model experiments have also revealed that unlike in austral summer, the coupled system can be modulated by the remote influence from the tropics, especially the Asian summer monsoon region. The enhanced deep convection over the Asian summer monsoon region as well as the equatorial eastern Indian Ocean and western

Pacific acts not only to shift the subtropical high westward but also to enhance mid-tropospheric subsidence and equatorward surface winds over the central and western portions of the subtropical South Indian Ocean. The induced subsidence acts to stabilize and dry the free troposphere, and the equatorward surface winds yield near-surface cold advection, both of which are favorable for the low-level cloud formation but unfavorable for the development of deep precipitating clouds. The resultant enhanced radiative cooling and reduced deep condensation heating can further reinforce the surface subtropical high.

Thus the present study has assessed the impacts of low-level clouds on the subtropical high and their seasonality in the South Indian Ocean quantitatively, deepening the understanding of the coupling between the subtropical high and low-level clouds. The present study has also indicated that the storm-track activity energized by the Agulhas SST front contributes to the maintenance of the wintertime subtropical high and low-level clouds, and that the deep convection around the Asian summer monsoon region as well as the equatorial Indian Ocean and western Pacific facilitates the westward shift and strengthening of the subtropical high in austral winter, elucidating the mechanisms of the distinct seasonality of the subtropical high and low-level clouds in the South Indian Ocean.

Contents

Chapter 1

General introduction

1.1 Current understanding

a Low-level clouds

Low-level clouds strongly cool the Earth as they reflect a large fraction of insolation while emitting longwave radiation nearly as much as the Earth's surface (Hartmann and Short 1980). In fact, a small change in fractional coverage of low-level clouds could offset the anthropogenic global warming (Randall 1984). Since their formation is governed by small-scale turbulent processes and microphysics, however, low-level clouds are not well represented in global climate models, introducing uncertainties into future climate projections (e.g., Bony and Dufresne 2005; Qu et al. 2014, 2015; Myers and Norris 2016). Thus understanding how the properties of low-level clouds are determined is a fundamental issue in climate science.

Climatologically, low-level clouds are frequently observed over cool oceans, where deep convection is unlikely to occur. For example, stratocumulus clouds prevail over the eastern portion of each of the subtropical ocean basins (e.g., Klein and Hartmann 1993; Wood 2012), which is located east of a surface subtropical high that accompanies persistent mid-tropospheric subsidence and equatorward surface winds (e.g., Miyasaka and Nakamura 2005, 2010). The equatorward winds induce coastal upwelling and upper-ocean mixing in addition to surface evaporation, acting to maintain relatively low sea surface temperature (SST) (e.g., Seager et al. 2003). Owing to their high albedo, those stratocumulus clouds also act to cool the ocean. Combination of the low SST and enhanced mid-tropospheric subsidence, which acts to warm the free troposphere, maintains a strong temperature inversion at the top of the boundary layer, inhibiting cloud-top entrainment of dry air. In fact, the temperature inversion can explain seasonality of low-cloud fraction (LCF) in the eastern portion of a subtropical ocean basin (Klein and Hartmann 1993; Wood and Bretherton 2006). Those equatorward surface winds yield cold advection, thus destabilize the surface layer, and thereby facilitate shallow convection in the boundary layer, to further increase LCF.

Other regions of large LCF are found over the mid-latitude/subpolar oceans, where not only stratocumulus but also fog and stratus are frequently observed (Norris 1998; Koshiro and Shiotani 2014). As typically observed in the eastern subtropics, cold air advection near the surface is favorable for stratocumulus formation. The occurrence of fog and stratus is, by contrast, more likely under warm advection that renders surface air temperature (SAT) higher than SST underneath (Norris and Klein 2000; Norris and Iacobellis 2005; Tokinaga et al. 2009; Tanimoto et al. 2009; Koshiro et al. 2017). It has been shown that seasonal-mean LCF can be explained well by lower-tropospheric stability (Klein and Hartmann 1993; Wood and Bretherton 2006; Koshiro and Shiotani

2014).

While previous studies have revealed large-scale controls on low-level clouds, those clouds can feed back onto large-scale conditions. Although the feedback can occur with various climatic phenomena, there are basically two mechanisms in which low-level clouds act on “local” large-scale conditions. One mechanism is shielding effect of low-level clouds owing to their high albedo. Low-level clouds strongly reflect sunlight, lowering SST underneath. Lowered SST in turn acts to increase lower-tropospheric stability, thereby enhancing LCF to constitute a positive low-cloud-SST feedback (e.g., Norris and Leovy 1994; Norris et al. 1998; Clement et al. 2009). This positive feedback is one-dimensional in terms of large-scale conditions. However, lowered SST may drive anomalous large-scale atmospheric circulation, making the feedback three-dimensional. The other mechanism is in-atmosphere longwave radiative cooling from the cloud top, which is necessary for maintaining the cloud layer by destabilizing the boundary layer (Lilly 1968). The cooling can also force large-scale atmospheric circulation (e.g., Nigam 1997; Miyasaka and Nakamura 2005, 2010).

Previous studies have discussed the possible climatological impacts of low-level clouds on large-scale atmospheric circulation. Particularly, many studies have paid attention to low-level clouds in the South Pacific and Atlantic, in connection with the intertropical convergence zone (ITCZ), which tends to be located in the Northern Hemisphere under the equatorially symmetric insolation at the top of the atmosphere (TOA). It has been shown that low-level clouds are key to keep the ITCZ north of the equator in coupled models (Philander et al. 1996; Ma et al. 1996; Yu and Mechoso 1999; Gordon et al. 2000; Xie et al. 2007), since the albedo effect of low-level clouds yields equatorial asymmetries in the SST field, triggering the wind-evaporation-SST (WES) feedback (Xie and Philander 1994; Philander et al. 1996). Radiative cooling from those low-level clouds can also play a role in the seasonal cycle of wind and precipitation systems (Nigam 1997), although the reinforcement of precipitation in the ITCZ in the Northern Hemisphere is relatively weak without any air-sea coupling processes (Wang et al. 2005). There are also several studies that suggest impacts of low-level clouds on the climatological subtropical highs away from the equator through cloud-top radiative cooling as well as their albedo effect (Rodwell and Hoskins 2001; Seager et al. 2003; Miyasaka and Nakamura 2005, 2010), although those impacts are not fully quantified yet. Details of such discussions are given in the next subsection.

Coupling of low-level clouds with the large-scale climate system over the equatorial and subtropical oceans can also occur in interannual and decadal variations. Bellomo et al. (2014, 2015) artificially enhanced the cloud-SST feedback by changing cloud water content as a function of anomalous SST underneath in the radiation calculations in an atmospheric general circulation model (AGCM) coupled with a slab ocean model. They found that stronger and more prolonged SST anomalies in the eastern subtropical oceans generated under the enhanced positive low-cloud feedback can propagate equatorward via the WES feedback in the South Pacific and Atlantic, enhancing equatorial SST variability. They also found that the impact of the augmented positive cloud feedback is limited to the north of the ITCZ in the North Pacific. Rädel et al. (2016) showed that interaction of large-scale circulations and clouds through radiation amplifies El Niño/Southern Oscillation (ENSO) by a factor of two or three in a climate model. Specifically, anomalous longwave cooling from low-level clouds contributes positively to the anomalous Walker circulation, strengthening the positive Bjerknes feedback along with anomalous longwave heating by high-level clouds.

Impacts of low-level clouds on the midlatitude/subpolar oceans have gained less attention until recently. Previous studies (e.g., Trenberth and Fasullo 2010; Grise et al. 2015) pointed out that many of the global climate models have large biases in shortwave radiation over the Southern Ocean, which can possibly affect the atmospheric circulations including the ITCZ and/or eddy-driven jet via SST distribution (Frierson and Hwang 2012; Hwang and Frierson 2013; Ceppi and Hartmann 2015). Although the biases are attributable mainly to the phase of clouds in the models (e.g., Senior and Mitchell 1993; Tsushima et al. 2006; Komurcu et al. 2014; McCoy et al. 2015b, 2016; Tan et al. 2016; Ceppi et al. 2016a; Bodas-Salcedo et al. 2016), those results imply that radiative effect of low-level clouds has the potential to affect the large-scale atmospheric circulation in the extratropics. In fact, a few studies directly assessed the influence of low-level clouds on the atmosphere over the midlatitude/subpolar oceans. Koseki et al. (2012) showed that summertime low-level clouds in the cool Okhotsk Sea locally enhance the surface high (Okhotsk high) through radiative cooling in a regional atmospheric model. Some studies removed the radiative effects of clouds in the entire troposphere and then discussed the resultant changes in eddy-driven westerly jets in AGCMs (Li et al. 2015; Watt-Meyer and Frierson 2017). For high-frequency variability, Grise et al. (2019) showed through an AGCM experiment that in-atmosphere radiative cooling in migratory extratropical storms slightly damps the storm-track activity through increased static stability. Meanwhile, low-level clouds that form under the cold advection and descent behind a cold front act to augment radiative cooling.

b Subtropical high

Over each of the subtropical ocean basins, there is a surface subtropical high, which can be regarded as the superposition of the zonal-mean Hadley circulation (e.g., Dima and Wallace 2003) and zonally asymmetric planetary waves (e.g., Rodwell and Hoskins 2001; Miyasaka and Nakamura 2005, 2010; Fig. 1.1). The high not only affects the surrounding atmospheric conditions but also drives an oceanic subtropical gyre, forming a warm western boundary current (e.g., the Kuroshio, Gulf Stream, or Agulhas Current) and cool eastern boundary current (e.g., the Canary, California, Peru or Benguela Current). As discussed in Section 1.1a, the equatorward winds associated with a subtropical high induce coastal upwelling and upper-ocean mixing in addition to surface evaporation, acting to maintain relatively low SST (e.g., Seager et al. 2003) and thus to promote low-cloud cover (e.g., Klein and Hartmann 1993).

Regarding their formation and maintenance mechanisms, previous studies mainly focused on the summertime subtropical highs because they tend to be stronger and zonally more asymmetric (Miyasaka and Nakamura 2005; 2010; Nakamura et al. 2010), especially in the Northern Hemisphere (Fig. 1.1). Thus their formation and maintenance mechanisms are discussed in the context of planetary waves, rather than the theory of zonal-mean Hadley circulation that predicts weaker subsidence in the summer hemisphere than the winter hemisphere (Lindzen and Hou 1998; Dima and Wallace 2003). Using a planetary wave model that only solves time evolution of zonally asymmetric components, Rodwell and Hoskins (2001) argued that summertime monsoonal heating east of each surface subtropical high forces adiabatic descent, enhancing local diabatic cooling to form the high. This argument is an extension of the "monsoon-desert" mechanism proposed by

Rodwell and Hoskins (1996). The adiabatic descent thus forced requires equatorward winds under the Sverdrup balance[1], which accompany near-surface cold advection over the eastern portion of the basin. Thus the induced equatorward winds act to cool the eastern subtropical ocean by facilitating turbulent heat loss, upper-ocean mixing and coastal upwelling (e.g., Seager et al. 2003).

Using the same model as in Rodwell and Hoskins (2001), Miyasaka and Nakamura (2005) showed that lower-tropospheric thermal contrast between the cool ocean under a subtropical high and the heated continent to the east under strong summertime insolation is more important as the direct diabatic forcing than the remote forcing by monsoonal heating for the formation of summertime subtropical highs. They also attributed the maritime cooling to cloud-top radiative cooling from low-level clouds, claiming the importance of low-level clouds on the maintenance of the subtropical highs. Figure 1.2 shows a schematic illustration of the local feedback loop for the formation of summertime subtropical highs proposed by Miyasaka and Nakamura (2005). Enhanced insolation toward summer initiates surface thermal contrast between the heated landmass and the relatively cool ocean. The surface thermal contrast accompanies the maritime high and the continental low (Hoskins et al. 1985) between which equatorward alongshore winds and associated surface divergence exist under the Sverdrup balance. The alongshore winds and surface divergence are favorable for maritime stratus clouds, which strengthen the thermal contrast by enhancing radiative cooling over the ocean. Thus they argued that although the monsoon-desert mechanism (Rodwell and Hoskins 1996) may help maintain the dryness of the western portion of the continents and thereby setting fundamental

---

[1] The Sverdrup vorticity balance can be written as $\beta v \approx f \partial\omega/\partial p$ where p is pressure, ω is vertical velocity, v is meridional wind, f is the Coriolis parameter, and β is its meridional gradient.

zonal asymmetries in the diabatic heating distribution after the monsoon onset, the summertime subtropical highs can essentially be interpreted in the framework of local atmosphere-ocean-land interactions (Nakamura 2012). This idea was further extended to the subtropical highs in the Southern Hemisphere (Miyasaka and Nakamura 2010).

In the winter hemisphere, a subtropical high shows zonally more symmetric structure (i.e., weaker highs as the planetary waves; Fig. 1.1; Rodwell and Hoskins 2001) with enhanced contribution from the zonal-mean Hadley circulation (Lindzen and Hou 1988; Dima and Wallace 2003). For the planetary wave component superposed on the zonal-mean Hadley circulation, Rodwell and Hoskins (2001) argued that nonlinear interaction between orography and zonal-mean circulations may force the subsidence to enhance the oceanic subtropical highs. Nakamura et al. (2010) showed that Rossby wave propagation acts to reinforce subtropical highs in the wintertime Northern Hemisphere. They added that feedback forcing from transient eddies is also important for the maintenance of the Azores high, the subtropical high in the North Atlantic. By comparing two versions of an AGCM, Richter et al. (2008) reported that improvement of precipitation distribution over the African continent can reduce a location bias of the subtropical high in the South Atlantic, implying the possibility of remote influence from the tropics. The existence of the remote influence from the tropics was also argued by Lee et al. (2013). By artificially changing the insolation over the Northern Hemisphere, they showed that changes in precipitation in the equatorial region can affect the wintertime subtropical highs in the Southern Hemisphere through Rossby wave teleconnection.

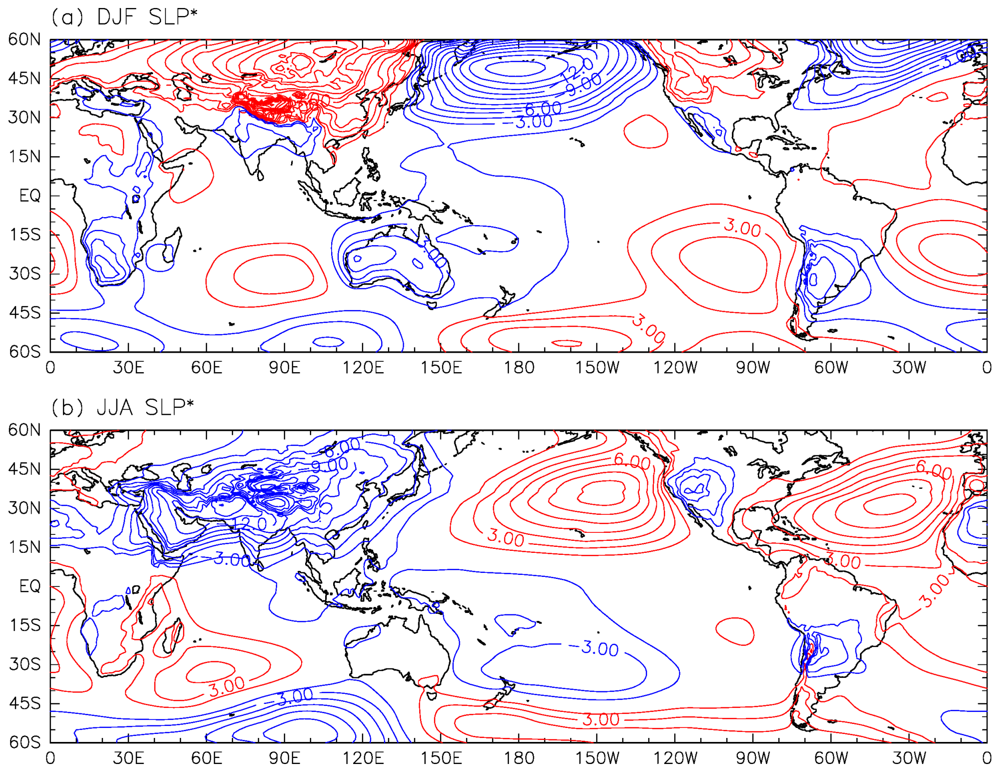

Figure 1.1: Climatological-mean zonally asymmetric SLP (contoured for every 1.5 hPa; red and blue lines for positive and negative values, respectively; zero contours are omitted) in (a) DJF and (b) JJA based on JRA-55 for the 1979-2018 period.

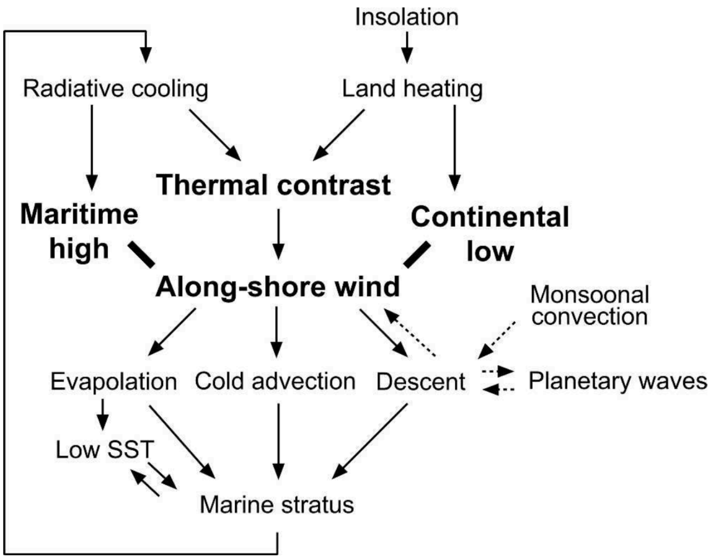

Figure 1.2: Schematic diagram showing a feedback system associated with a surface subtropical high. Solid lines indicate a local feedback loop associated with the high, whereas dashed lines indicate possible remote triggering processes. Adapted from Miyasaka and Nakamura (2005).

1.2 Purpose of this study

Despite the strong correlation between climatological-mean LCF and lower-tropospheric static stability as shown by Klein and Hartmann (1993) and subsequent studies (Wood and Bretherton 2004; Koshiro and Shiotani 2014), modelling and observational studies have revealed several environmental conditions, including the stability, that can influence low-level clouds, which is often called “cloud-controlling factors” (Kamae et al. 2016; Klein et al. 2017). In fact, not only lower-tropospheric stability but also SST is important for the response of LCF to global warming (Qu et al. 2014, 2015). Taking advantage of the accumulated knowledge of cloud-controlling factors thus far, we can reconsider whether lower-tropospheric stability alone can fully explain the climatological-mean distribution of LCF and its seasonality. If not, identifying other important cloud-controlling factors is of particular significance because such large-scale circulation features as subtropical highs or storm-track activity control LCF is useful information for disentangling interactions between low-level clouds and large-scale atmospheric circulation as well as their interaction on the underlying ocean.

Furthermore, several studies (e.g., Seager et al. 2003; Miyasaka and Nakamura 2005, 2010) implied the active roles of low-level clouds on the maintenance of subtropical highs by lowering of SST and/or enhancing cloud-top radiative cooling. Still, there have been few studies that assess the feedback from low-level clouds on the climatological-mean subtropical highs quantitatively and comprehensively. Although several studies (e.g., Philander et al. 1996; Ma et al. 1996; Yu and Mechoso 1999; Gordon et al. 2000; Xie et al. 2007) investigated the impacts of low-level clouds off the Peruvian coast, their focus is on the role of low-level clouds as a driver of the WES feedback and thereby their impacts on precipitation associated with the ITCZ. Thus the atmospheric circulation system away from the ITCZ have not been discussed thoroughly.

In this study we focus on the South Indian Ocean, where the surface subtropical Mascarene high exhibits a distinct seasonality from its counterpart in other ocean basins (Figs. 1.3a,d; Rodwell and Hoskins 2001; Lee et al. 2013). The Mascarene high resides over the eastern portion of the basin in summer (Fig. 1.3a), while it strengthens and shifts westward in winter (Fig. 1.3d). Correspondingly, the area of large LCF over the South Indian Ocean also shows westward extension from summer (Figs. 1.3a,d). Over each of the South Atlantic and Pacific, by contrast, the subtropical high resides over the eastern portion of the basin throughout the year, and thus such westward extension of a large LCF area into winter as seen over the South Indian Ocean is not apparent. Still, the seasonality of low-level clouds over the South Indian Ocean has not been examined in detail. In fact, the Mascarene high is the sole subtropical high that strengthens and shifts westward in winter as the planetary wave component (Fig. 1.1). While Nakamura et al. (2010) discussed the wintertime subtropical highs in the Northern Hemisphere, structure and maintenance mechanisms for the wintertime Mascarene high have not been investigated yet.

Another important factor that characterizes the South Indian Ocean is a prominent oceanic front that forms in the confluent zone of the warm Agulhas Return Current and cool Antarctic Circumpolar Current (Figs. 1.3c,f). This midlatitude oceanic front extends nearly zonally around 45°S from 20°E to 90°E and is characterized by pronounced SST gradient (hereafter referred to as the Agulhas SST front). It has been shown that this prominent SST front acts to maintain a surface baroclinic zone locally and thereby anchors a storm track along which migratory cyclones and anticyclones recurrently develop (Nakamura and Shimpo 2004; Nakamura et al. 2008; Nonaka et al. 2009; Hotta and Nakamura 2011). Sub-weekly fluctuations in surface winds associated with migratory cyclones and anticyclones act to relax the SAT gradient around the SST front, yielding cross-frontal gradient of surface sensible heat flux (SHF) (Nonaka et al. 2009; Hotta and Nakamura 2011). In fact, sub-weekly fluctuations in surface meridional wind velocity are enhanced around the particular SST front, especially in winter (Figs. 1.3b,e; Nakamura and Shimpo 2004), which may influence on low-level clouds nearby. In addition, since those baroclinic eddies transport westerly momentum toward its core region, they can reinforce the subtropical high with enhanced westerlies on its poleward edge. Thus seasonally enhanced storm-track activity in winter (Nakamura and Shimpo 2004) can also be an important factor for the wintertime enhancement of the Mascarene high.

In boreal summer (or austral winter), the Asian summer monsoon, one of the strongest seasonal variations in Earth's climate system, may also have significant impacts on the subtropical high (and thus low-level clouds) in the South Indian Ocean. While cross-equatorial surface winds starting from the subtropical South Indian Ocean carry a large amount of moisture toward the monsoon regions (Fig. 1.4), upper-tropospheric divergent winds from the Asian summer monsoon regions reach the subtropical South Indian Ocean across the equator, resulting in enhanced horizontal convergence and mid-tropospheric subsidence above the wintertime Mascarene high (Fig. 1.5). This is suggestive of certain remote influences from the Asian summer monsoon on the subtropical Mascarene high in the South Indian Ocean. Under the influence of the monsoon, the climatological surface easterlies, as the necessary background condition for the occurrence of the WES feedback, blow along the equator only in austral summer and early fall (e.g., Kawamura et al. 2001; Schott et al. 2009), although the westerlies on the northern side of the ITCZ located at 5°S-10°S (Fig. F1a) hamper equatorward propagation of the coupled signal from the subtropical South Indian Ocean in those seasons.

Considering those intriguing aspects, the South Indian Ocean is a suitable region for seeking new large-scale controls on LCF as well as for quantifying feedback from low-level clouds on the subtropical high without the interference of the equatorial asymmetric mode generated under the WES feedback. The purpose of this study is 1) to assess the coupling between the subtropical high and low-level clouds and its seasonality over the South Indian Ocean, and 2) to reveal the modulations of the coupled system by the storm-track activity maintained by the Agulhas SST front and remote influence by the Asian summer monsoon in austral winter. In Chapter 2, we investigate the seasonality of the impacts of the subtropical Mascarene high, the storm track, and the SST front on LCF over the South Indian Ocean in detail, and the distinct seasonality is then highlighted in comparison with the corresponding seasonality over the South Atlantic and Pacific. Our investigation takes advantage of the Moderate Resolution Imaging Spectroradiometer (MODIS) on the Aqua satellite, whose horizontal resolution is sufficient for capturing impacts of the oceanic front on low-level clouds. Not only subtropical but also midlatitude/subpolar oceanic regions are analyzed in Chapter 2. In Chapter 3, we examine three-dimensional structure and maintenance mechanisms for the summertime and wintertime subtropical highs as the planetary wave component, using state-of-the-art atmospheric reanalysis datasets as well as numerical experiments with an atmospheric dynamical model and a general circulation model. This chapter highlights the impacts of the storm-track activity maintained by the Agulhas SST front and the remote influence from the Asian summer monsoon as well as local feedback associated with the subtropical high and low-level clouds. In Chapter 4, we assess the radiative impacts of low-level clouds on the subtropical high using a coupled general circulation model combined with the atmospheric dynamical model used also in Chapter 3. We quantitatively discuss the impacts of cloud-top radiative cooling and the albedo effect on the subtropical high and their seasonal difference. General concluding remarks are given in Chapter 5, where the relationship among the subtropical Mascarene high, the storm-track activity, the Agulhas SST front and the Asian summer monsoon clarified by this study is summarized. The implications and prospects for the future works are also discussed. Note that a major portion of Chapter 2 has been published in Miyamoto et al. (2018).

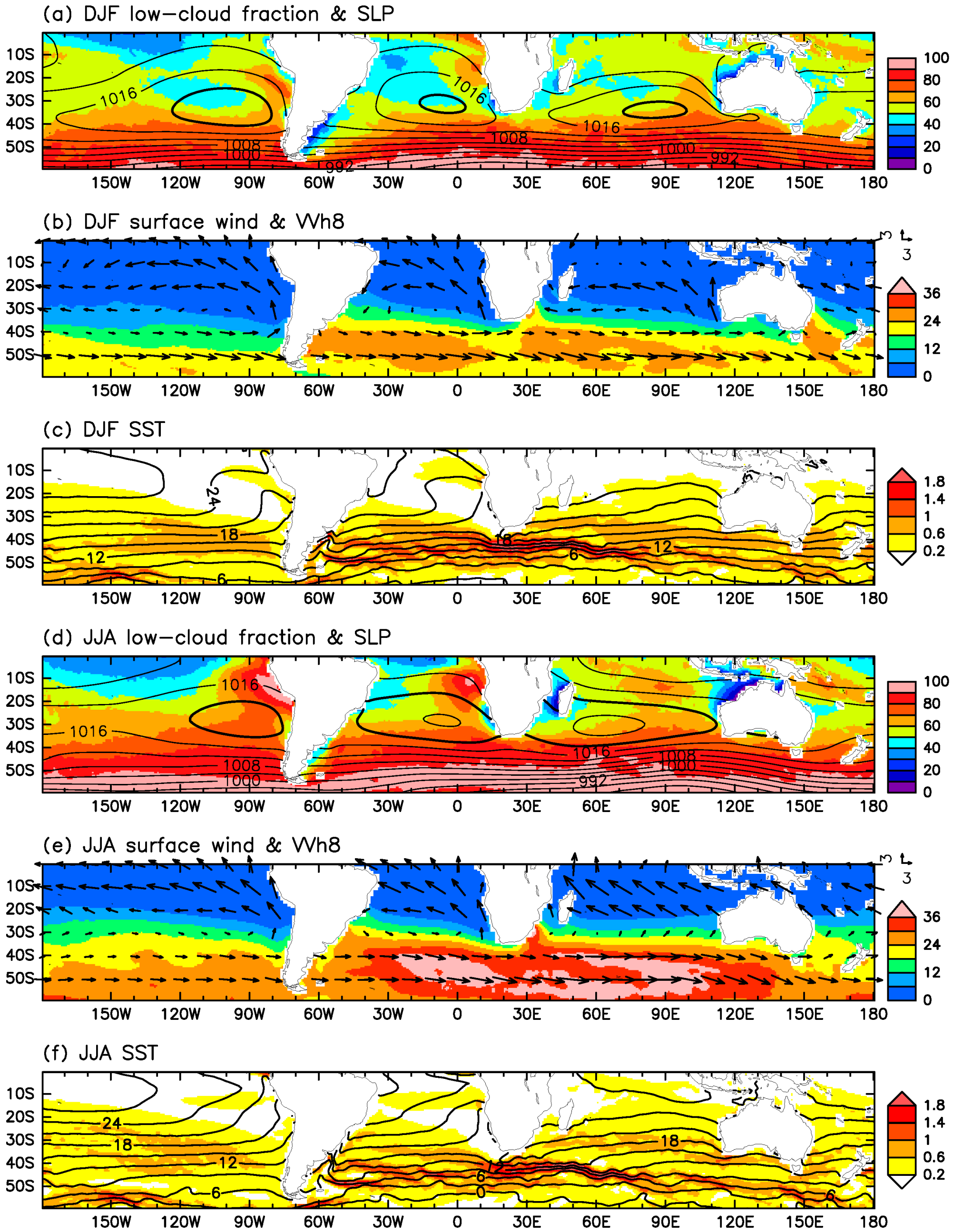

Figure 1.3: (a) Climatological-mean sea-level pressure (SLP) (contoured for every 4 hPa, with heavy lines for 1020 hPa) and low-cloud fraction (LCF) (color shaded for every 10 % as indicated on the right) over the southern oceans in austral summer (DJF). (b) Climatological-mean surface winds (m s^{-1}, arrows with reference on the right) and the variance of 8-day high-pass-filtered fluctuations of surface meridional wind (color shaded for every 6 m^2 s^{-2} as indicated on the right) for DJF. (c) Climatological-mean SST (contoured for every 3 °C) and its meridional gradient (color shaded for every 0.4 °C $(100\,\mathrm{km})^{-1}$) for DJF. (d-f) Same as in (a-c), respectively, but for austral winter (JJA). (e) Same as in (b), but for JJA. (f) Same as in (c), but for JJA. The climatologies are for the 2002/07-2015/06 period. LCF is based on MODIS and estimated under random overlap assumption, whereas the other variables are based on ERA-Interim.

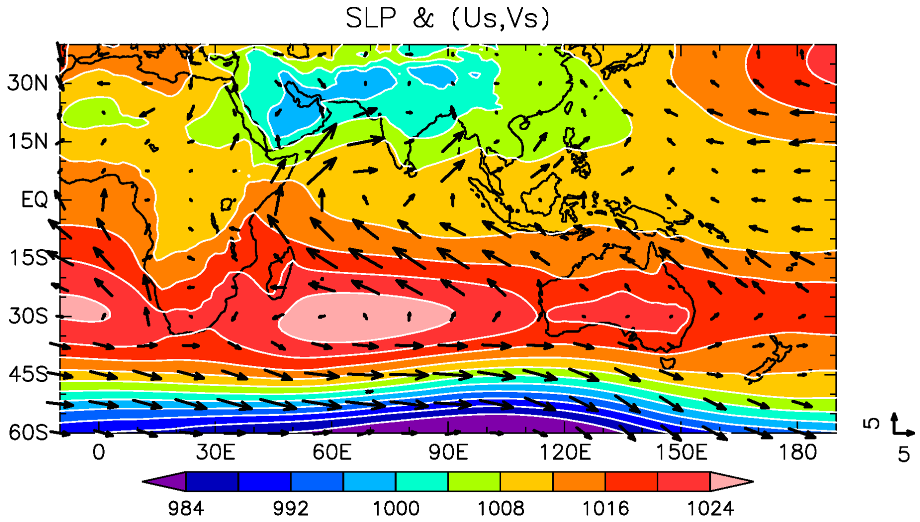

Figure 1.4: Climatological-mean August SLP (color shaded for every 4 hPa) and surface winds (m s^{-1}, arrows) based on JRA-55 for the 1979-2018 period.

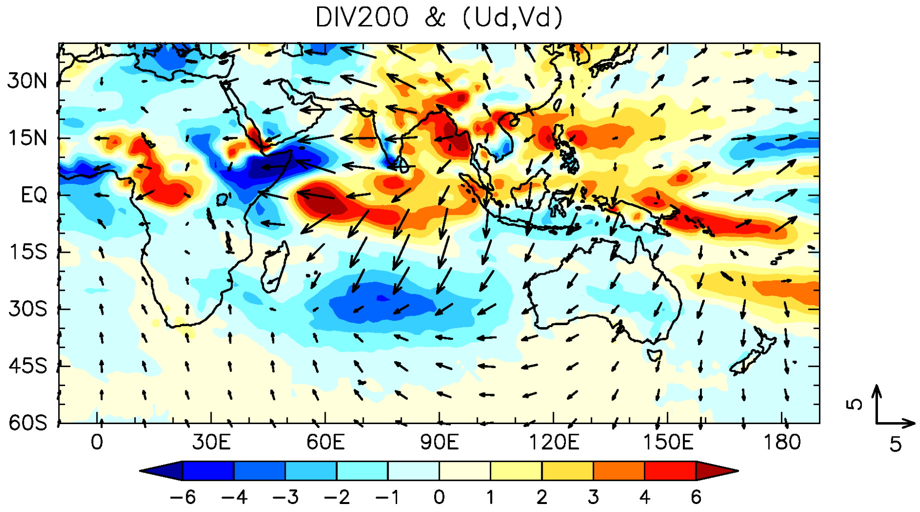

Figure 1.5: Climatological-mean August zonally asymmetric 200-hPa horizontal divergence (s^{-1}, color shadings) and divergent winds (m s^{-1}, arrows) based on JRA-55 for the 1979-2018 period. The color convention is indicated at the bottom.

Chapter 2

Influence of the subtropical high and storm track on low-cloud fraction and its seasonality over the South Indian Ocean

2.1 Introduction

Figures 2.1 and 2.2 indicate processes that will be demonstrated in this chapter in the feedback system associated with subtropical low-level clouds over the South Indian Ocean. Note that we present the complete schematic diagrams in Chapter 5 (Figs. 5.1 and 5.2). In this chapter, we substantiate influences of the subtropical high and storm track on low-level clouds over the South Indian Ocean. While maintenance of low-level clouds by the subtropical high through lower-tropospheric stability in summer, which we also confirm in this chapter, has already been demonstrated by previous studies (e.g., Klein and Hartmann 1993; Wood and Bretherton 2004; Wood 2012), we first reveal the influences of subtropical high and storm track on the basin-wide enhancement of LCF in winter. In addition, we analyze midlatitude/subpolar oceanic regions in this chapter.

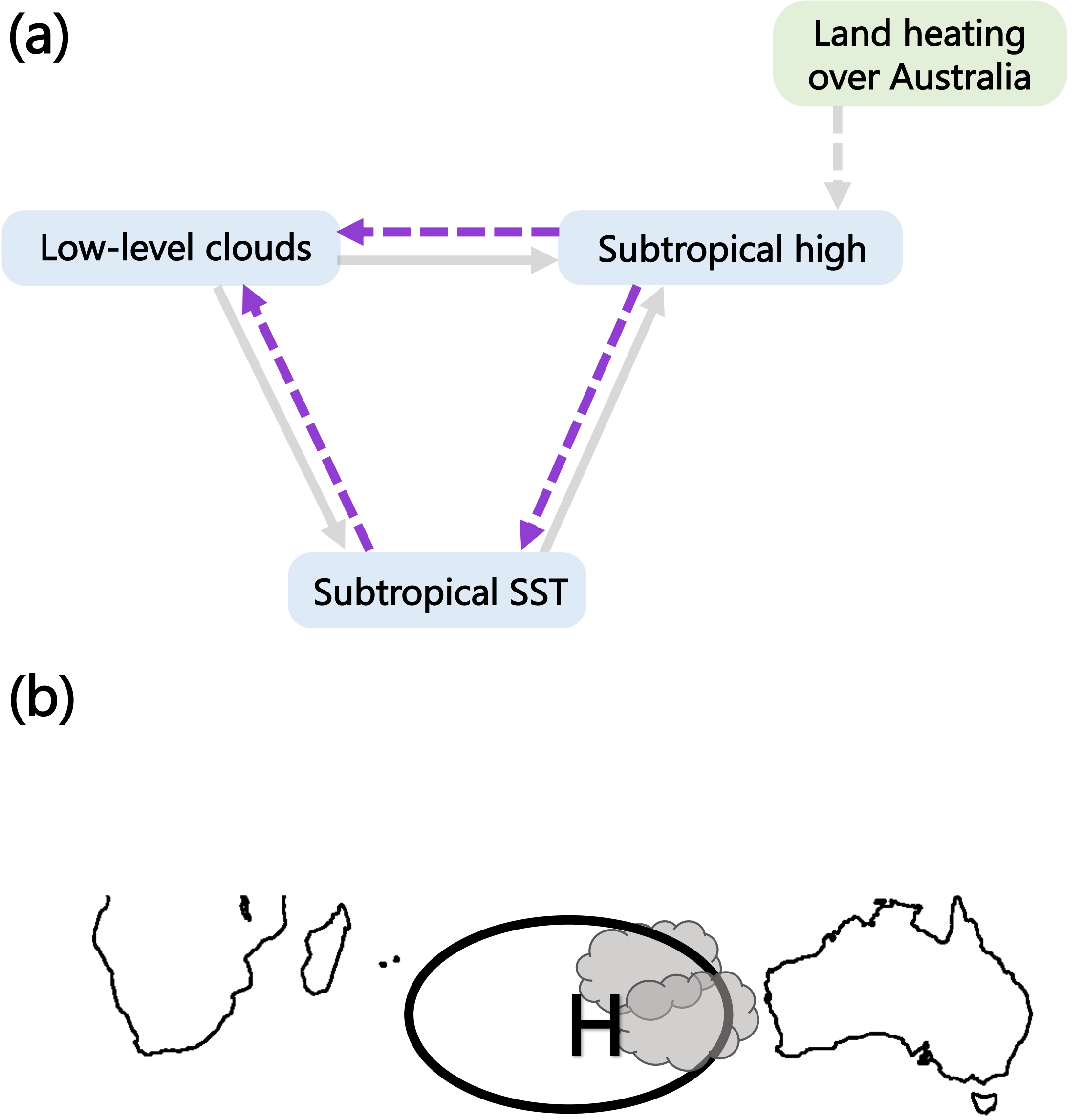

Figure 2.1: (a) Schematic diagram showing a feedback system associated with subtropical low-level clouds over the South Indian Ocean in austral summer. Solid line arrows indicate an influence demonstrated by the present study while dashed line arrows indicate that demonstrated by previous studies. Thin grey arrows indicate a feedback discussed in detail in other chapters. Light blue boxes signify the components of the feedback associated with low-level clouds while the light green box signifies the components that can modulate the feedback. (b) Geographical location of each factor in (a). “H” signifies the subtropical high whereas grey objects signify low-level clouds.

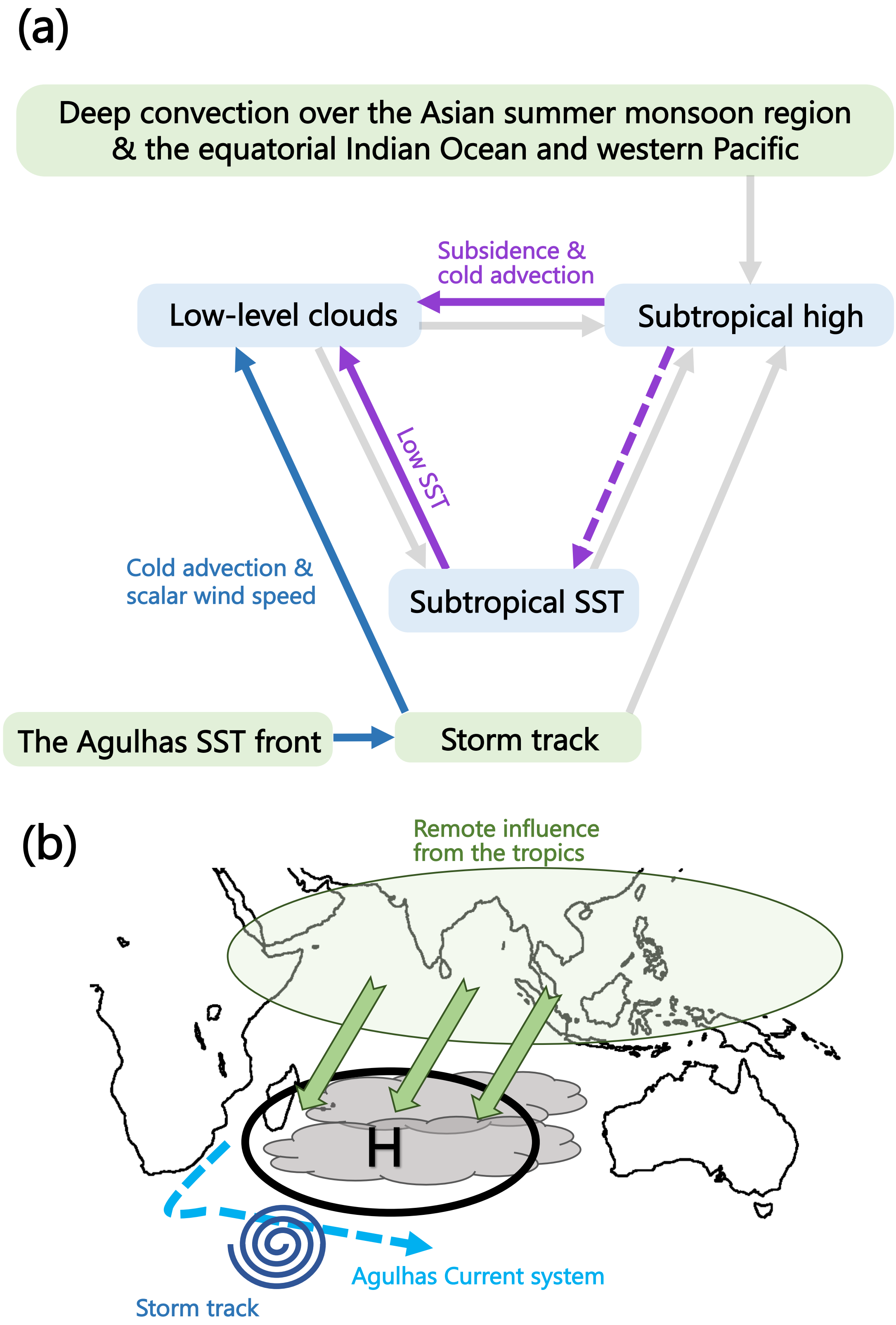

Figure 2.2: Same as in Fig. 2.1, but for austral winter. Green arrows in (b) indicate upper-tropospheric divergent wind from the tropics.

2.2 Data

a Satellite data

In this study, we use the collection 06 Level-3 daily cloud product of MODIS onboard Aqua on a $1^\circ \times 1^\circ$ grid (King et al. 2006; Hubanks et al. 2016). The horizontal resolution is adequate for extracting impacts of oceanic fronts, as found in the SST climatologies after interpolated onto the MODIS grid (Figs. 1.3c and 1.3f). Only daytime ($\sim$ 1030 LT) data are analyzed for a 13-year period from July 2002 to June 2015. We utilize cloud mask, which is not subjected to the additional screening for the retrieval of cloud optical properties (called “clear sky restoral”), and cloud top pressure as well. In this study, those clouds whose top pressures are higher than 680 hPa are regarded as “low-level clouds”. Since MODIS cannot detect low-level clouds if overlapped with mid- and/or high-level clouds, the random overlap assumption is used for reducing the influence of mid- and high-level clouds (e.g., Weare 2000). This is a reasonable assumption outside the areas of deep convection and landmass (McCoy et al. 2014; Li et al. 2015). In this study, seasonality in LCF over the subpolar ocean is not discussed in detail, because large solar zenith angles (greater than 65°-70°) are likely to introduce errors into the MODIS cloud retrievals (Grosvenor and Wood 2014).

Using optical depth τ and effective radius r_{eff}, we estimate liquid water path (LWP) and droplet number concentration (N_c) of low-level clouds everyday when mid- and/or high-level clouds are not present:

$$\mathrm{LWP} = \frac{5}{9}\rho_w \tau r_{\mathrm{eff}} \tag{2.1}$$

$$N_c = K\tau^{1/2} r_{\mathrm{eff}}^{-5/2} \tag{2.2}$$

where $K = (5\beta C_w/8\pi^2 k^2 \rho_w)^{1/2}$ and ρ_w is the density of water (Brenguier et al. 2000; Szczodrak et al. 2001; Bennartz 2007). C_w is the moist adiabatic condensate coefficient and is calculated using cloud top temperature and pressure. β represents the proximity of clouds to adiabatic clouds and is set to 0.8 (Bennartz 2007), whereas k reflects the shape of the cloud droplet size distribution and is set to 0.8 for maritime air masses.

For planetary albedo, we use Level-3 daily CERES-SSF product on a $1° \times 1°$ (Wielicki et al. 1996). Daytime observations from Aqua are used to calculate statistics for the same period as MODIS data only for days when mid- and/or high-level clouds are not present.

b Meteorological parameters

For meteorological parameters, we use the ERA-Interim global atmospheric reanalysis data (Dee et al. 2011). The $0.75° \times 0.75°$ gridded data have been interpolated linearly onto the $1° \times 1°$ MODIS grid. We use the data only at 0900 UTC (as average between 0600 UTC and 1200 UTC) for the South Indian Ocean, at 1500 UTC (as average between 1200 UTC and 1800 UTC) for the South Atlantic and at 2100 UTC (as average between 1800 UTC and 2400 UTC) for the South Pacific to the east of the International Date Line, so as to correspond roughly to the overpass time of the Aqua for each of the basins. Since the horizontal resolution of SST data prescribed at the lower boundary of the atmospheric forecast model for data assimilation for the ERA-Interim has been significantly improved since January 2002 (Masunaga et al. 2015), we utilize the data from July 2002 through June 2015 of surface sensible heat flux (SHF), surface latent heat flux (LHF), 700-hPa ω, 700-hPa relative humidity (RH), 2-m surface air temperature (SAT), 10-m surface winds, sea-level pressure (SLP) and SST. It has been shown that air-sea fluxes products somewhat differ from one dataset to another (e.g., Smith et al. 2011; Liu et al. 2011; Yu et al. 2011), which suggests that SHF and LHF in ERA-Interim also include some uncertainties. We have confirmed that qualitatively the same results are obtained when surface fluxes in J-OFURO3 (Tomita et al. 2018) for the period of 2002-2013 are used in place of the ERA-Interim data (Figs. C.1-C.4). In addition, we use the SST data prescribed for ERA-Interim. Near-surface temperature advection and wind convergence have been evaluated on a daily basis at the lowest level of the forecast model used for the ERA reanalysis, as in Masunaga et al. (2015).

In this study, the estimated inversion strength (EIS) defined by Wood and Bretherton (2006) is used as a measure of the strength of the inversion layer at the top of the boundary layer:

$$\mathrm{EIS} = (\theta_{700} - \theta_{\mathrm{sfc}}) - \Gamma_m^{850}(z_{700} - z_{\mathrm{LCL}}), \tag{2.3}$$

where θ_{700} and θ_{sfc} denote potential temperature at 700 hPa and the surface, respectively, whereas z_{700} and z_{LCL} denote local altitudes of the 700-hPa surface and lifting condensation level, respectively. In Eq. (2.3), Γ_m^{850} signifies moist adiabatic lapse rate at the 850-hPa level. We also use the estimated cloud-top entrainment index (ECTEI; Kawai et al. 2017), which is a modified version of EIS by taking a cloud-top entrainment criterion into account:

$$\mathrm{ECTEI} = \mathrm{EIS} - \beta(L/c_p)(q_{\mathrm{sfc}} - q_{700}) \tag{2.4}$$

where L is latent heat for evaporation, c_p is the specific heat of air at constant pressure, and β is 0.23. q_{700} and q_{sfc} are 700-hPa and 2-m specific humidity, respectively. EIS and ECTEI are calculated from the ERA-Interim data.

c AGCM output

This chapter utilizes output of ensemble model experiments with an atmospheric general circulation model (AGCM) for the Earth Simulator (AFES; Ohfuchi et al. 2004, 2007; Enomoto et al. 2008; Kuwano-Yoshida et al. 2010). The horizontal resolution is T119 (equivalently 1° grid intervals), with 56 levels in the vertical from the surface to approximately 0.1 hPa. Daily global SST fields taken from the Optimally Interpolated Advanced Very High Resolution Radiometer (AVHRR) Pathfinder SST (OISST) data produced by the U.S. National Oceanic and Atmospheric Administration (NOAA) with 0.25° resolution (Reynolds et al. 2007) are prescribed at the bottom boundary of AFES. This study analyzes the following two experiments: control experiment (AFES_CTL) with the original OISST data, and sensitivity experiment (AFES_SMTH) with the spatially smoothed OISST. The smoothed SST fields are created by applying a Gaussian-type smoothing filter as follows. In each grid point (x, y), SST is horizontally averaged with

Gaussian weighting $W_{k,l}$:

$$W_{k,l} = \exp\left[-\frac{(x-x_{k,l})^2}{a^2} - \frac{(y-y_{k,l})^2}{a^2}\right] \quad \text{where} \quad |x-x_{k,l}| \leq 2a \text{ and } |y-y_{k,l}| \leq 2a$$

else

$$W_{k,l} = 0$$

where k and l are longitudinal and latitudinal grid indices, respectively, of the SST field for the averaging, and a is set to 600 km. This procedure is performed in the extratropical latitudinal bands (30.125°-55.125° in each hemisphere) with ±5° latitudinal buffer zones. The summertime and wintertime climatological-mean distributions of SST prescribed for AFES_CTL and AFES_SMTH are shown in Figs. 2.3 and 2.4, respectively. The smoothing weakens the prominent meridional gradient of SST across the Agulhas Return Current around 40°S-45°S in either season. In both experiments, AFES is integrated for 32 years from January 1 of 1982 through December 31 of 2013. Each of the experiments has 15 ensemble members, all of which are used to calculate ensemble-mean fields. Since LCF for the AFES simulations is obtained as output through the International Satellite Cloud Climatology Project (ISCCP) simulator (Klein and Jacob 1999; Webb et al. 2001), we apply the random overlap assumption as for the MODIS data. In addition, we use SHF, 700-hPa and 2-m temperature, and surface pressure for the AFES simulations.

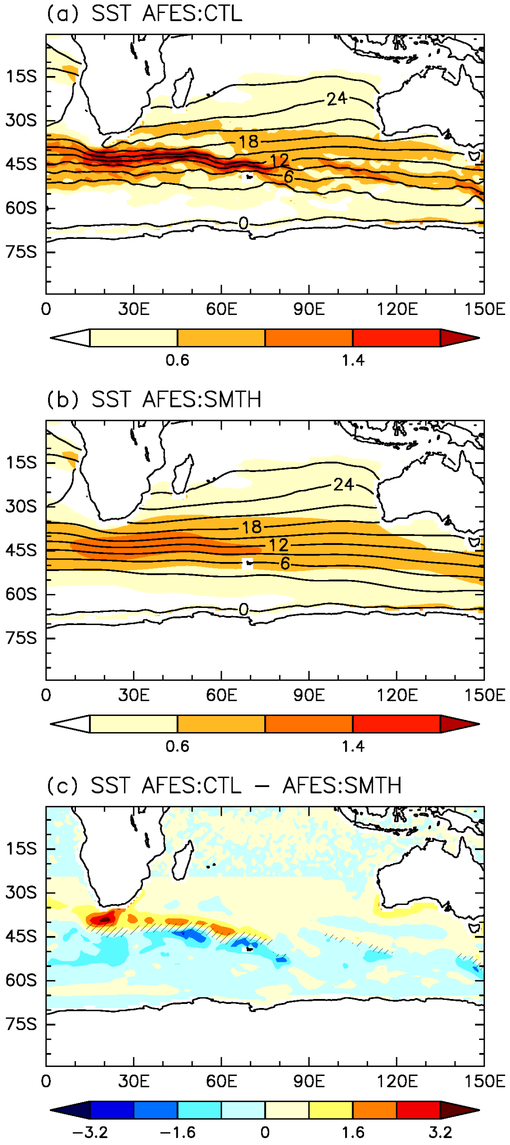

(a) SST AFES:CTL

(b) SST AFES:SMTH

(c) SST AFES:CTL − AFES:SMTH

Figure 2.3: DJF climatological distributions of SST (contoured for every 3°C) and its meridional gradient [color shaded for every 0.4°C $(100\ \mathrm{km})^{-1}$] prescribed for (a) AFES_CTL and (b) AFES_SMTH. (c) The difference of SST (color shaded, every 0.8°C) defined as AFES_CTL minus AFES_SMTH. Hatch in (c) indicates the area where the difference in meridional gradient of SST exceeds 0.4°C $(100\ \mathrm{km})^{-1}$.

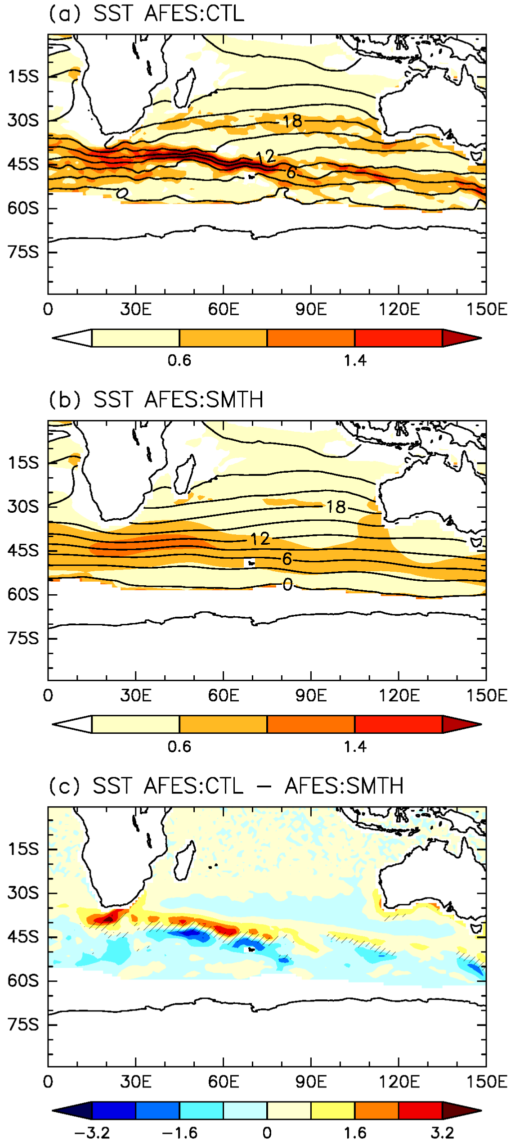

Figure 2.4: Same as in Fig. 2.3, but for JJA.

2.3 Influence of the Mascarene high and the storm track on LCF and its seasonality over the South Indian Ocean

a Overview of climatological distribution of LCF

Before making detailed discussions on the relationship between LCF and meteorological conditions, we give an overview of climatological-mean distributions of LCF over the South Indian Ocean for summer (Fig. 2.5a) and winter (Fig. 2.5b). Across the subtropical basin (equatorward of ∼35°S), zonal inhomogeneity is evident in summertime LCF, with a distinct local maximum off the west coast of Australia around 105°E and rapid decline toward the west (Fig. 2.5a). By contrast, wintertime LCF is more zonally uniform across the subtropical basin (Fig. 2.5b). Both in summer and winter, LCF over the midlatitude and subpolar oceans is higher than over the subtropical ocean, and its distribution exhibits a high degree of zonal uniformity. Figures 2.5a and 2.5b indicate higher LCF in winter than in summer, although the wintertime MODIS retrievals are likely to suffer from errors under large solar zenith angles (Grosvenor and Wood 2014). In fact, cloud-top height-optical depth histograms based on the Multiangle Imaging Spectroradiometer (MISR) measurements (Marchand et al. 2010) show that climatological-mean LCF estimated under the random overlap assumption decreases into winter (not shown), which appears to be consistent with the zonal-mean LCF over the Southern Ocean (McCoy et al. 2014). In the following, we therefore avoid detailed investigation of the wintertime low-level clouds over the subpolar ocean.

Previous studies have indicated that climatological-mean distribution of LCF and its seasonality are well explained by lower-tropospheric stability, whose enhancement acts to increase LCF (e.g., Klein and Hartmann 1993; Wood and Bretherton 2006; Koshiro and Shiotani 2014). Climatological-mean distributions of EIS defined in Eq. (2.3) are thus shown in Figs. 2.5c and 2.5d for DJF and JJA, respectively. Across the summertime subtropical basin (Fig. 2.5c), EIS maximizes off the west coast of Australia around 105°E, in good correspondence with the spatial pattern of LCF (Fig. 2.5a). This local maximum of EIS corresponds to the longitudinal minimum in SST around 105°E (Fig. 2.5a). In fact, SST just off the Australian coast is slightly higher due to the southward Leeuwin Current, which is a unique feature of the South Indian Ocean from other ocean basins at equivalent latitudes (Smith et al. 1991; Kataoka et al. 2014). Compared to SST, 700-hPa potential temperature (θ_{700}) is more zonally uniform (Fig. 2.5c), but with a slight zonal asymmetry. θ_{700} at 30°S minimizes around 85°E and increases gradually toward the east. At 29.5°S, for example, the SST difference from 105.5°E to 85.5°E is -1.6 K, whereas the corresponding θ_{700} difference is 1.7 K. Thus, the increase in θ_{700} toward the east from 85°E also contributes to the local maximum of EIS off the west coast of Australia. This eastward warming is contributed to, in part, by the enhanced subsidence around [30°S, 110°E] (Fig. 2.5e). The enhanced subsidence and associated surface divergence are required to keep the vorticity balance with strong equatorward winds in the eastern portion of the surface subtropical high (Fig. 2.7c; Rodwell and Hoskins 2001; Miyasaka and Nakamura 2010). Compared to the summertime situation, EIS in winter exhibits more zonally uniform distribution across the subtropical basin (Fig. 2.5d) in accordance with the spatial pattern of LCF (Fig. 2.5b). The high degree of zonal uniformity in wintertime

EIS reflects zonally uniform distribution of SST (Fig. 2.5b), 700-hPa θ (Fig. 2.5d) and free-tropospheric subsidence (Fig. 2.5f). Poleward of 30°S, EIS in summer increases rapidly with latitude and maximizes around 50°S (Fig. 2.5c). The poleward increase in EIS is consistent with the latitudinal distribution of LCF (Fig. 2.5a). Overall, the spatial patterns of LCF over the South Indian Ocean in both summer and winter are in reasonable correspondence with those of EIS, as previous studies have indicated.

We point out, however, that there are several aspects that cannot be explained fully by EIS. For example, EIS increases rapidly across the midlatitude SST front along the Agulhas Return Current and maximizes on the poleward flank of the front (Fig. 2.5c), but the corresponding increase in LCF across the Agulhas SST front is more gradual (Fig. 2.5a). In fact, over the subpolar ocean poleward of 50°S, EIS slightly decreases with latitude, while LCF still increases with latitude. Though not our primary focus, this discrepancy is discussed briefly in Section 2.4c. Other discrepancies in detailed aspects in the seasonal cycles are discussed in Section 2.3c.

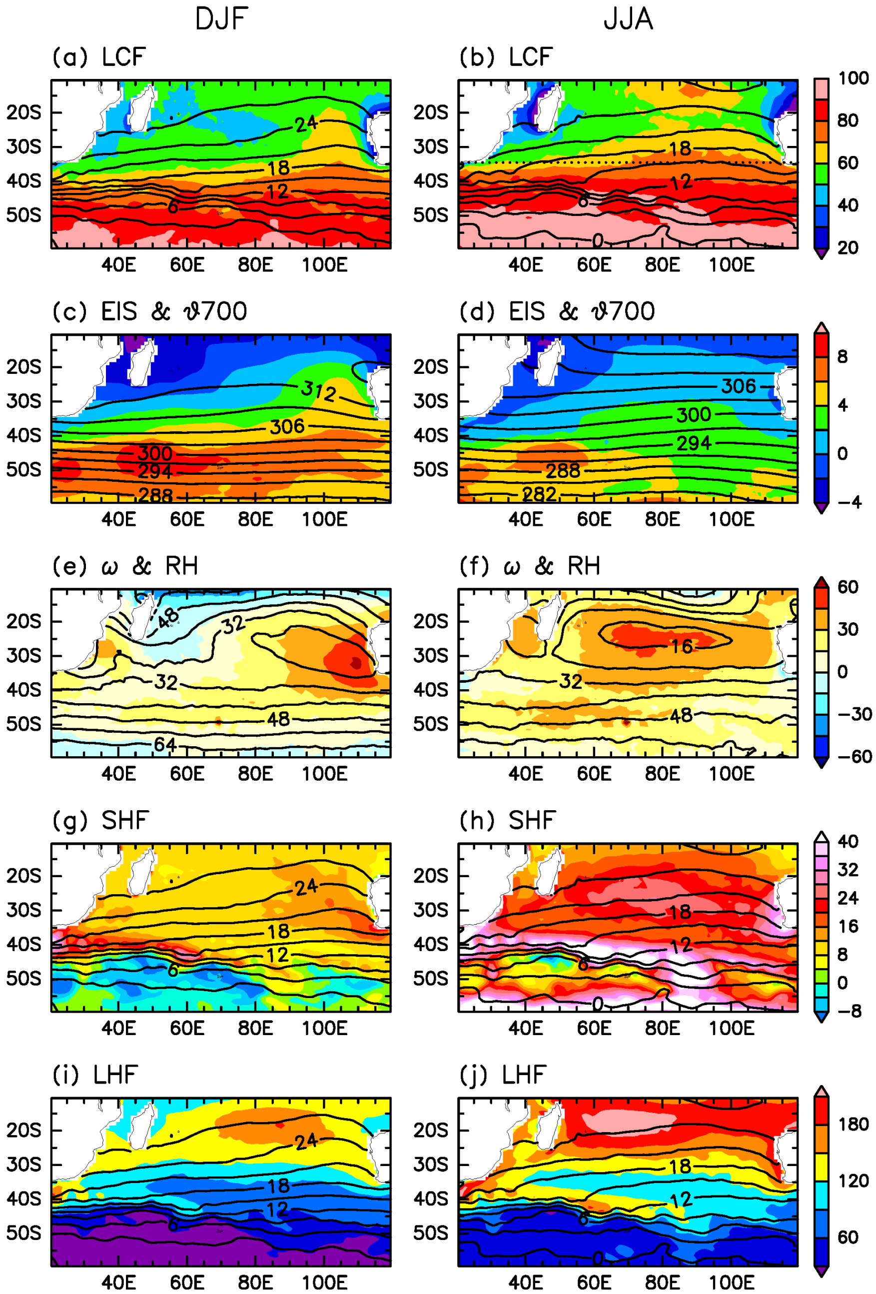

Figure 2.5: Climatological distributions for austral summer (DJF) of maritime (a) LCF (color shaded for every 10 %) and SST (contoured for every 3 °C), (c) EIS (color shaded for every 2 K) and 700-hPa θ (contoured for every 3 K), (e) 700-hPa ω (color shaded for every 15 hPa day^{-1}) and 700-hPa RH (contoured for every 8 %), (g) SHF (color shaded for every 4 W m^{-2}; positive values for upward flux) and SST (contoured for every 3 °C), (i) LHF (color shaded for every 30 W m^{-2}; positive values for upward flux) and SST (contoured for every 3 °C). (b), (d), (f), (h) and (j) Same as in (a), (c), (e), (g) and (i), respectively, but for austral winter (JJA). In (b), the dotted line indicates the latitude poleward of which more than 30% of observations were made under (daily maximum) solar zenith angles greater than 65°.

b LCF around the Agulhas SST front

Figure 2.6 shows meridionally high-pass-filtered fields of LCF, oceanic and meteorological parameters around the Agulhas SST front for DJF. The meridional high-pass filtering has been applied, in order to highlight the impacts of the meridionally pronounced SST gradient across the front. Here local departures of a given variable from the meridional nine-point running-mean values are regarded as its meridionally high-pass-filtered component. This procedure is equivalent to 9° latitudinal high-pass-filtering. Comparison between Figs. 2.6a and 2.6b reveals opposing tendencies between LCF and EIS across the front. Specifically, LCF shows local maxima (minima) on the equatorward (poleward) flank of the SST front (Fig. 2.6a), albeit EIS exhibits local minima (maxima) on the equatorward (poleward) flank of the front (Fig. 2.6b) in accordance with the underlying SST distribution. Figure 2.6d shows the distribution of (upward) SHF, whose enhancement acts to increase LCF (e.g., Xu et al. 2005; Mauger and Norris 2010). There is indeed local enhancement (reduction) of SHF on the equatorward (poleward) flank of the SST front, which overall coincides with the local maxima (minima) of LCF. On the warmer side of the SST front, the enhanced heat release (SHF) from the warm Agulhas Return Current acts to lower SLP locally (not shown) and thereby induce wind convergence near the surface (Fig. 2.6f) and vice versa on the cooler side of the SST front with locally enhanced near-surface divergence. These cross-frontal contrasts are considered to be through the hydrostatic effect (Lindzen and Nigam 1987; Shimada and Minobe 2011). The corresponding weakening of lower-tropospheric subsidence on the warmer side of the SST front (Fig. 2.6c) may be in part a signature of this hydrostatic effect, while no systematic signals are found in free-tropospheric relative humidity around the SST front (Fig. 2.6e).

A close inspection of Fig. 2.6f reveals, however, that the local maxima and minima of wind convergence near the surface tend to be shifted slightly eastward of the corresponding pattern of SST. This slight eastward shift is attributable to the advective effect by the prevailing time-mean near-surface westerlies and/or to enhanced (suppressed) turbulent mixing over warmer (cooler) SST and the resultant downward transfer of the momentum of the prevailing westerlies within the boundary layer (Wallace et al. 1989; Chelton et al. 2004; O'Neill et al. 2010). The latter process leads to surface divergence and convergence downstream of the cool and warm SSTs, respectively. The prevailing near-surface westerlies are characteristic of the westerly jetstream driven by enhanced activity of synoptic-scale atmospheric eddies migrating along the storm track (e.g., Nakamura et al. 2008), through their poleward heat transport and resultant downward transfer of wind momentum of the upper-tropospheric westerly jet. The enhanced storm-track activity is maintained in the presence of the Agulhas SST front (Nakamura and Shimpo 2004; Nakamura et al. 2008). In association with the local minima and maxima of near-surface wind convergence (Fig. 2.6f), free-tropospheric subsidence tends to be weaker (stronger) over warmer (cooler) SST (Fig. 2.6c), but their spatial patterns do not coincide perfectly. This inconsistency may be due to synoptic-scale atmospheric eddies that dynamically induce subsidence climatologically on the warmer side of the SST front. Both observational studies (e.g., Norris and Leovy 1994; Clement et al. 2009; Qu et al. 2014, 2015; Seethala et al. 2015; Myers and Norris 2016; McCoy et al. 2017) and modelling studies (e.g., Rieck et al. 2012; Brient and Bony 2013; Bretherton and Blossey 2014) suggested that LCF decreases with increasing SST. We then argue that direct impacts of EIS and SST should act to decrease LCF on the warmer side of the SST front, and that the local maximum of LCF must therefore be due to the locally enhanced SHF. Additionally, the locally enhanced wind convergence near the surface induced by enhanced SHF can also make additional contributions to the local increase in LCF.

Figure 2.7a shows climatological-mean near-surface temperature advection. There is cold advection on the *warmer* side of the Agulhas SST front, resulting in local enhancement of SHF (Fig. 2.5g). Figure 2.7c shows near-surface temperature advection based on climatological-mean winds and temperature, which is generally weak on the *warmer* side of the Agulhas SST front. The sole noticeable exception is found around [45°S, 60°E], where the mean westerlies can yield modest cold advection due to a slight meridional tilt of the frontal axis. We therefore argue that the primary contributor to the enhanced SHF on the equatorward flank of the SST front must be cold advection by atmospheric transient eddies (Fig. 2.7e) that recurrently develop along the storm track near the SST front (Fig. 1.3b). We have confirmed that contribution from interannual variations of wind and temperature is weak (not shown). Although eddy-associated fluctuating winds across the SST front act to relax the pronounced cross-frontal SAT gradient, resultant instantaneous enhancement of SHF on the warmer side of the SST front acts to restore the cross-frontal SAT gradient efficiently (Nonaka et al. 2009; Taguchi et al. 2009), and their accumulated effects lead to the climatological enhancement in SST$-$SAT on the equatorward flank of the front (Nakamura et al. 2008; Hotta and Nakamura 2011). Sub-monthly oceanic meso-scale eddies around the Agulhas Return Current and Antarctic Circumpolar Current may also contribute to the climatological-mean SHF (Frenger et al. 2013). Quantification of their impact is, however, difficult due to the data used in our study, as the horizontal resolution is inadequate for resolving those eddies.

Enhancement of scalar wind speed by fluctuating winds further augments SHF, whose processes are investigated in detail based on the daily ERA-Interim data, and the results are summarized in Fig. 2.8. Since SST−SAT increases almost linearly with the enhanced surface southerlies (Fig. 2.8b) and scalar wind speed is enhanced in case of strong southerlies and northerlies (Fig. 2.8c), SHF is strongly enhanced under the strong southerlies while the SHF decline under the enhanced northerlies is rather modest (Fig. 2.8a). Likewise, since scalar wind speed also increases under both enhanced easterlies and westerlies (Fig. 2.8f), while SST−SAT is insensitive to zonal wind velocity (Fig. 2.8e), SHF increases under both enhanced westerlies and easterlies (Fig. 2.8d).

To evaluate the impacts of nonlinearity embedded in scalar wind speed on SHF more quantitatively, SHF is reconstructed as $\mathrm{SHF_r}$ by using a simple bulk formula:

$$\mathrm{SHF_r} = CW(\mathrm{SST} - \mathrm{SAT}) \tag{2.5}$$

and

$$C = \rho c_p c_h \tag{2.6}$$

with ρ and c_p denote air density and specific heat at constant pressure of air, and heat transfer coefficient c_h is set to 0.0015 (Holton and Hakim 2012). We decompose scalar wind speed at the surface, denoted as W in Eq. (2.5), for a given month into the wind speed $\hat{W}$ calculated from monthly-mean zonal and meridional wind velocities, and the residual W^* that represents the contributions from sub-monthly wind fluctuations:

$$W = \hat{W} + W^* \tag{2.7}$$

Note that W^* includes not only the contributions from sub-weekly fluctuations associated migratory transient eddies but also the contributions from more persistent fluctuations associated with quasi-stationary atmospheric eddies. If this decomposition is incorporated into Eq. (2.5), the seasonal-mean climatology of the reconstructed SHF ($\overline{\mathrm{SHF_r}}$) can be decomposed into

$$\overline{\mathrm{SHF_r}} = C\hat{W}(\overline{\mathrm{SST}-\mathrm{SAT}}) + C\overline{W^*}(\overline{\mathrm{SST}-\mathrm{SAT}}) + C\overline{(W^*)'(\mathrm{SST}-\mathrm{SAT})'} \tag{2.8}$$

where overbars denote the climatological-means and primes denote deviations from the climatological-mean (i.e., anomalies). Note that $\overline{W^*}$ is not necessarily zero because of the nonlinearity of scalar wind speed. The climatological-mean $\mathrm{SHF_r}$ for summer (Fig. 2.9a) and winter (Fig. 2.9b) reproduces the spatial patterns of SHF (as a product of ERA-Interim) for the respective seasons (Figs. 2.5g-h), including its distinct gradient across the Agulhas SST front, although $\mathrm{SHF_r}$ generally has slight negative biases across the basin for both seasons. Overall, the spatial pattern of $\mathrm{SHF_r}$ over the basin is accounted for largely by the contribution from the climatological-mean surface wind velocities for each of the seasons (Figs. 2.9c-d). To the sharp decline of $\mathrm{SHF_r}$ poleward across the Agulhas SST front, by contrast, sub-monthly fluctuations in surface winds make a positive contribution (Figs. 2.9e-f), which is comparable to that from the climatological-mean wind velocities (Figs. 2.9c-d). The positive contribution from the sub-monthly fluctuations is obvious, especially toward the enhanced upward SHF on the equatorward flank of the Agulhas SST front. In winter (Fig. 2.9f), enhancement of upward SHF is also recognized on the equatorward flank of the zonally-extending subtropical SST front around 25°S-35°S. Finally, the contribution from the transient eddy covariance term $C\overline{(W^*)'(\mathrm{SST}-\mathrm{SAT})'}$ is found negligible for each of the seasons (Figs. 2.9g-h).

A comparison among Figs. 2.5-2.9 reveals that, on the equatorward flank of the Agulhas SST front, transient atmospheric eddies that recurrently develop along the storm track act to increase the occurrence of those events where SST−SAT and/or wind speed are augmented, resulting in particularly large SHF and thereby acting to facilitate the formation of shallow convective clouds. The resultant increase in LCF acts to reduce the gradient of LCF across the SST front than what is anticipated from the corresponding gradients of EIS (Fig. 2.5c) or SST (Fig. 2.5a). Similarly, enhanced wind speed by sub-monthly atmospheric eddies also augment LHF (not shown), resulting in local maximum of LHF on the equatorward flank of the Agulhas SST front (Figs. 2.5i-j). Enhancement of climatological-mean surface heat flux by high-frequency wind fluctuations through scalar wind speed has been recently investigated globally by Ogawa and Spengler (2019).

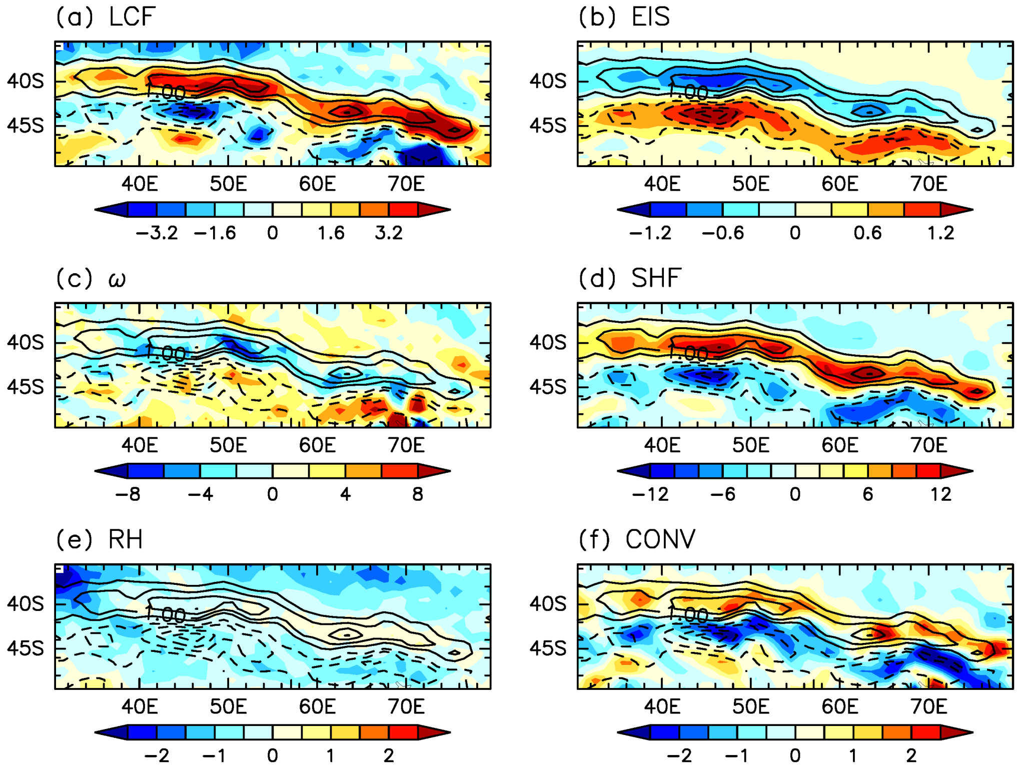

Figure 2.6: Meridionally high-pass-filtered fields around the Agulhas SST front for austral summer (DJF) of (a) LCF (color shaded for every 0.8 %), (b) EIS (color shaded for every 0.3 K), (c) 700-hPa ω (color shaded for every 2 hPa day^{-1}), (d) SHF (color shaded for every 2 W m^{-2}), (e) 700-hPa RH (color shaded for every 0.5 %), and (f) wind convergence near the surface (color shaded for every 0.5×10^{-6} s^{-1}). Superimposed with the contours is meridionally high-pass-filtered climatological SST (every 0.5 °C; solid and dashed lines for positive and negative values, respectively; zero contours are omitted) for DJF. Local departures of each variable from its meridional nine-point running-mean values are regarded as the meridionally high-pass-filtered component.

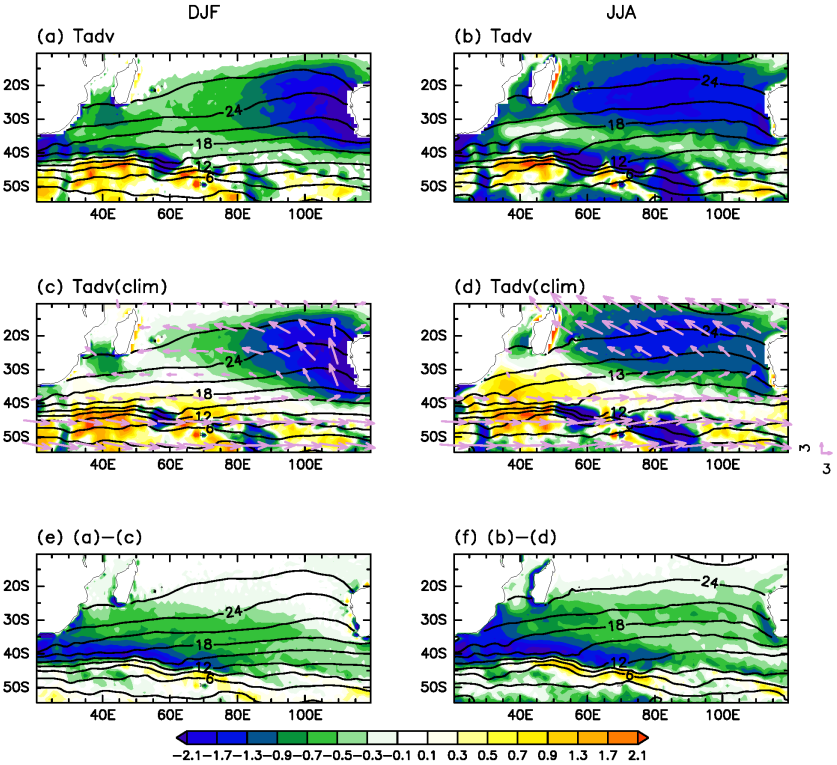

Figure 2.7: Same as in Fig.2.5a, but for (a) near-surface temperature advection (K day^{-1}, color shadings), (c) near-surface temperature advection calculated only from climatological-mean wind and temperature (K day^{-1}, color shadings) and surface winds (m s^{-1}, arrows), and (e) near-surface temperature advection by fluctuating wind and temperature calculated as (a)−(c) (K/day, color shadings). (b), (d) and (f) Same as (a), (c) and (e), respectively, but for austral winter (JJA). On all the panels, SST is superimposed with the contours (every 3 °C).

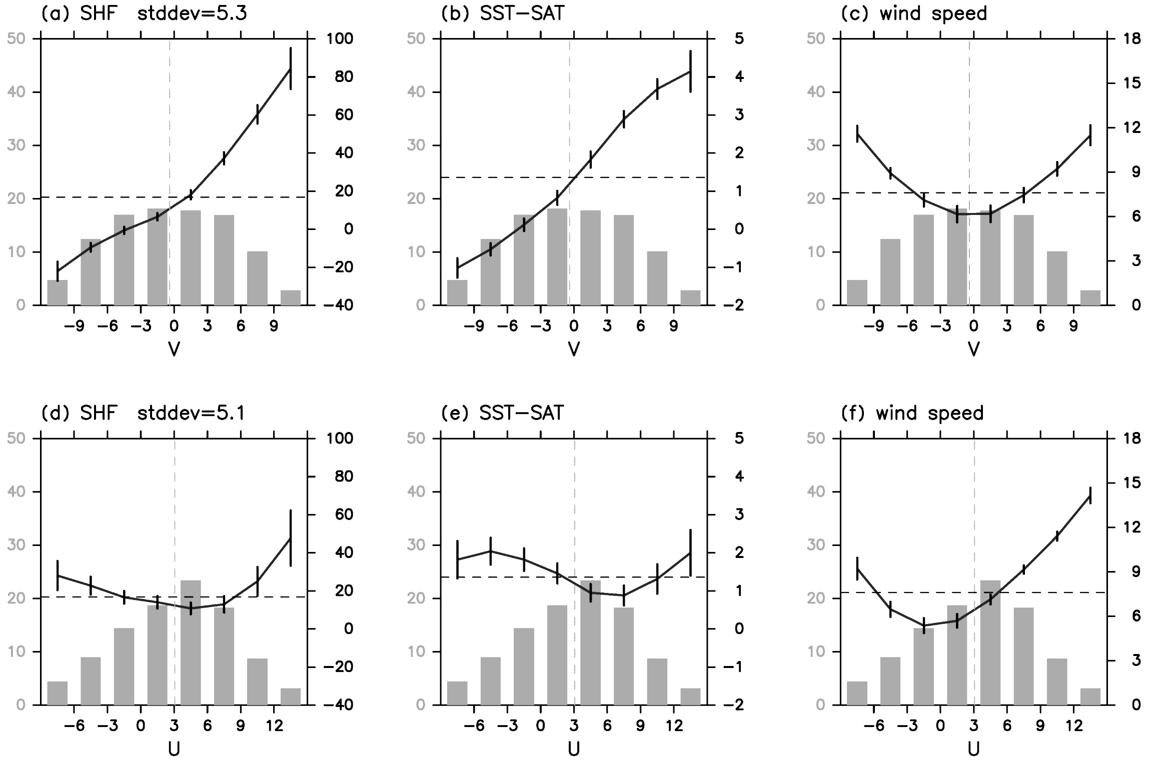

Figure 2.8: Dependence of daily (a) SHF (W m^{-2}; right ordinate), (b) SST−SAT (K; right ordinate) and (c) surface scalar wind speed (m s^{-1}; right ordinate) on surface meridional wind velocity in DJF. Grey bars are daily frequency (%; left ordinate) of surface meridional wind (m s^{-1}) at individual grid points within the domain on the equatorward flank of the Agulhas SST front [40.5°E-54.5°E, 37.5°S-41.5°S, AF]. Tick marks along the abscissa indicate bin boundaries. Leftmost and rightmost bars include all the samples of the strongest northerlies and southerlies, respectively. Black solid lines indicate climatological-mean values of the individual variables (right ordinate) for the individual bins with the 90% confidence intervals, while the climatological-mean values averaged over all the samples are represented by the black dashed horizontal lines. See Appendix A for the details of the confidence level. The grey dashed vertical lines indicate climatological-mean meridional wind. Standard deviation of surface meridional wind is added on the top of (a). (d-f) Same as in (a-c), respectively, but for the dependence of the variables on surface zonal wind velocity.

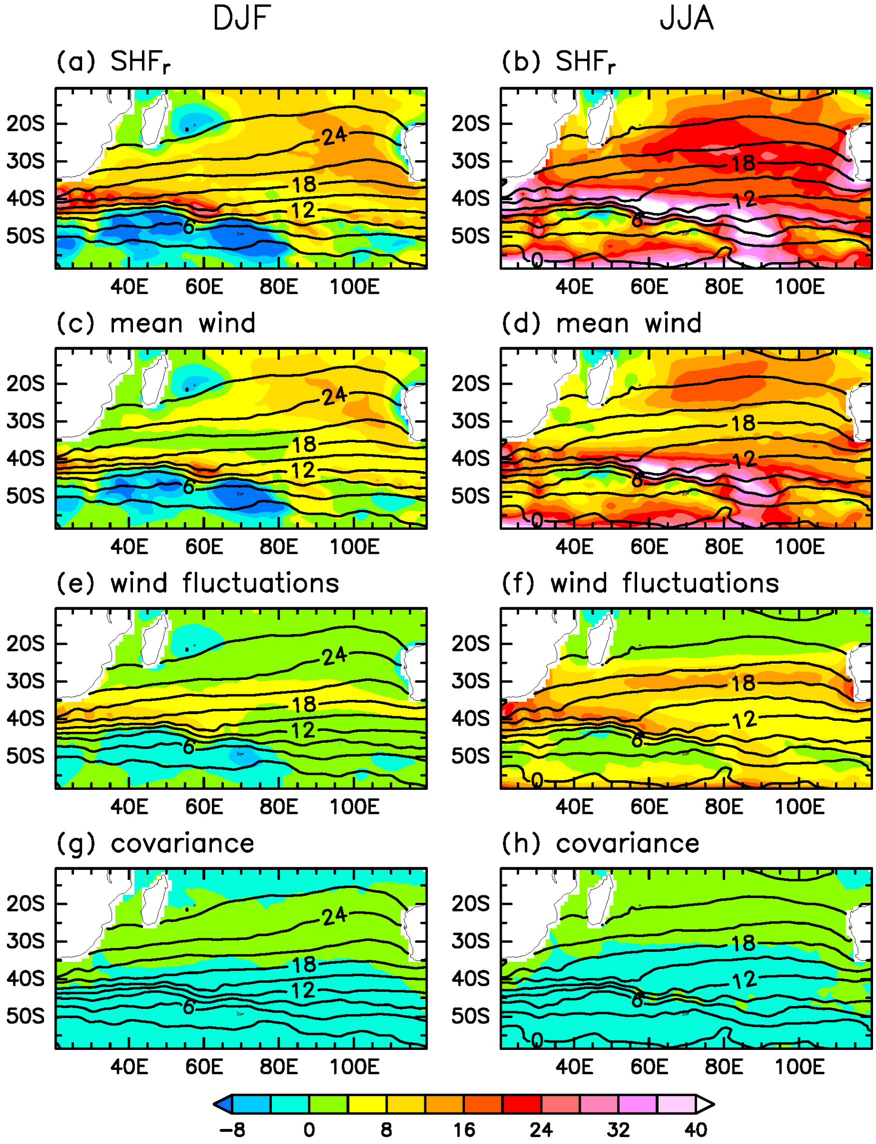

Figure 2.9: (a) (b) Same as in Fig. 2.5i, but for the reconstructed climatological-mean SHF ($\overline{\mathrm{SHF_r}}$; color shaded for every 4 W m^{-2} as indicated at the bottom of this figure) through the decomposition (2.8) in the text for austral summer (DJF) and winter (JJA). (c) (d) Same as in (a) and (b), respectively, but for the term $C\hat{W}(\overline{\mathrm{SST}-\mathrm{SAT}})$ in decomposition (2.8). (e) (f) Same as in (a) and (b), respectively, but for the term $C\overline{W^*}(\overline{\mathrm{SST}-\mathrm{SAT}})$ in decomposition (2.8). (g) (h) Same as in (a) and (b), respectively, but for the term $C\overline{(W^*)'(\mathrm{SST}-\mathrm{SAT})'}$ in decomposition (2.8). On all the panels, SST is superimposed with the contours (every 3 °C).

c Seasonal cycle of LCF in the subtropical South Indian Ocean

To discuss the seasonality of LCF and its longitudinal distribution across the subtropical basin of the South Indian Ocean, longitude-time sections of climatological-mean LCF and the corresponding meteorological and oceanic variables are shown in Fig. 2.10. The figure reveals complex relationships of LCF with meteorological parameters in the course of its seasonal cycle over the subtropical South Indian Ocean. EIS is larger in summer than in winter within the eastern subtropics (95°E-110°E, Fig. 2.10b), which seems consistent with the winter-summer difference in LCF shown in Figs. 2.5a-b. As evident in Fig. 2.10a, however, in addition to its primary maximum in summer, LCF exhibits a secondary maximum in winter, which is not fully explained by EIS (Fig. 2.10b). In the western and central subtropics (50°E-90°E), wintertime EIS is slightly higher than its summertime counterpart, which is again seemingly consistent with the winter-summer difference in LCF (Figs. 2.5a-b). Despite the well-defined wintertime maximum in LCF, however, EIS maximizes in spring but not in winter.

One of the possible factors that cause the aforementioned discrepancies between EIS and LCF in the subtropics may be SHF. It maximizes in winter (Fig. 2.10e), which can facilitate the formation of shallow convective clouds and thereby increase LCF in winter despite the spring maximum of EIS (Fig. 2.10b). Another contributor to the wintertime enhancement of LCF is probably SST. Climatologically SST is the lowest in August and September (Fig. 2.10c) after wintertime deepening of the ocean mixed layer and resultant increase in thermal inertia. In addition to the decreased insolation and the increased thermal inertia, turbulent heat loss (Figs. 2.5g-j) associated with the enhanced cold advection and scalar wind speed in winter as discussed later can further lower SST.

In the presence of negative dependence of LCF on SST (e.g., Rieck et al. 2012; Brient and Bony 2013; Bretherton and Blossey 2014; Qu et al. 2014, 2015; Seethala et al. 2015; McCoy et al. 2017), relatively cool SST in winter can contribute to an increase of LCF. At the same time, the decline of SST from late autumn into early spring acts to increase EIS continuously into early spring.

700-hPa subsidence is enhanced in winter between 50°E and 90°E (Fig. 2.10e) in accordance with the westward shift of the Mascarene high (Fig. 1.3d). The enhanced zonal-mean Hadley circulation in the winter hemisphere explains half of the wintertime subsidence, while the remaining half is associated with the subtropical high as a planetary-wave component, whose dynamics is discussed in Chapter 3. As shown by Myers and Norris (2013), enhanced subsidence under fixed EIS can contribute to the wintertime reduction of LCF, while acting to increase EIS by raising free-tropospheric temperature adiabatically. Consistent with the seasonality of subsidence, free-tropospheric relative humidity tends to be lower in winter than in summer (Fig. 2.10f), which may also possibly act to reduce wintertime LCF (e.g., Bretherton et al. 2013; van der Dussen et al. 2015). We thus conjecture that the wintertime enhancement of LCF may be caused by the enhanced SHF under the lowering SST.

To discuss why SHF is enhanced over the almost entire subtropical basin in winter, near-surface temperature advection due to climatological-mean wind and temperature is calculated. In summer, the Mascarene high resides over the eastern portion of the basin, and enhanced cold advection is limited off the west coast of Australia (Fig. 2.7c), resulting in locally enhanced upward SHF. Equatorward of 30°S, as the Mascarene high shifts westward into winter, cold advection occurs almost entirely across the basin (Fig. 2.7d).

Our additional calculation reveals that almost 40% of the wintertime cold advection is attributable to zonal-mean meridional temperature gradient and equatorward wind.

The wintertime enhancement of storm-track activity (Figs. 1.3b and 1.3e; Nakamura and Shimpo 2004) also contributes to the enhanced SHF in the wintertime subtropics (Figs. 2.5i-j and 2.10d). As shown in Figs. 1.3f, a subtropical SST front forms in winter around 30°S extending zonally across the basin (Graham and De Boer 2013). The subtropical SST front can also be seen in summer (Fig. 1.3c), although its latitude is slightly poleward if compared with the wintertime counterpart, and is not well isolated from the Agulhas SST front. Along the warmer flank of this subtropical SST front, the climatological-mean surface cold advection is augmented in winter (Fig. 2.7b), due to temporally enhanced southerlies associated with sub-monthly atmospheric disturbances (Fig. 2.7f) and due to the climatological-mean southerlies across the subtropical SST front associated with the Mascarene high (Fig. 2.7d). Note that SHF tends to be larger in winter than in summer (Figs. 2.5g-h), although climatological-mean cold advection along the west coast of Australia is slightly larger in summer than in winter (Figs. 2.7a-b). This is probably due to the heated Australian continent in summer, which reduces SST – SAT around the continent (not shown).

Furthermore, fluctuations in surface winds also act to augment surface scalar wind speed. Dependence of wintertime SHF on fluctuating surface winds is shown in Fig. 2.11 along the equatorward flank of the subtropical SST front. Meridional winds strongly fluctuate with a standard deviation of 4.6 m s^{-1} around the climatological-mean southerlies (+1.9 m s^{-1}), and scalar wind speed is enhanced temporally under both strong northerlies and southerlies (Fig. 2.11c), which is analogous to the situation along the warmer side of the Agulhas SST front in summer (Fig. 2.8c). Given the large positive value of SST−SAT under the enhanced southerlies and its strongly reduced values under the enhanced northerlies (Fig. 2.11b), upward SHF strongly increases under the enhanced southerlies while its reduction is modest under the enhanced northerlies (Fig. 2.11a), resulting in the net positive contribution from transient atmospheric eddies to the climatological-mean SHF. Similarly, SHF is enhanced under both strong easterlies and westerlies (Fig. 2.11d) due to nonlinear dependence of scalar wind speed (Fig. 2.11f), combined with the corresponding weak dependence of SST−SAT on the zonal wind velocity (Fig. 2.11e). Note that LHF is also enhanced by daily fluctuations in surface winds through the nonlinear increase in scalar wind speed (not shown). This augmentation of SHF by sub-monthly fluctuations can be confirmed through Figs. 2.9b,d,f,h. Comparison between Figs. 2.9b and 2.9d reveals that the climatological-mean Trades associated with the Mascarene high make the dominant contribution to the reconstructed climatological-mean SHF ($\mathrm{SHF_r}$) around 15°S-25°S. Around 30°S, almost the two thirds of the climatological-mean $\mathrm{SHF_r}$ is accounted for by the sub-monthly wind fluctuations (Fig. 2.9f), as is already noted in Section 2.3b. The corresponding augmentation of SHF by sub-monthly atmospheric disturbances is much weaker in summer than in winter (Figs. 2.9e-f) under the weaker eddy activity (Fig. 1.3b) and the poleward-shifted subtropical SST front (Fig. 1.3c).

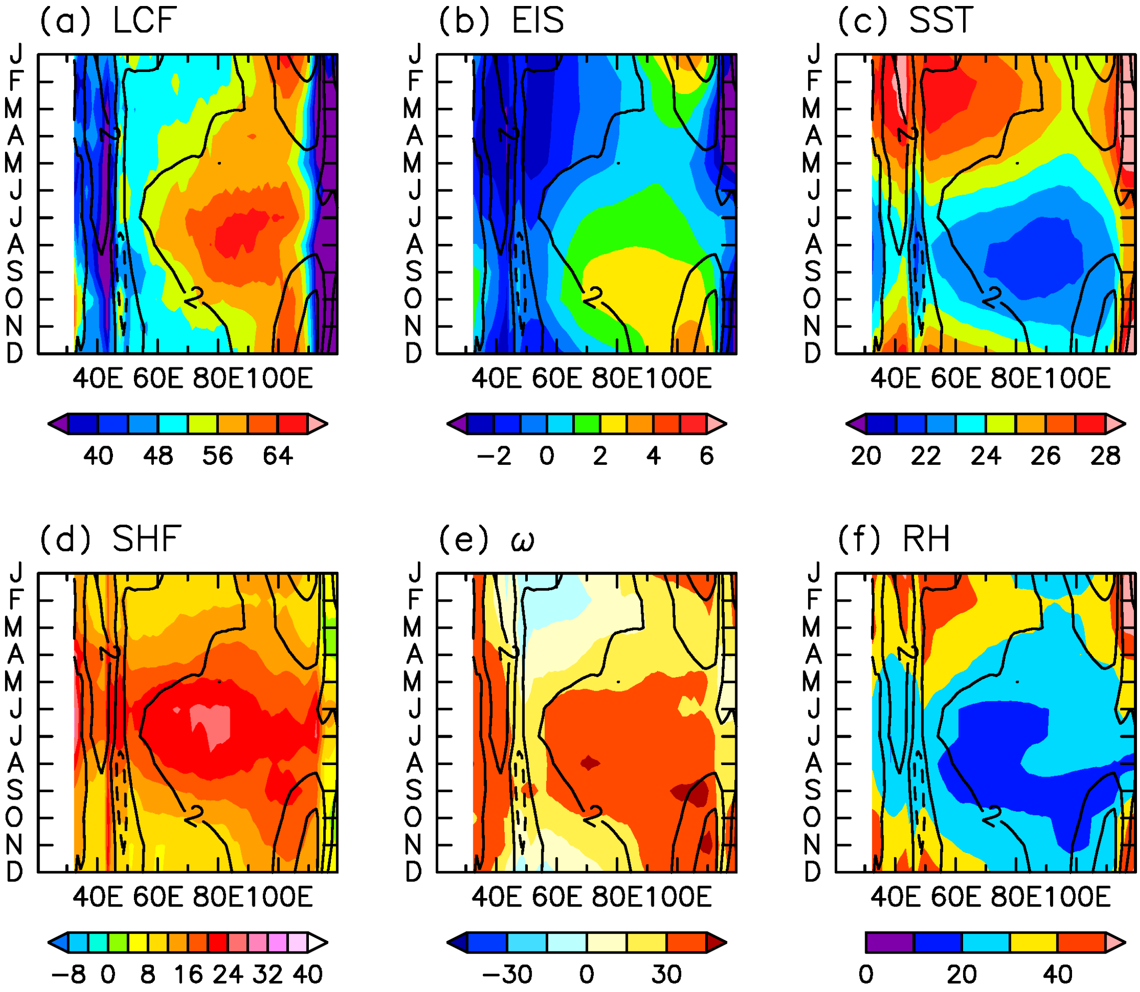

Figure 2.10: Climatological-mean seasonal cycle of the longitudinal distributions of (a) LCF (color shaded for every 4 %), (b) EIS (color shaded for every 1 K), (c) SST (color shaded for every 1 °C), (d) SHF (color shaded for every 4 W m^{-2}), (e) 700-hPa ω (color shaded for every 15 hPa day^{-1}), (f) 700-hPa RH (color shaded for every 10 %) across the subtropical basin of the South Indian Ocean averaged between 15.5°S and 29.5°S. For each of the panels, the coloring convention is indicated at the bottom, and the contours indicate the corresponding seasonal cycle of the meridional component of surface winds (every 2 m s^{-1}; positive values for the southerlies).

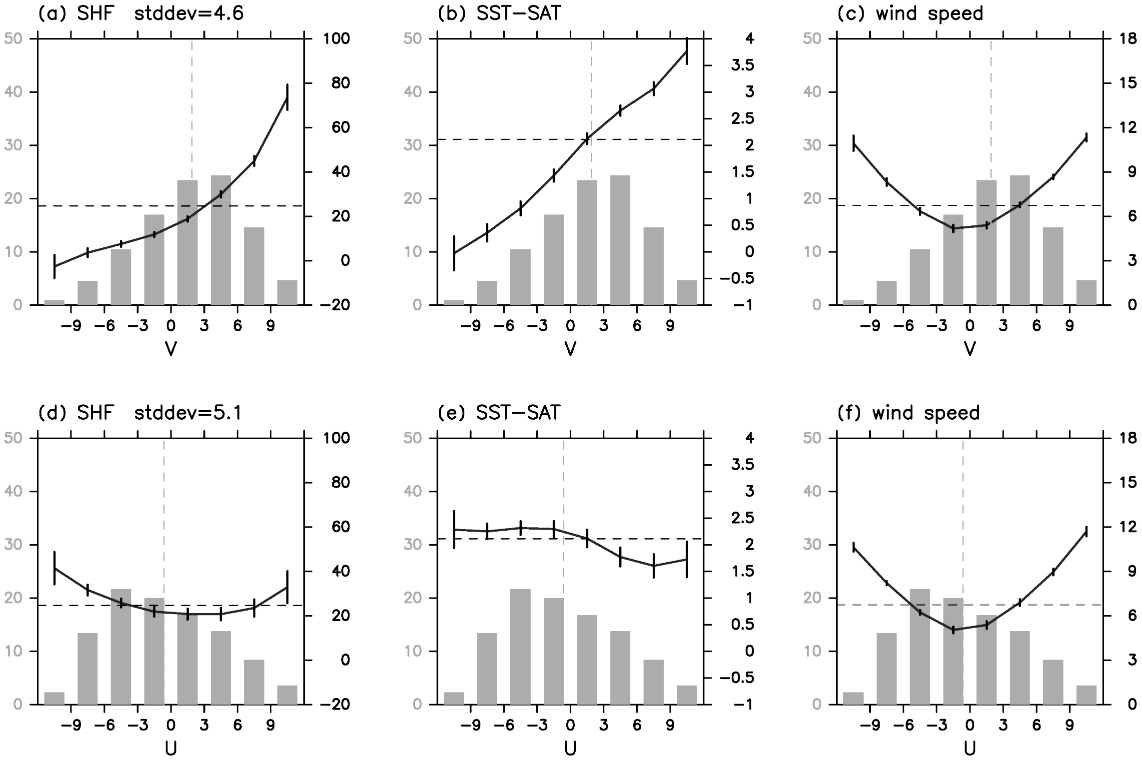

Figure 2.11: (a) Same as in Fig. 2.8, but for JJA along the equatorward flank of the subtropical SST front [60.5°E-109.5°E, 27.5°S-29.5°S, ST].

2.4 Discussion

a Relative importance of individual cloud-controlling factors

As shown in the preceding section, SHF, SST and EIS act to increase LCF in winter across the subtropical South Indian Ocean basin under the westward extension and intensification of the Mascarene high and the enhancement of storm-track activity. One may question the relative importance of the contributions from SHF, SST and EIS to the wintertime enhancement of LCF. To quantify the relative contributions, LCF is reconstructed through a multiple linear regression model as described in detail in Appendix B. The regression slope obtained for the LCF variations against each of the predictors of the model is given in Table B.1. Figure 2.12 shows the longitude-time sections of the predicted climatological seasonal cycle of LCF between 15.5°S and 29.5°S. The multiple linear regression model explains 64% of the total variance of regionality of LCF and its seasonal cycle, whereas root mean square error between the observed LCF and the predicted LCF is 7%. Most importantly, the model well reproduces the wintertime LCF maximum from July to September in the western and central subtropics (Figs. 2.12a-b). In the eastern subtropics [100°E-110°E], the predicted summertime LCF maximum (Fig. 2.12b) is underestimated (Fig. 2.12a). Nevertheless, the zonal contrast in LCF in summer is still reproduced by the model. Reconstruction of LCF is not successful near the coasts, which is not our primary focus.

The reconstruction indicates that in the subtropics EIS (Fig. 2.12c) and SST (Fig. 2.12d) make main contributions to the late winter enhancement of LCF (Fig. 2.12b), while the contribution from SHF is of primary importance in the midwinter LCF maximum

(Fig. 2.12e). By contrast, 700-hPa relative humidity acts to reduce LCF in winter (Fig. 2.12g). The direct impact of the 700-hPa subsidence appears to be negligible (Fig. 2.12f), although the enhanced subsidence (Fig. 2.10f) may influence the wintertime increase in LCF indirectly through EIS. Meanwhile, the summertime LCF maximum off the west coast of Australia is attributable mostly to the enhanced EIS (Figs. 2.12b-c). Nevertheless, lower SST (Fig. 2.12d) and enhanced SHF (Fig. 2.12e) in the eastern portion of the basin compared with the western portion act to augment the zonal LCF contrasts in summer.

Seasonal cycle of ECTEI further supports the importance of SHF. Figure 2.13 shows the climatological-mean distribution of ECTEI over the South Indian Ocean, while Fig. 2.14 shows its seasonal cycle over the subtropical basin. Since ECTEI incorporates the effect of moisture gap across the cloud-top as well as the strength of temperature inversion (Kawai et al. 2017), ECTEI combines the direct effects of EIS, SST and free-tropospheric relative humidity. In the summertime subtropical basin, ECTEI shows a local maximum off the west coast of Australia (Fig. 2.13a) due to large EIS (Fig. 2.13c) with an additional contribution from weaker moisture stratification (Fig. 2.13e), to which the local minimum of SST (Fig. 2.13e) contributes through the nonlinearity of the Clausius-Clapeyron relation (Kawai et al. 2017). In winter, ECTEI is zonally more uniform across the subtropical basin (Fig. 2.13b), consistent with the zonal uniformity of EIS (Fig. 2.13d) and moisture stratification (Fig. 2.13f). Longitude-time distribution of ECTEI shows a prolonged maximum from August to October (Fig. 2.14a), which shows better correspondence with LCF (Fig. 2.10a) than EIS (Fig. 2.14b). This improvement is due to the reduced moisture stratification in winter (Fig. 2.14c), consistent with seasonal lowering of SST. Still, the maximum of ECTEI is lagged behind the LCF maximum, implying again the importance of the wintertime enhancement of SHF.

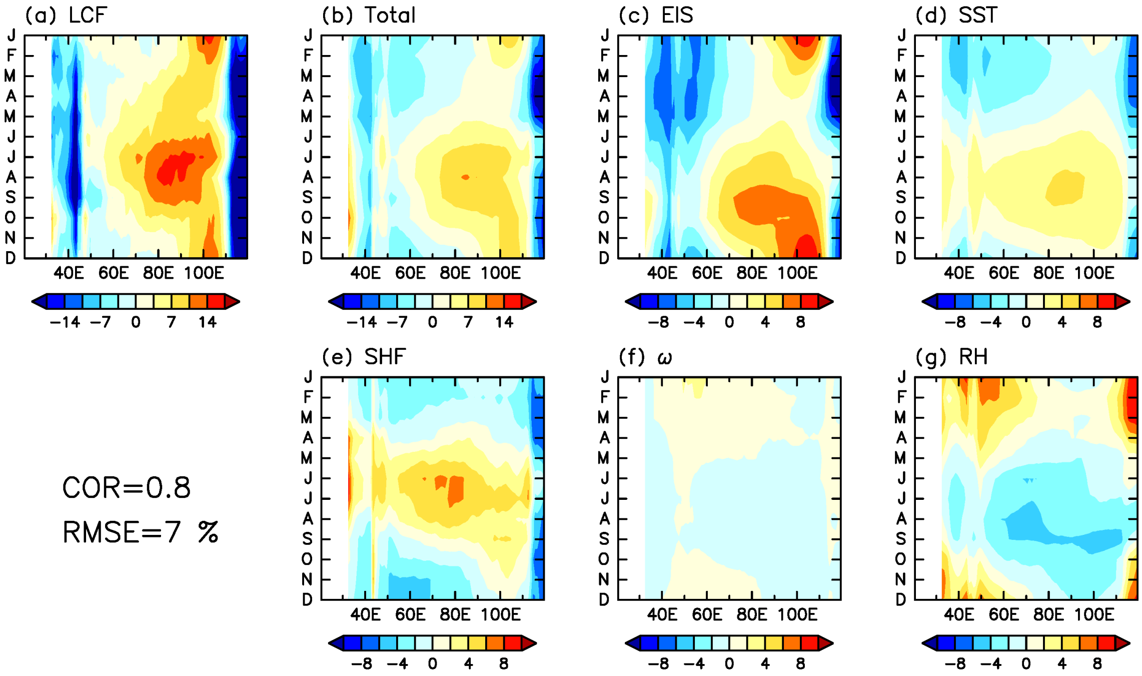

Figure 2.12: (a) Same as in Fig. 2.10a, but from which the annual-mean LCF within the domain has been removed. (b) Same as in (a), but for the corresponding LCF predicted by the multiple linear regression model described in Appendix B. The correlation and root mean square error (RMSE) between (a) and (b) are shown below (a). (c-g) Same as in (b), but for the individual contributions from EIS, SST, SHF, 700-hPa ω, and 700-hPa RH, respectively, to (b), respectively.

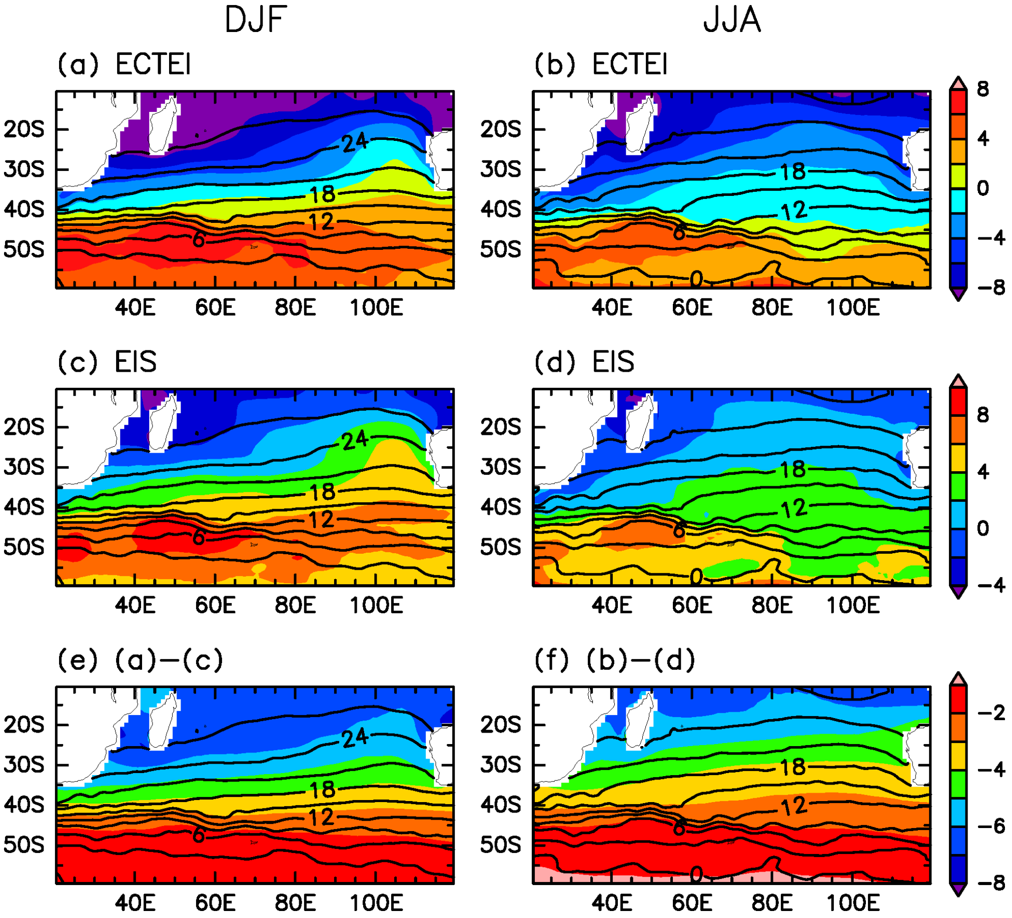

Figure 2.13: Same as in Fig. 2.5a, but for (a) ECTEI (color shaded for every 1 K), (c) EIS (color shaded for every 1 K), and (e) (a)−(c) which represents the contribution from moisture stratification (color shaded for every 1 K). (b,d,f) Same as in (a), (c) and (e), respectively, but for austral winter (JJA). On all the panels, SST is superimposed with the contours (every 3 °C).

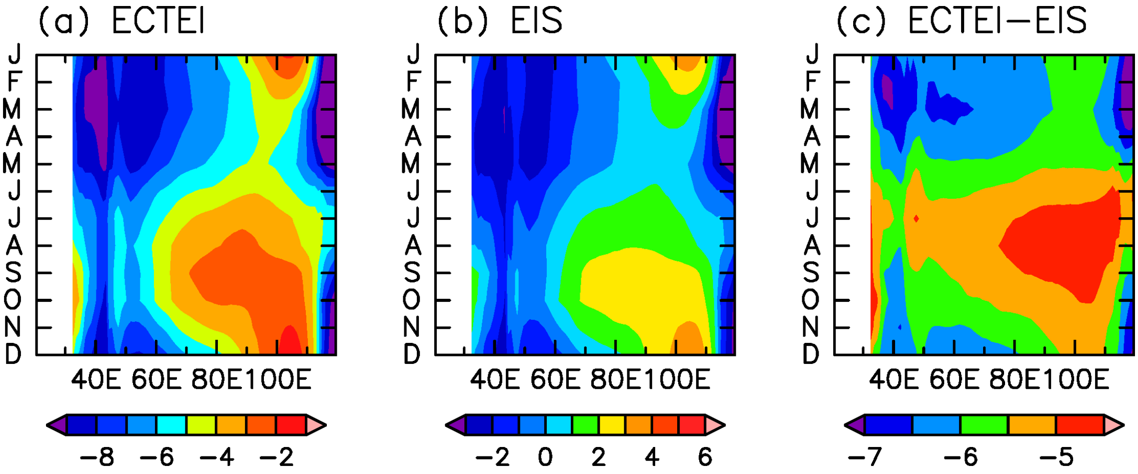

Figure 2.14: Same as in Fig. 2.10a, but for (a) ECTEI (color shaded for every 1 K), (b) EIS (color shaded for every 1 K), and (c) (a)−(b) which represents the contribution from moisture stratification (color shaded for every 0.5 K).

b Summertime LCF around the Agulhas SST front in an AGCM

Here, we compare two AFES experiments to confirm the impacts of the Agulhas SST front on LCF as discussed in Section 2.3b. Figure 2.15 shows meridionally high-pass-filtered summertime climatologies of LCF in the two AFES experiments and their difference. AFES_CTL reproduces the local maximum along the warmer flank of the Agulhas SST front (Fig. 2.15a), while it is totally missing in AFES_SMTH due to the weakened SST front (Fig. 2.15b). Thus, the difference in the frontal intensity between the AFES experiments (Fig. 2.15c) is closer to that of the MODIS observations around the Agulhas SST front (Fig. 2.6a). Figures 2.16 and 2.17 show meridionally high-pass-filtered summertime climatologies of EIS and SHF in the AFES experiments and their difference, respectively. AFES_CTL simulates the local minimum of EIS and maximum of upward SHF over the local maximum of SST (Figs. 2.16a and 2.17a), as in the ERA-Interim data (Figs. 2.6b,d). Removal of the frontal SST gradient leads to the meridionally more uniform distributions (Figs. 2.16b-c and 2.17b-c), which is consistent with the absence of any local maximum of LCF (Fig. 2.15b). Though not shown, poleward heat transport by 8-day high-pass-filtered wind and temperature fluctuations across the SST front is stronger in AFES_CTL with the enhanced SST gradient and wind fluctuations. Thus the AFES experiments further support our notion that the local enhancement of LCF along the warmer flank of the Agulhas SST front reflects the local maximum of SHF induced by the frontal SST gradient and the enhanced storm-track activity despite the reduced EIS over the warmer Agulhas Return Current.

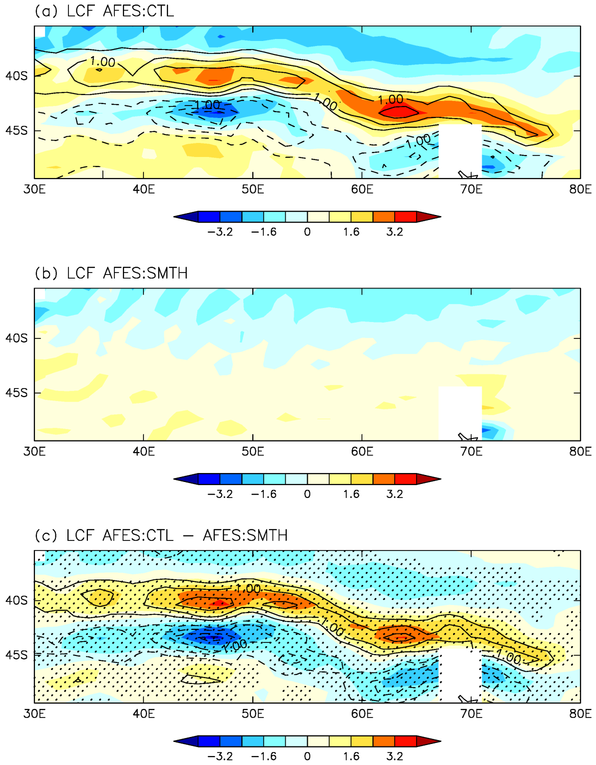

Figure 2.15: (a) Meridionally high-pass-filtered fields of LCF (color shaded for every 0.8 %) around the SST front for austral summer (DJF) in AFES_CTL. Superimposed with the contours is meridionally high-pass-filtered climatological SST (every 0.5 °C; solid and dashed lines for positive and negative values, respectively; zero contours are omitted) for DJF. Local departures of each variable from its meridional nine-point running-mean values are regarded as the meridionally high-pass-filtered component. (b) Same as in (a), but for AFES_SMTH. (c) Same as in (a), but for the difference defined as AFES_CTL−AFES_SMTH. Stippling indicates the 99% confidence for the difference.

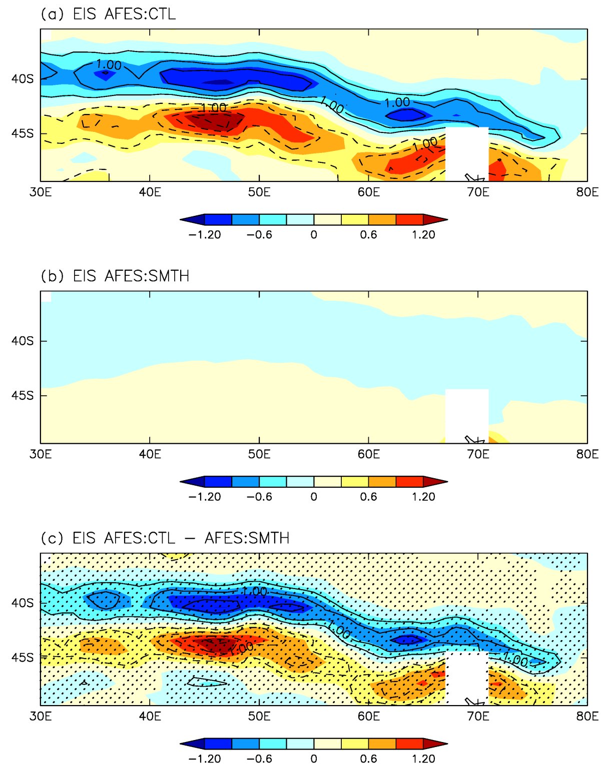

Figure 2.16: Same as in Fig. 2.15, but for EIS (color shaded for every 0.3 K).

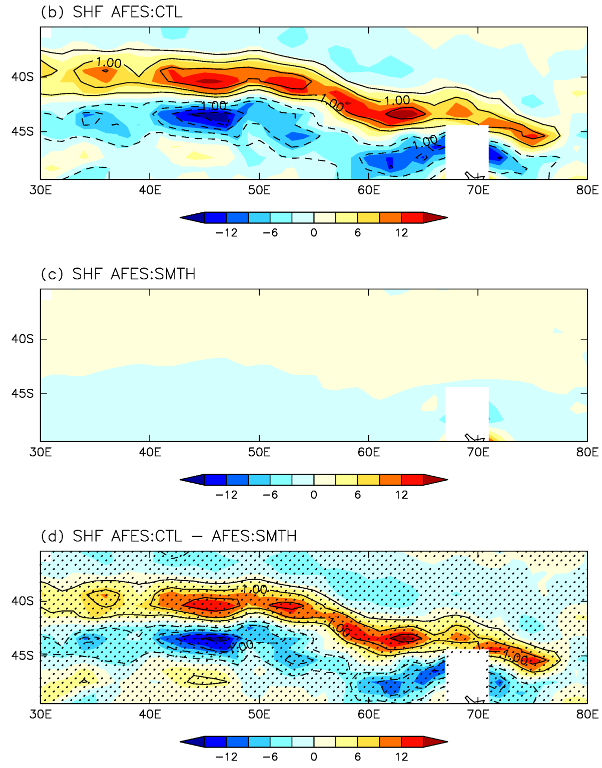

Figure 2.17: Same as in Fig. 2.15, but for SHF (color shaded for every 3 W m^{-2}).

c LCF over the subpolar ocean

Over the South Indian Ocean poleward of 50°S, summertime EIS decreases slightly with latitude, probably due to the stronger latitudinal decrease in free-tropospheric temperature than in SST (Figs. 2.5a and 2.5c). No corresponding latitudinal decrease is observed in LCF with its extremely large values distributed over the subpolar oceans (Fig. 2.5a). One possible contributor may be poleward decrease in SST (Fig. 2.5a), and another possible contributor is poleward increase in free-tropospheric relative humidity (Fig. 2.5e). The latter may weaken the entrainment drying and thus act to increase LCF (e.g., Bretherton et al. 2013; van der Dussen et al. 2015), although the origin of the high relative humidity is not clear. The low SST and high free-tropospheric relative humidity act to increase ECTEI (Fig. 2.13e), although ECTEI does not actually increases poleward (Fig. 2.13a). Note that the wintertime situation (Figs. 2.5b,d,f and Figs. 2.13b,d,f) is similar to the summertime counterpart, but the wintertime LCF is probably not reliable as discussed in Section 2.3a.

d Radiative properties of low-level clouds

In this subsection, we discuss the radiative impacts of LCF on planetary albedo. Figure 2.18 shows the climatological winter/summer distributions of LCF, optical depth τ and planetary albedo over the South Indian Ocean, while Fig. 2.19 shows their climatological seasonal cycles across the subtropical basin. Since cloud albedo is linear in log(τ) over a wide range of τ, climatological-mean "radiatively effective" optical depth is derived as

$$\overline{\tau} = 10^{\overline{\log_{10}(\tau)}} \tag{2.9}$$

where overbar denotes time averaging (Pincus et al. 2012). Although scenes with mid- and/or high-level clouds are discarded in making their climatologies, climatological-mean LCF and its seasonal cycle are still similar to those obtained under random overlap assumption (Figs. 2.5a-b and 2.10a).

In the subtropics, planetary albedo exhibits a local maximum off the west coast of Australia in summer (Figs. 2.18e and 2.19c), while the albedo increases with enhanced zonal uniformity in winter (Figs. 2.18f and 2.19c). This seasonality is consistent with that of LCF (Figs. 2.18a-b and 2.19a), suggesting the importance of albedo effect of low-level clouds through their fractional coverage. In fact, the pattern correlation between Figs. 2.19a and 2.19c is very high ($r = 0.81$).

By contrast, horizonal distribution of τ is slightly different from that of LCF and albedo. In summer, optical depth is large not only off the west coast of Australia but also equatorward of 25°S in the western and central portion of the basin (Fig. 2.18c). In winter, optical depth is horizontally uniform within the subtropics (Fig. 2.18d), which is similar to LCF and albedo. Seasonality of "radiatively effective" τ is not pronounced as LCF (Fig. 2.19b), leading to weaker pattern correlation with albedo ($r = 0.62$).

To discuss the seasonality in the horizonal distribution of τ in more detail, we derive LWP and N_c, and their seasonal cycles are shown in Fig. 2.20. Interestingly, LWP is maximized in late autumn to early winter (Fig. 2.20a), which precedes the LCF maximum in midwinter (Fig. 2.19a). In summer, LWP is small even off the west coast of Australia, where LCF has its maximum. Those differences imply that large-scale controls on LCF and LWP are not the same, as is suggested by van der Dussen et al. (2015). They showed that LWP is rather insensitive to lower-tropospheric stability, but increases significantly and almost linearly with free-tropospheric humidity, although the wintertime maximum of LWP is not explained by free-tropospheric humidity, which exhibits its minimum in winter (Fig. 2.10f). Meanwhile, area of high N_c is observed in summer off the west coast of Australia (Fig. 2.20b), which can locally lead to smaller τ (Fig. 2.19a) along with smaller LWP (Fig. 2.20a). This high N_c may be due to the intrusion of continental air into the South Indian Ocean. In early winter, larger LWP and smaller N_c observed across the subtropical basin are not fully reflected into larger "radiatively effective" τ, presumably because large day-to-day variations act to reduce "radiatively effective" τ through the non-linear relationship between cloud albedo and τ (Pincus et al. 2012).

Over the summertime midlatitude and subpolar oceans, albedo is higher than the subtropics with zonal uniformity (Fig. 2.18e), which is again consistent with LCF (Fig. 2.18a). Larger τ over the summertime midlatitude and subpolar oceans can also contribute to the high albedo there (Fig. 2.18c). Radiative properties of low-level clouds around the Agulhas SST front are highlighted in Figs. 2.21 and 2.22. Albedo is higher along the warm Agulhas Return Current than the cooler side of the SST front (Fig. 2.21c), which is consistent with larger LCF (Fig. 2.21a). τ is also lager larger along the warm current (Fig. 2.21b), acting to further enhance albedo. As shown in Fig. 2.22a, larger LWP is observed along the warm current (Fig. 2.22a). The reason of large LWP is not clear, but it may be due to warm SST and/or enhanced upward SHF (Fig. 2.6d). Meanwhile, cross-frontal contrast in N_c is less pronounced (Fig. 2.22b) than the other variables. Koike et al. (2012, 2016) showed that enhanced shallow convection promotes enhanced activation of small aerosols, resulting in larger N_c along the warm Kuroshio Current. The reason of no marked enhancement of N_c over the warm Agulhas Return Current is not clear at this stage, but presumably it may be due to insufficient supply of continental air mass that is rich in small-size aerosols.

Overall, the distribution of planetary albedo is consistent with that of LCF, while τ is not necessarily consistent with the distribution of albedo. This is because large-scale controls on LWP and N_c can be different from those on LCF. Those large-scale controls on LWP and N_c will be investigated in the future.

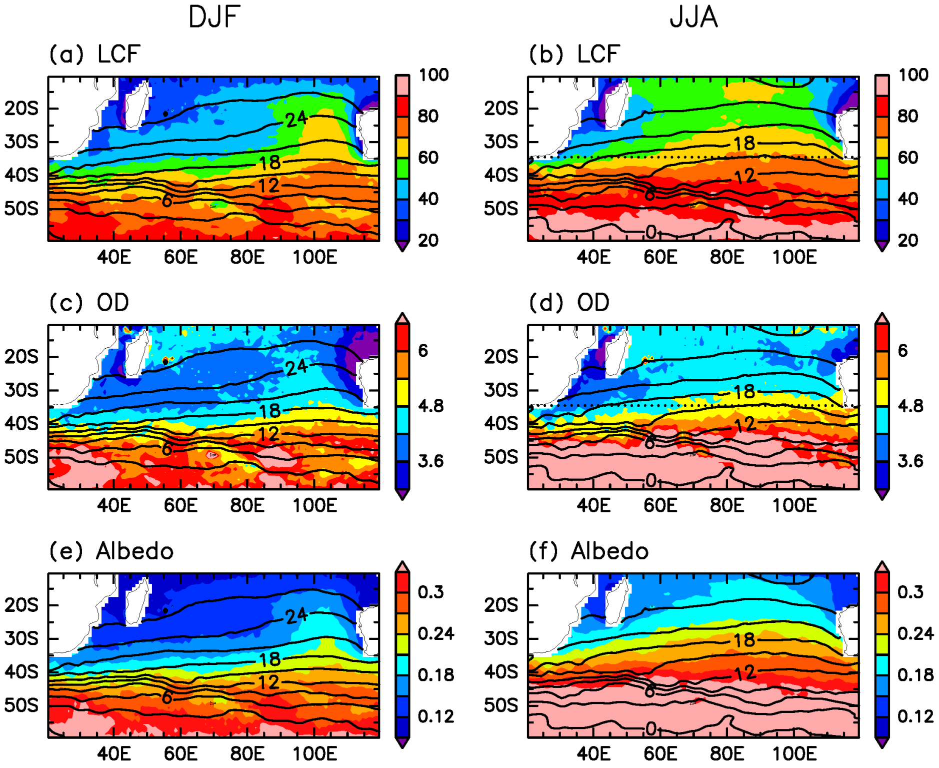

Figure 2.18: Same as in Fig. 2.5a, but for (a) LCF (color shaded for every 10 %), (c) radiatively effective cloud optical depth (color shaded for every 0.6), and (e) planetary albedo (color shaded for every 0.03). (b,d,e) Same as in (a), (c) and (e), respectively, but for austral winter (JJA). On all the panels, SST is superimposed with the contours (every 3 °C).

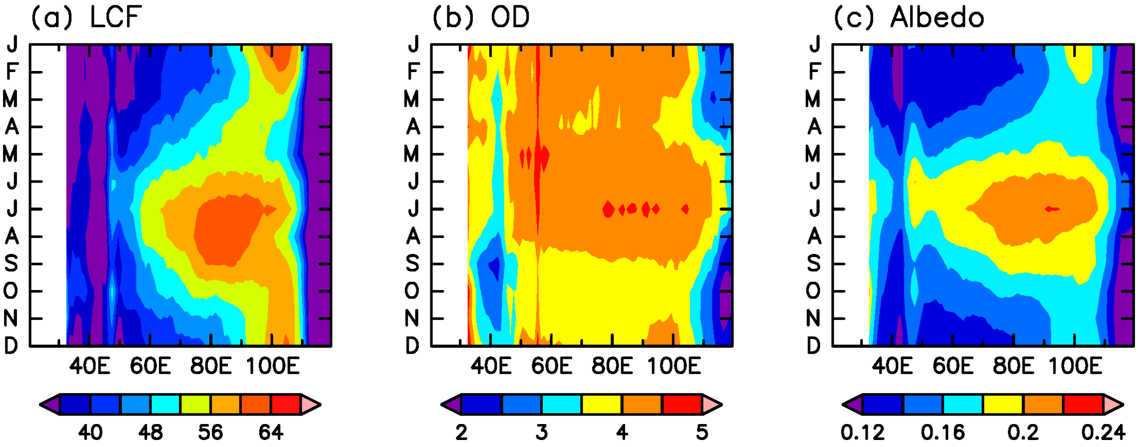

Figure 2.19: Same as in Fig. 2.10a, but for (a) LCF (color shaded for every 4 %), (b) radiatively effective cloud optical depth (color shaded for every 0.5), and (c) planetary albedo (color shaded for every 0.02).

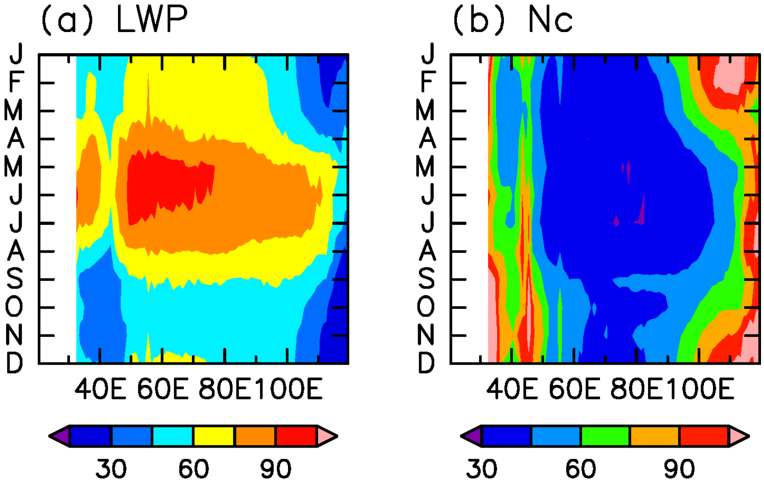

Figure 2.20: Same as in Fig. 2.10a, but for (a) LWP (color shaded for every 15 $\mathrm{g\,m^{-2}}$) and (b) N_c (color shaded for every 15 $\mathrm{cm^{-3}}$).

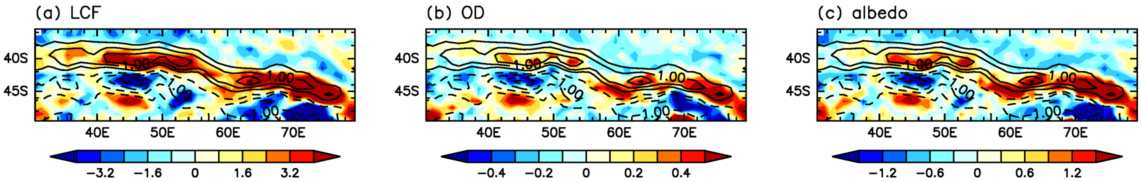

Figure 2.21: Same as in Fig. 2.6a, but for (a) LCF (color shaded for every 0.8 %), (b) radiatively effective cloud optical depth (color shaded for every 0.1), and (c) planetary albedo (color shaded for every 0.3×10^{-2}). Superimposed with the contours is meridionally high-pass-filtered climatological SST (every 0.5 °C; solid and dashed lines for positive and negative values, respectively; zero contours are omitted) for DJF.

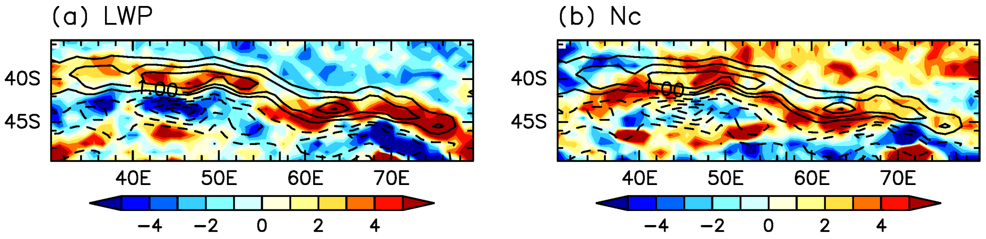

Figure 2.22: Same as in Fig. 2.6a, but for (a) LWP (color shaded for every 1 $\mathrm{g\,m^{-2}}$) and (b) N_c (color shaded for every 1 $\mathrm{cm^{-3}}$). Superimposed with the contours is meridionally high-pass-filtered climatological SST (every 0.5 °C; solid and dashed lines for positive and negative values, respectively; zero contours are omitted) for DJF.

e Comparison with the South Atlantic and the South Pacific

Finally, the same analysis above is applied to the other basins in the Southern Hemisphere, in comparison with the South Indian Ocean. Figures 2.23 and 2.24 show the climatological-mean distributions of LCF and related meteorological and oceanic variables in the South Atlantic and the South Pacific, respectively. In summer, the climatological-mean distributions of LCF in the South Atlantic (Fig. 2.23a) and the South Pacific (Fig. 2.24a) are similar to that in the South Indian Ocean (Fig. 2.5a). LCF in the South Atlantic and Pacific maximizes off the west coast of South Africa between 15°S and 25°S and South America between 15°S and 30°S, respectively, and LCF further increases with latitude poleward of 35°S over the two basins. These LCF distributions are well explained by EIS (Figs. 2.23c and 2.24c). An exception is, however, found just off the west coast of South Africa around 30°S where LCF is minimized locally (Fig. 2.23a) under high EIS but locally suppressed SHF due perhaps to coastal upwelling. Another exception is found just to the south of South Africa, where relatively large LCF is observed in association with a local minimum of EIS but a local maximum of SHF due to the retroflecting warm Agulhas Current. These exceptions seem to suggest importance of SHF as a controlling factor of LCF.

A local summertime maximum of EIS in the eastern portion of each of the subtropical basins coincides with a local maximum of θ_{700} (Figs. 2.23c and 2.24c) and nearly so with a local minimum of SST (Figs. 2.23a and 2.24a). The former is associated with locally enhanced 700-hPa subsidence (not shown) east of a subtropical high. In neither of the South Atlantic (Fig. 2.23e) and Pacific (Fig. 2.24e), the near-surface cold advection in summer over the eastern portion over the subtropical basin is not as strong as over the South Indian Ocean (Fig. 2.7c), despite the strong southeasterly Trades off the coast associated with the subtropical high (Figs. 2.23f and 2.24f). The weaker cold advection is due to the weaker gradient of underlying SST in the eastern portions of the South Atlantic (Fig. 2.23a) and Pacific (Fig. 2.24a) than in the South Indian Ocean (Fig. 2.5a). Correspondingly, the local enhancement of summertime SHF off the west coast of South Africa (Fig. 2.23g) and South America (Fig. 2.24g) is less obvious than in the South Indian Ocean (Fig. 2.5g).

Although the spatial distributions of the climatological-mean LCF in summer overall correspond well with those of EIS for both the South Atlantic and the South Pacific (Figs. 2.23 and 2.24, respectively), regions around oceanic frontal zones can be exceptions as discussed in Section 2.3b for the South Indian Ocean (Figs. 2.5 and 2.6). We have shown that both the pronounced SST gradient and enhanced storm-track activity act to increase LCF along the warmer side of the Agulhas SST front. As evident in Figs. 1.3c and 1.3f, areas of strong meridional SST gradients are also observed in the other basins. Though not as pronounced as the Agulhas SST front, the Brazil-Malvinas fronts are located in the western South Atlantic around 35°W-50°W (Tokinaga et al. 2005). Over the warmer side of each of these two SST fronts, upward SHF is locally enhanced (Fig. 2.23g), which can be confirmed in the meridionally high-pass-filtered fields (Fig. 2.25c). The locally enhanced SHF coincides with the enhanced LCF (Fig. 2.25a). This suggests the formation of shallow convective clouds facilitated under the enhanced SHF along the warm Brazil Current, despite the local minimum of EIS (Fig. 2.25b) that acts to reduce LCF. We have confirmed that augmentation of SHF by sub-monthly atmospheric disturbances is essential for the large SHF over the warmer side of each SST front (not shown). The cross-frontal SHF gradient is also strong around [55°S, 140°W-170°W] in the South Pacific (Fig. 2.24g), although the corresponding impact on LCF is found to be rather modest (not shown). In summary, the combined impacts of frontal SST gradient and sub-monthly atmospheric disturbances on LCF, as discussed in Section 2.3b for the South Indian Ocean, can also be seen in the South Atlantic and the South Pacific, although the impacts are not as prominent as around the Agulhas SST front.

The right columns of Figs. 2.23 and 2.24 show the climatological-mean wintertime distributions of LCF and related meteorological and oceanic variables in the South Atlantic and South Pacific, respectively. Unlike in the subtropical South Indian Ocean (Fig. 2.5b), zonal asymmetry of LCF is still evident in both the South Atlantic (Fig. 2.23b) and the South Pacific (Fig. 2.24b), as observed in summer (Figs. 2.23a and 2.24a). Correspondingly, EIS exhibits its maxima off the west coasts of South Africa and South America (Figs. 2.23d and 2.24d), collocated with the local minima of SST (Figs. 2.23b and 2.24b), as in summer (Figs. 2.23c and 2.24c). Especially, off the west coast of South Africa around between 10°S and 15°S, LCF exhibits its extreme maximum in spite of moderate EIS and SHF, in which microphysical interactions associated with a large amount of biomass-burning aerosols can play a role (Zuidema et al. 2016, Adebiyi and Zuidema 2018). Though less obvious than in summer, the local maxima of θ_{700} are also observed over the same coastal regions (Figs. 2.23d and 2.24d). Compared to the summertime situation, cold advection associated with the subtropical high is enhanced in winter in the tropics between 10°S and 20°S (Figs. 2.23f and 2.24f), resulting in local enhancement in SHF around [10°S, 10°W-10°E] in the South Atlantic (Fig. 2.23h) and around [10°S, 90°W] in the South Pacific (Fig. 2.24h). These features are all attributable to the subtropical highs that reside over the eastern portions of the South Atlantic and the South Pacific basins throughout the year, which is in sharp contrast with the South Indian Ocean (Figs. 1.3a,d). As in summer, LCF is minimized locally just off the west coast of South Africa around 30°S (Fig. 2.23b) under the locally suppressed SHF (Fig. 2.23h) despite large EIS (Figs. 2.23d). Likewise, large LCF is observed also in winter to the south of South Africa under an extreme local maximum of SHF in spite of a local EIS minimum

Compared to summer, storm-track activity is enhanced in winter across the South Atlantic and South Pacific (Figs. 1.3b,e). In the South Pacific, the primary SST front in winter is located poleward of 50°S, far south compared with the South Atlantic and the South Indian Ocean (Fig. 1.3f). Still, the storm-track activity over the South Pacific is enhanced in winter around 30°S, where upper-level eddies traveling along the subtropical jet can couple with the near-surface baroclinic zone along the modest subtropical SST front in winter (Nakamura and Shimpo 2004). In addition, quasi-stationary atmospheric eddies also contribute to the sub-monthly fluctuations in surface winds (not shown). As also observed in the South Indian Ocean (Fig. 2.5), the wintertime enhancement of surface wind fluctuations acting on the subtropical SST front with modest SST gradients around 35°S in the South Atlantic and 30°S in the South Pacific (Fig. 1.3f) can also contribute to the wintertime enhancement of SHF.

The seasonal cycles of LCF and related meteorological and oceanic variables across the subtropical basin for the South Atlantic and South Pacific are plotted in Fig. 2.26, which is compared with the corresponding plots in Fig. 2.10 for the South Indian Ocean. At 32.5°S in the South Atlantic, LCF maximizes from late winter into early spring (Fig. 2.26a), while EIS is lagged behind the wintertime maximum of LCF (Fig. 2.26b). The delay of the wintertime EIS increase relative to the LCF maximum is in common with the South Indian Ocean. By contrast, SHF is basically enhanced across the basin from late autumn to winter (Fig. 2.26e), which can act to facilitate the formation of shallow convective clouds and thereby to increase LCF in winter. This wintertime enhancement of SHF is not explained well by near-surface temperature advection due to climatological-mean winds (Fig. 2.26d), which is quite weak except over the eastern portion of the basin. We have confirmed that wind fluctuations associated with sub-monthly atmospheric disturbances acting on the SST gradient is the main contributor to the wintertime enhancement of SHF, especially along the warmer flank of the wintertime subtropical SST front (not shown). In addition, we have repeated the same analysis as in Fig. 2.9 for the South Indian Ocean, and confirmed that enhancement of SHF by sub-monthly atmospheric eddies through augmentation of surface wind speed also contributes to the wintertime enhancement of SHF (not shown). As in the South Indian Ocean, SST also minimizes in late winter (Fig. 2.26c), which can also contribute to the wintertime enhancement of LCF.

At 28.5°S in the South Pacific, the seasonal cycles of LCF, EIS, SST and SHF (Figs. 2.26f-h,j) across the basin shows some resemblance to their counterpart for the South Atlantic (Figs. 2.26a-c,e). Across the subtropical South Pacific, LCF is characterized by its prolonged maximum from winter to early spring (Fig. 2.26f), whereas EIS maximizes from spring into early summer and SST is the lowest in late winter to early spring (Figs. 2.26g-h). SHF maximizes from late autumn into late winter (Fig. 2.26j), despite no clear wintertime enhancement of cold advection due to climatological-mean winds (Fig.

2.26i). Again, this enhancement of SHF is mainly due to sub-monthly atmospheric eddies through enhancement of net cold advections as well as augmentation of surface wind speed (not shown), which may contribute to the wintertime enhancement of LCF. Overall, the unique seasonality in the position of the subtropical high characterizes the distinct seasonality in LCF over the subtropical South Indian Ocean, while basin-wide augmentation of LCF through SHF by sub-monthly atmospheric eddies can be seen in the other basins. Applying the multiple linear regression model (Table B.1) to the South Atlantic and the South Pacific, we have confirmed that the wintertime enhancement of SHF plays a role in the seasonal cycle of the midlatitude and subtropical LCF (Figs. C.6 and C.8) while EIS dominates in the seasonal cycle of LCF further equatorward (Figs. C.5 and C.7).

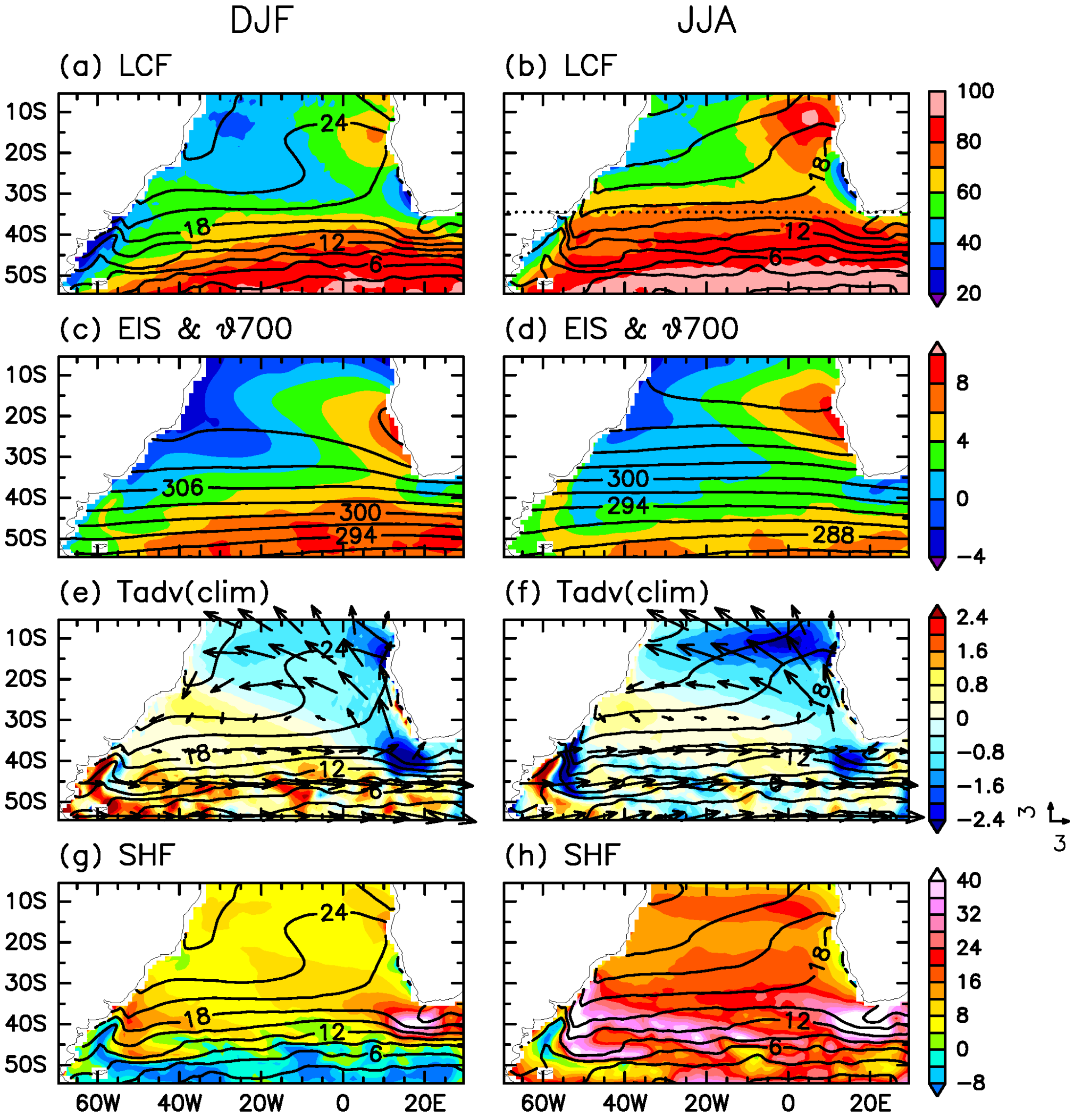

Figure 2.23: Climatological distributions for austral summer (DJF) of maritime (a) LCF (color shaded for every 10 %) and SST (contoured for every 3 °C), (c) EIS (color shaded for every 2 K) and 700-hPa θ (contoured for every 3 K), (e) near-surface temperature advection (color shaded for every 0.4 K day^{-1}), SST (contoured for every 3 °C) and surface winds (m s^{-1}, arrows), and (g) SHF (color shaded for every 4 W m^{-2}; positive values for upward flux) and SST (contoured for every 3 °C) in the South Atlantic. (b), (d), (f) and (h) Same as in (a), (c), (e) and (g), respectively, but for austral winter (JJA). In (e) and (f), the climatological-mean temperature advection is calculated only from climatological-mean winds and temperature. In (b), the dotted line indicates the latitude poleward of which more than 30% of observations were made under (daily maximum) solar zenith angles greater than 65°.

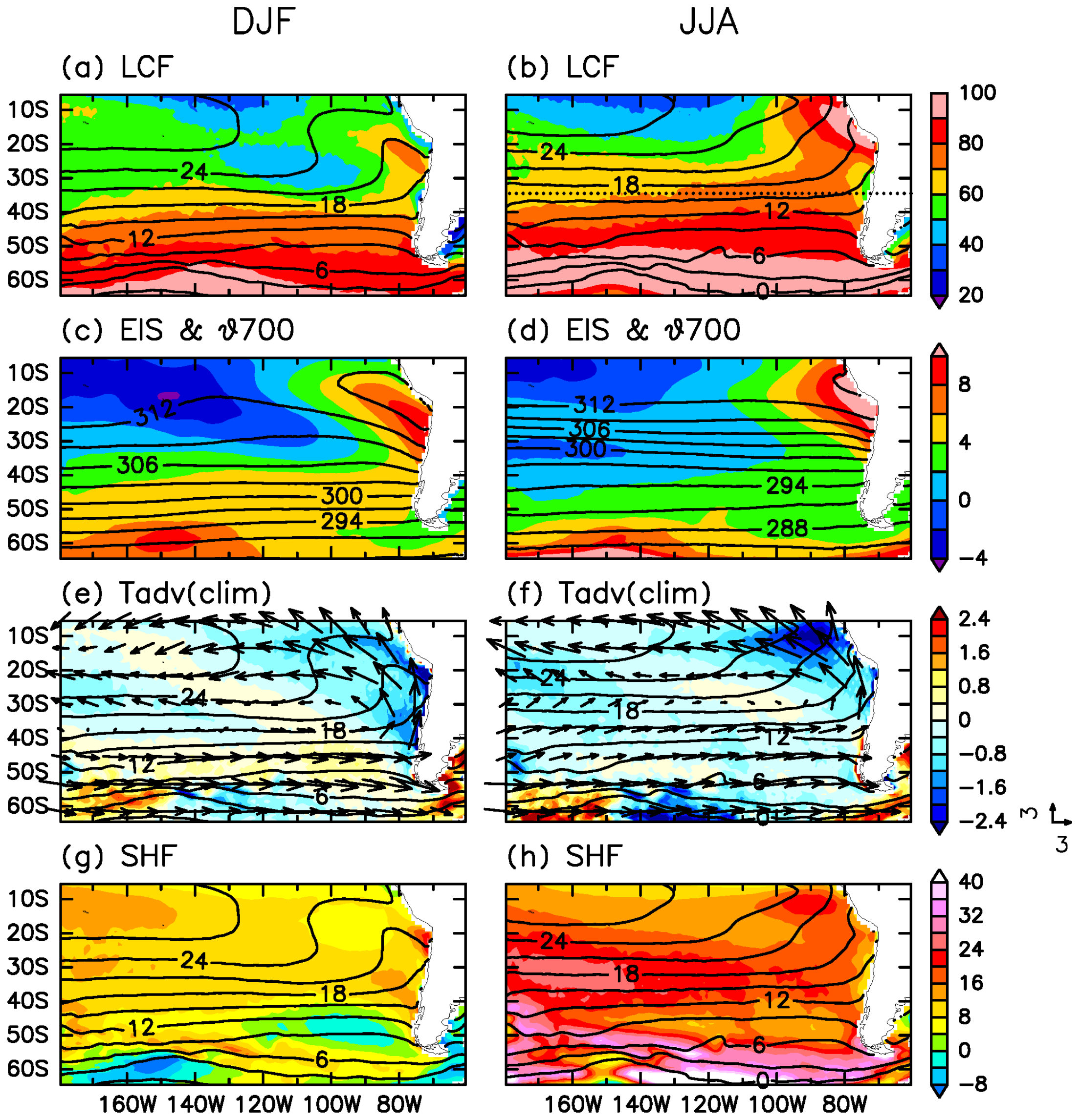

Figure 2.24: Same as in Fig. 2.23, but for the South Pacific.

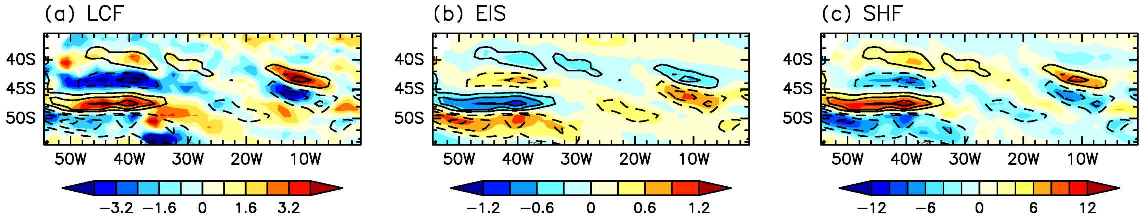

Figure 2.25: Same as in Fig. 2.6, but for (a) LCF (%), (b) EIS (K), (c) SHF (W m^{-2}) for DJF in the South Atlantic.

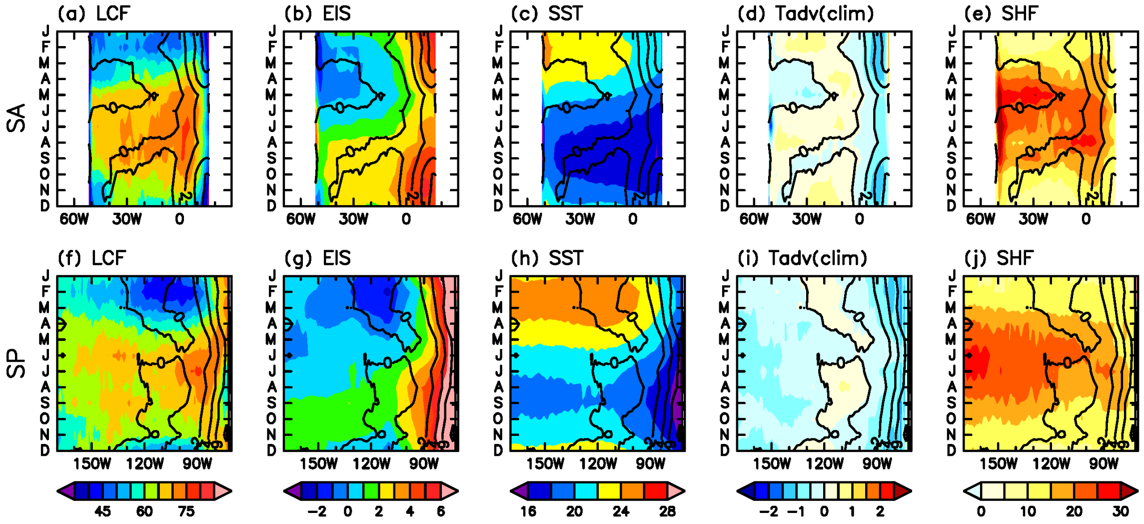

Figure 2.26: Same as in Fig. 2.10, but for (a) LCF (%), (b) EIS (K), (c) SST (°C), (d) near-surface temperature advection (K day^{-1}) and (e) SHF (W m^{-2}) at 32.5°S. (f-j) Same as in (a-e), respectively, but for 28.5°S in the South Pacific. In (d) and (i), the climatological-mean temperature advection is calculated only from climatological-mean winds and temperature.

2.5 Conclusions

In this chapter, influence of the subtropical high and storm-track activity on LCF and its seasonality over the South Indian Ocean is investigated extensively by utilizing the MODIS satellite data and atmospheric reanalysis data. In austral summer, the climatological LCF has a local maximum off the west coast of Australia, as in the other subtropical basins (e.g., Klein and Hartmann 1993). Over the midlatitude and subpolar oceans, the mean LCF is greater and distributed more zonally across the basin. Across the subtropical basin, by contrast, atmospheric circulation is changed notably in association with the westward shift of the Mascarene high in winter, and correspondingly climatological LCF is distributed more zonally than in summer.

In either season, the spatial pattern of the climatological-mean LCF is overall explained by the EIS distribution. In summer, the SST distribution is characterized by a local subtropical minimum off the west coast of Australia and by pronounced meridional gradient across the midlatitude oceanic front anchored between the warm Agulhas Return Current and cool Antarctic Circumpolar Current. Owing to lower SST and warmer free-tropospheric temperature associated with enhanced subsidence, EIS has a local maximum off the west coast of Australia and increases with latitude in summer. In winter, EIS is horizontally uniform in the subtropics, which is also consistent with the zonal uniformity of LCF.

However, LCF distribution around the SST front is not fully explained by EIS. EIS strongly increases with latitude across the front whereas the corresponding increase in LCF is much less. We have found that enhanced SHF acts to increase LCF on the equatorward flank of the Agulhas SST front (Nonaka et al. 2009; Hotta and Nakamura 2011). This enhanced SHF is owed to the enhanced storm-track activity in the presence of the SST front. Transient atmospheric eddies not only act to relax the SAT gradient but also increase instantaneous surface wind speed, leading to extremely large upward SHF over the warmer side of the SST front. This rectifying effect of storm-track activity on climatological SHF seems prominent around the Agulhas SST front. Note that sub-monthly atmospheric eddies may also be important for climatological-mean low-cloud top, since climatological cross-frontal contrast of low-cloud top around the SST front along the Gulf Stream resembles the corresponding contrast under cold advection events (Liu et al. 2014).

Previous studies (e.g., Trenberth and Fasullo 2010; Grise et al. 2015) pointed out that many of the global climate models have large bias in shortwave radiation over the Southern Ocean, which can possibly affect the atmospheric circulation via SST distribution (Frierson and Hwang 2012; Hwang and Frierson 2013; Ceppi and Hartmann 2015). Although underestimation of super-cooled liquid water in mixed-phase clouds in the models is considered as the major cause of this bias (e.g., Senior and Mitchell 1993; Tsushima et al. 2006; Komurcu et al. 2014; McCoy et al. 2015b, 2016; Tan et al. 2016; Ceppi et al. 2016a; Bodas-Salcedo et al. 2016), our analysis suggests that bias in SST front and storm-track activity simulated in those models may also leads to the bias in LCF and thereby in the surface radiation budget. In fact, Masunaga et al. (2015) showed the importance of high-resolution SST in realistic representation of cloudiness around the North Pacific SST fronts in ERA-Interim. The LCF increase locally over the warmer side of an oceanic front through SHF is also recognized in the South Atlantic.

The seasonal cycle of subtropical LCF is not fully explained by EIS, either. EIS maximizes in spring, whereas LCF has more prolonged maximum from early winter. We have found that this wintertime augmentation of LCF is due to not only EIS but also enhanced SHF and seasonal lowering of SST. Centered at the western portion of the basin in winter, the Mascarene high enhances near-surface cold advection almost entirely across the subtropical basin, resulting in large upward SHF. In addition, seasonally enhanced storm-track activity augments SHF by not only bringing cold advection equatorward of the subtropical SST front but also augmenting scalar wind speed around 30°S where the mean cold advection by the Mascarene high is weaker than around 15°S-25°S. Thus, both the westward shift of the subtropical high and the seasonally enhanced storm-track activity seem essential for the unique seasonality of LCF within the subtropical South Indian Ocean via SHF, which is also supported through our multiple linear regression analysis.

The corresponding analysis of LCF in the South Atlantic and the South Pacific not only highlights the uniqueness of the South Indian Ocean arising from the seasonality of the Mascarene high but also reveals common features associated with sub-monthly atmospheric fluctuations among the three ocean basins. Compared to the South Indian Ocean, the seasonality of the subtropical highs is much weaker in the South Atlantic and Pacific. They reside over the eastern portions of the basins in both summer and winter. Correspondingly, LCF maximizes off the west coast of South Africa and South America in both seasons in accordance with the EIS distributions. We have revealed, however, that there are similarities among the three ocean basins around 30°S, where LCF exhibits a zonally-extended maximum from winter to spring while EIS peaks in spring. Unlike in the South Indian Ocean, there is no basin-wide enhancement of cold advection by climatological-mean southerlies in the South Atlantic and Pacific. Still, under the wintertime enhancement of sub-monthly atmospheric eddy activity around the subtropical SST fronts, SHF is enhanced in winter around 30°S across those basins, which can contribute to the wintertime enhancement LCF across the subtropical basins in the South Atlantic and Pacific as in the South Indian Ocean. In the Northern Hemisphere, two major storm tracks also form along the prominent oceanic frontal zones along the Gulf Stream and Kuroshio-Oyashio Extensions (Nakamura et al. 2004; Kwon et al. 2010), and the storm-track activity is much stronger in boreal winter than in summer, though somewhat suppressed in midwinter over the Pacific (Nakamura 1992). Impact of storm-track activity on LCF through SHF over those oceanic frontal zones in comparison with the subtropical North Pacific and Atlantic will be pursued in our future study.

As reviewed by Kamae et al. (2016) and Klein at al. (2017), near-surface temperature advection is recognized as an important cloud controlling factor that represents how strongly large-scale atmospheric circulation enhances upward SHF in favor of the formation of low-level clouds. However, the temperature advection calculated from monthly-mean temperature and winds does not fully explain SHF due to the prominent contribution from temperature and wind fluctuations associated with sub-monthly atmospheric disturbances mainly along the storm tracks. In a warmed climate, a weak negative feedback from enhanced cold advection is suggested by recent studies (Qu et al. 2015; Myers and Norris 2016), where the near-surface air temperature advection is mimicked as "SST advection" ($-\mathbf{V} \cdot \nabla \mathrm{SST}$) by near-surface winds $\mathbf{V}$ that includes no contribution from sub-monthly atmospheric eddies. We suggest that SHF may be used in place of near-surface temperature advection to obtain more realistic observational constraints on the LCF response to the global warming. Unlike the SST advection, however, SHF is a locally determined boundary layer quantity that can likely be affected by low-level clouds themselves. Thus, incorporating SHF in place of temperature advection in a multiple-linear regression model may bring about a causality issue, which should be carefully handled.

As pointed out by previous studies, strong covariability in interannual variations between EIS and SST can be an issue for projecting LCF response to global warming (Myers and Norris 2015), since both EIS and SST are likely to increase under warmed climatic conditions (Qu et al. 2014, 2015; Myers and Norris 2016; McCoy et al. 2017). Off the Peruvian coast, the EIS-SST anti-correlation is indeed strong in the course of seasonal cycle (Fig. 2.24; Wang et al. 2011). However, the anti-correlation is rather weak in the eastern portion of the subtropical South Indian Ocean as shown through our analysis (Fig. 2.10) and off the California coast (Wang et al. 2011). Furthermore, time lag between EIS and SST in the course of their seasonal cycle is apparent commonly over the subtropical and mid-basin domains in each of the South Indian Ocean (Fig. 2.10), in addition to the South Atlantic and Pacific (Fig. 2.26). We therefore argue that disentanglement of the dependence of LCF on EIS, SST and SHF may be possible over the subtropical basins, including the South Indian Ocean. Thus, seasonal variations might be better suited than interannual variations for constructing a multiple linear regression model to constrain the low-cloud response to the global warming.

As revealed through our analysis, the seasonality of the Mascarene high strongly affects low-level clouds over the subtropical South Indian Ocean. In fact, enhanced longwave cooling associated with those low-level clouds acts to strengthen land-sea contrasts of diabatic heating (Wu and Liu 2003), contributing to the maintenance of summertime subtropical highs (Miyasaka and Nakamura 2005, 2010). Nevertheless, the role of low-level clouds in the maintenance of the Mascarene high has not been fully investigated, which is pursued in Chapter 4.

Though beyond the scope of our study, satellite-based analysis of the variability in optical thickness of low-level clouds, in addition to their fraction (LCF), is necessary for deepening our understanding of albedo of low-level clouds and its variability (Wood 2012), but such analysis based on satellite data has not been performed until recently over the midlatitude and subpolar oceans (e.g., Terai et al. 2016; Ceppi et al. 2016b). Furthermore, although our focus is on how meteorological and oceanic conditions affect LCF, cloud microphysical processes and aerosol properties may also play a key role in determining LCF, and oceanic aerosol productivity can also play an important role in determining cloud condensation nuclei (e.g., Lana et al. 2011; McCoy et al. 2015a). These aspects should also be explored in future studies.

Chapter 3

Seasonality in the maintenance mechanisms for the subtropical high in the South Indian Ocean

Unpublished materials

3.1 Introduction

3.2 Data and model experiments

a Observational data

b Dynamical model

c AGCM output

3.3 The summertime subtropical high

a Observations

i Three-dimensional structure

ii Local diabatic heating

iii Storm-track activity

b LBM experiments

i Local influences

ii Remote influences from the tropics

3.4 The wintertime subtropical high

a Observations

i Three-dimensional structure

ii Local diabatic heating

iii Storm-track activity

b LBM experiments

i Local influences

ii Remote influences from the tropics

c AGCM experiments

3.5 Conclusions

Chapter 4

Radiative impacts of low-level clouds on the subtropical high in the South Indian Ocean and their seasonal differences simulated in a coupled general circulation model

Unpublished materials

4.1 Introduction

4.2 Model experiments

4.3 Results

a Seasonality in SST anomaly induced by low-level clouds

b Impacts of low-level clouds on the summertime subtropical high

c Impacts of low-level clouds on the wintertime subtropical high

4.4 Discussion

a Feedback loop for low-level clouds

b Changes in the large-scale ocean circulation

c Impacts of model biases

4.5 Conclusions

Chapter 5

General conclusions and discussions

5.1 Air-sea coupled system associated with low-level clouds in the South Indian Ocean

In this study, seasonal variations of low-level clouds and associated air-sea interactions over the South Indian Ocean have been investigated in detail and also comprehensively. Here, we recapitulate the main findings presented in the preceding chapters (Chapters 2-4) for summer and winter separately. Schematic diagrams for those seasons are shown in Figs. 5.1 and 5.2.

a Summer

Previous studies showed the subtropical Mascarene high resides over the eastern portion of the basin in summer and low-level clouds prevail east of the high under the enhanced lower-tropospheric static stability (e.g., Klein and Hartmann 1993; Miyasaka and Nakamura 2010). In fact, we have confirmed in Chapter 2 that the large LCF over the eastern portion of the basin under the enhanced lower-tropospheric stability is owing to the formation of the subtropical high, using the satellite observations and atmospheric reanalysis data.

Our main finding for the summertime climate is the importance of low-level clouds for the maintenance of the subtropical high, which has been revealed in Chapter 4. Our sensitivity experiments with a coupled general circulation model (CM2.1) confirmed that low-level clouds reinforce the summertime subtropical high ($\sim +5$ hPa) so that the high as the planetary wave component would almost vanish without the radiative effects of the subtropical low-level clouds. During the warm season, the albedo effect of low-level clouds strongly lowers SST under the strong summertime insolation, especially in the eastern portion of the basin (~ -4 °C in the CM2.1 experiments). The lowered SST hinders the southward displacement (or expansion) of the ITCZ, reducing precipitation from deep clouds in the equatorward portion of the subtropical South Indian Ocean. The anomalous diabatic cooling associated with the reduced precipitation induces an anticyclonic response to its southwest, reinforcing the surface subtropical high. Our dynamical model experiments have elucidated that the reinforcement through the anomalous condensation heating is predominant in the feedback from low-level clouds. The high is also modestly reinforced by the augmented in-atmosphere radiative cooling, which is attributable to the reduced longwave radiative heating by high-level clouds associated with the reduced deep convection as well as the cloud-top longwave cooling from low-level clouds. The modest impact of cloud-top longwave radiative cooling for the maintenance of the surface subtropical high is inconsistent with Miyasaka and Nakamura (2010)'s argument advocating its predominant impact. However, the dynamical model experiments in Chapter 3 with individual diabatic heating component taken from an atmospheric reanalysis data (JRA-55) have confirmed the predominance of the reduced precipitation for the maintenance of the high as the planetary wave component. Still, the shallow cooling-heating couplet between the cool South Indian Ocean and the heated Australian continent acts to suppress deep convection by invoking surface divergence and alongshore winds, which act to lower SST by enhanced evaporation, upper-ocean mixing, coastal upwelling and weakening of the Leeuwin Current (Seager et al. 2003; Miyasaka and Nakamura 2005, 2010; Kataoka et al. 2014), off the west coast of Australia. The analysis in Chapter 3 has also revealed that forcing from sub-monthly eddies as well as remote influences from the tropics is negligible for the maintenance of the summertime subtropical high over the South Indian Ocean.

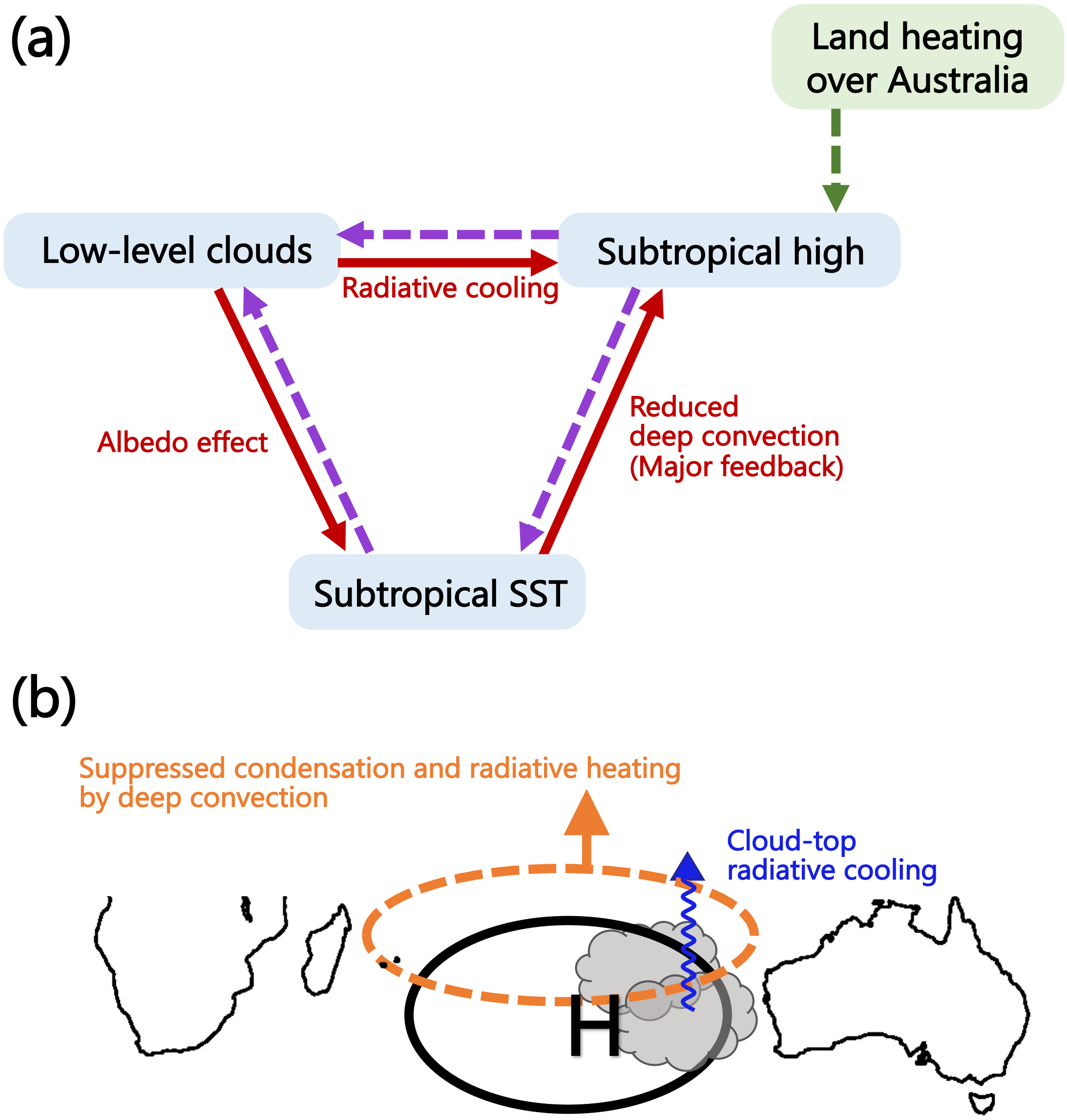

Figure 5.1: (a) Schematic diagram showing a feedback system associated with subtropical low-level clouds over the South Indian Ocean in austral summer. Solid line arrows indicate an influence demonstrated by the present study while dashed line arrows indicate that demonstrated by previous studies. Light blue boxes signify the components of the feedback associated with low-level clouds while the light green box signifies the components that can modulate the feedback. (b) Geographical location of each factor in (a). “H” signifies the subtropical high whereas grey objects signify low-level clouds.

b Winter

In winter, the subtropical Mascarene high resides over the *western* portion of the basin in the absence of the thermal contrast between the southeastern Indian Ocean and the Australian continent, and low-level clouds prevail across the entire subtropical basin. While those features are distinct from the other basins, the present study is the first to examine the maintenance mechanisms for the wintertime high and extensive low-level clouds in the South Indian Ocean.

In winter, the westward-shifted subtropical high contributes to the wintertime enhancement and westward expansion of low-cloud cover by invoking the mid-tropospheric subsidence, which enhances lower-tropospheric stability, and the southeasterly Trades, which enhance upward SHF, both across the entire subtropical basin (shown in Chapter 2). Our sensitivity experiments with CM2.1 shown in Chapter 4 have elucidated that those low-level clouds feed back onto the equatorward portion of the subtropical high ($\sim +1.5$ hPa) through augmenting cloud-top longwave cooling. They also reinforces the high modestly through the reduced turbulent heating associated with the lowered SST. In contrast to the summertime case, suppression of deep convection by low-level clouds is weak, leading to a smaller contribution to the maintenance of the high. This is probably because the reduced lowering of SST ($\sim -2\,^{\circ}$C) due to the weaker cloud radiative forcing under reduced wintertime insolation along with climatologically low SST and the enhanced winter-hemisphere Hadley cell, suppressing precipitation even in the absence of low-level clouds. Nevertheless, it has been demonstrated that there exists a coupling between the subtropical high and low-level clouds also in winter.

This study has also revealed the modulations of the aforementioned coupling by the seasonally enhanced storm-track activity maintained by the Agulhas SST front. In Chapter 2, we have shown that the enhanced storm-track activity maintained by the Agulhas SST front is also important for the enhanced LCF, because migratory synoptic-scale eddies along the storm track augment upward SHF by enhancing cold advection over the warmer side of the wintertime subtropical SST front located at ∼30°S and increasing the climatological-mean scalar wind speed where climatological-mean southerlies are weak (25°S-30°S). This is presumably one of the reasons why SHF emerges as an important cloud-controlling factor for the seasonal cycle of LCF in the subtropical South Indian Ocean. The storm-track activity is even more important for the maintenance of the poleward portion of the subtropical high through the convergences of eddy heat and vorticity fluxes and the resultant acceleration of the climatological-mean westerlies on the poleward side of the high, as shown by the dynamical model experiments in Chapter 3. The AGCM experiments in Chapter 3 further indicate that the Agulhas SST front acts to reinforce the high by energizing the storm-track activity.

The dynamical model experiments in Chapter 3 have also revealed that unlike in austral summer, the coupled system can be modulated by the remote influence from the tropics, especially the Asian summer monsoon region. The enhanced deep convection over the Asian summer monsoon region as well as the equatorial eastern Indian Ocean and western Pacific acts not only to shift the Mascarene high westward but also to enhance mid-tropospheric subsidence and equatorward surface winds over the central and western portions of the subtropical South Indian Ocean. The induced subsidence acts to stabilize and dry the free troposphere, and the equatorward surface winds yield near-surface cold advection, both of which are favorable for the low-level cloud formation but unfavorable for the development of deep precipitating clouds. The resultant enhanced radiative cooling and reduced deep condensation heating can further reinforce the surface subtropical high.

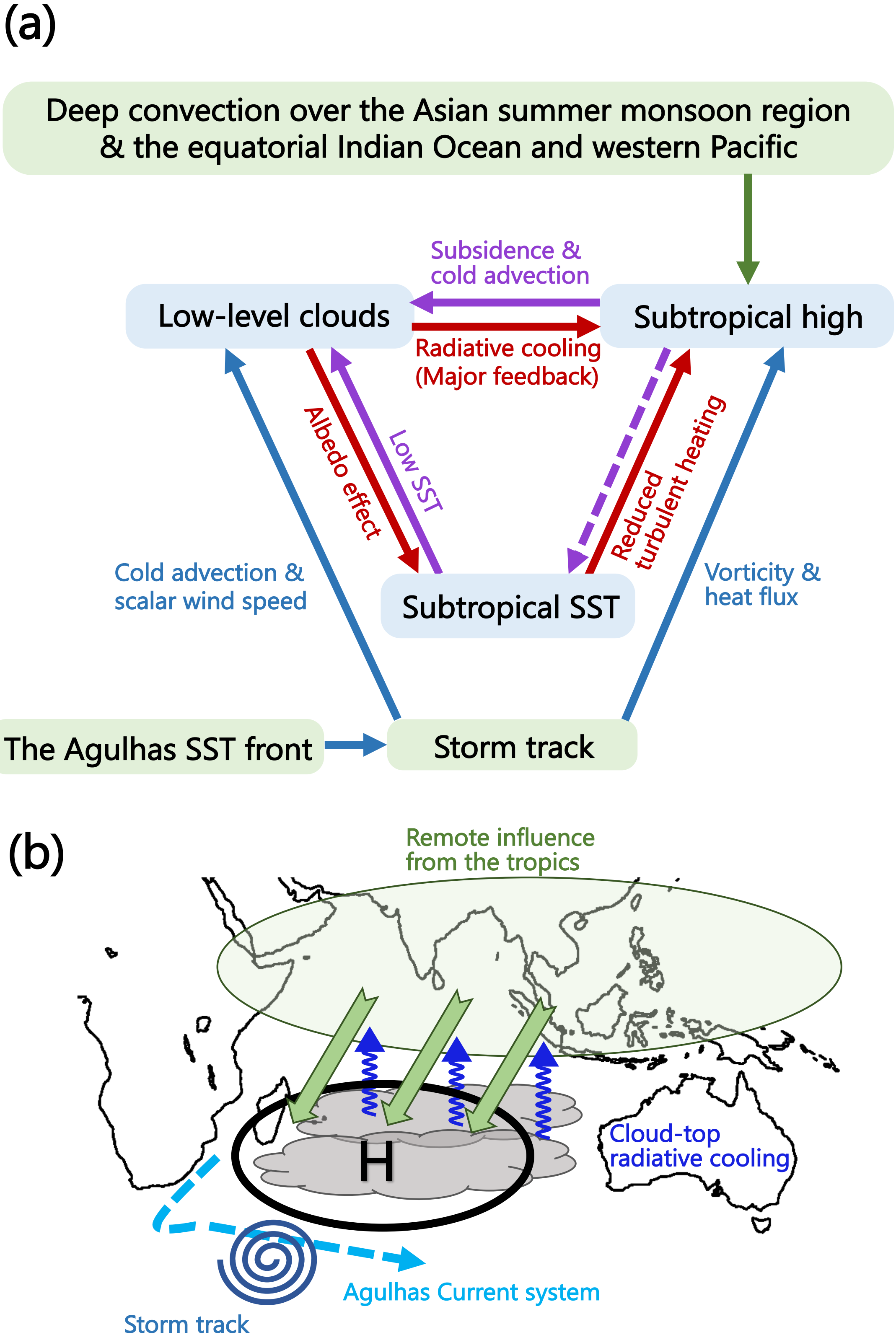

Figure 5.2: Same as in Fig. 5.1, but for austral winter. Green arrows in (b) indicate upper-tropospheric divergent wind from the tropics.

5.2 Implications and prospects for the future

As mentioned in Section 5.1, we have found that the modulations of the coupling system between the subtropical Mascarene high and low-level clouds by the Asian summer monsoon and the storm-track activity maintained by the Agulhas SST front leads to the westward shift and strengthening of the wintertime subtropical high in winter, which are the distinct features of the South Indian Ocean from the other ocean basins (Figs. 1.1, 1.3a,d). The wintertime enhancement of storm-track activities is also observed in the North Pacific and Atlantic, namely the Kuroshio-Oyashio Extension and Gulf Stream regions (e.g., Nakamura et al. 2004, 2010; Kwon et al. 2010). In these storm-track regions, eddy activity in winter is stronger than in summer, except for the midwinter suppression over the North Pacific (Nakamura 1992). One may wonder if the enhancement of the storm-track activities in boreal winter might contribute to the wintertime westward shift and strengthening of the subtropical highs along with enhanced LCF. In the wintertime Northern Hemisphere, however, strong orographic effects and thermal forcings with pronounced land-sea thermal contrasts in the mid- and subpolar latitudes force planetary waves with a basin-scale surface cyclone in the western and central portions of each basin (e.g., Nakamura et al. 2010; Fig. 1.1a). Although the feedback forcing from sub-weekly eddies acts to reinforce the high in the North Atlantic (Nakamura et al. 2010) as in the South Indian Ocean, the wintertime subtropical highs in the Northern Hemisphere form as a component of the prominent planetary waves with no climatological wave-activity injection from the tropics (Nakamura et al. 2010), resulting in the lack of westward shift of those highs (Fig. 1.1a).

In the Southern Hemisphere, the wintertime subtropical highs in the South Atlantic and Pacific also reside over the eastern portion of the two basins, and LCF is maximized in their eastern sides (Fig. 1.3c; see Section 2.4e for the details), despite the slight increase in LCF and storm-track activity is observed (see Section 2.4e for the details). Previous studies (Rodwell and Hoskins 2001; Xu et al. 2004; Richter and Mechoso 2004, 2006) showed that South American and African orography contributes to the enhanced low-cloud cover as well as the equatorward surface alongshore winds over the eastern portion of each basin, acting to cool the ocean and thereby to enhance the land-sea thermal contrast. Thus the orographic forcing can drive the local atmosphere-ocean-land feedback system suggested for the summertime subtropical highs (Fig. 1.2; Miyasaka and Nakamura 2005, 2010) even in winter. However, such an orographic forcing is unlikely around the Australian continent because the orography is much less steep and the continent exits only poleward of 15°S. Since the strong tropical diabatic heating is concentrated into the Asian summer monsoon region as well as the equatorial Indian Ocean and western Pacific, the remote influence through the local Hadley cell is strong only in the subtropical South Indian Ocean in austral winter (Fig. 3.38), further enhancing the interbasin differences. In addition, the enhancement of the wintertime storm-track activity is more prominent in the eastern South Atlantic and the South Indian Ocean (Figs. 1.3b,e; Nakamura and Shimpo 2004). We therefore argue that the eddy feeback forcing may act to maintain the wintertime subtropical high in the *eastern* South Atlantic in the absence of tropical influence, but not over the South Pacific. Further investigation is required to understand why the wintertime subtropical highs in the South Pacific and Atlantic reside over the eastern portion of the basins.

By contrast, the geographical relationship between the subtropical Mascarene high and low-level clouds in summer is similar to the other basins (e.g., Klein and Hartmann 1993; Miyasaka and Nakamura 2005, 2010; see also Section 2.4e). We have shown in Chapter 4 that the artificial removal of cloud radiative effect in a CGCM is a useful method for assessing the impacts of low-level clouds on the subtropical high and it is particularly so if combined with the atmospheric dynamical model experiments as conducted in Chapter 3. With a care for a model climatic drift, we can apply this methodology to the other subtropical basins so that we can identify common features as well as interbasin differences. Although their focus was mostly on the off-equatorial ITCZ, Xie et al. (2007) removed cloud radiative effect over the South Pacific in a regional coupled model to show that low-level clouds act to hinder the potential seasonal drift of the ITCZ into the Southern Hemisphere in austral summer and autumn through maintaining the cross-equatorial SST difference and thereby suppressing convective precipitation in the tropical Southern Hemisphere. Although the equatorial-asymmetric mode does not seem to be operative in the South Indian Ocean and thus the mechanisms may be somewhat different, the suppression of convective precipitation by low-level clouds and the associated strengthening of the subtropical high is likely to occur in the South Pacific. In addition, since low-level clouds prevail along the coasts in the other basins (e.g., Klein and Hartmann 1993), interaction with the cool eastern boundary currents and associated coastal upwelling may be more important than in the South Indian Ocean, although the weakening of the warm Leeuwin Current off western Australia due to low-level clouds is in fact found in our model experiments. Since warm biases of coastal SST in the South Atlantic and Pacific is one of the serious problems in climate models (e.g., Zuidema et al. 2016), understanding impacts of coastal low-level clouds along the coast is necessary. For that purpose, however, a high-resolution CGCM is required that well represents those coastal current systems and low-level clouds.

The active roles of low-level clouds elucidated in this study are also important for understanding climate variability. In the South Indian Ocean, the Ningaloo Niño/Niña (e.g., Kataoka et al. 2014) and the subtropical dipole mode (e.g., Behera and Yamagata 2001) are known as major climate modes in austral summer. During the Ningaloo Niño/Niña, LCF changes are in fact observed (Tozuka and Oettli 2018), which can amplify the SST anomalies and the anomalous subtropical high to the west. Although changes in LCF associated with the subtropical dipole mode have not been investigated so far, similar feedback may be possible in each of its centers of action. Therefore, our results suggest that low-level clouds may act to amplify the Ningaloo Niño/Niña and the subtropical dipole mode. Because the climatological-mean SST along the Leeuwin Current is slightly below the threshold for active cumulus convection, negative SST anomalies are unlikely to strongly affect precipitation, while the positive SST anomalies may exceed the threshold, leading to stronger precipitation anomaly and thus anomalous subtropical high. In fact, the asymmetry of anomalous high-level clouds tied to deep convection is actually observed in the Ningaloo Niño/Niña (Tozuka and Oettli 2018), to which low-level clouds may contribute through magnifying the SST and SLP anomalies. The induced deep convection in the Ningaloo Niño may further weakens the subtropical high, which acts to introduce the asymmetry with the stronger Ningaloo Niño, although the associated reduction of downward shortwave radiation at the surface itself acts as a negative feedback to the Ningaloo Niño (Tozuka and Oettli 2018). It is also interesting to extend the analysis to the analogous climate modes in the other basins such as the subtropical dipole modes in the South Atlantic and Pacific (e.g., Morioka et al. 2011, 2013), and coastal Niño phenomena, namely the Beguela Niño (e.g., Shannon et al. 1986), California Niño (e.g., Yuan and Yamagata 2014), and Dakar Niño (e.g., Oettli et al. 2016), as well as the air-sea coupled climate modes exhibiting positive low-cloud-SST feedback including the Pacific Decadal Oscillation, the Atlantic Multidecadal Oscillation and others (e.g., Tanimoto and Xie 2002; Huang and Hu 2007; Clement et al. 2009; Yuan et al. 2016; Myers et al. 2018).

Future changes in low-level clouds have large uncertainties, hampering reliable projections of future global warming (e.g., Bony and Dufresne 2005; Qu et al. 2014, 2015; Myers and Norris 2016). Our results suggest that uncertainties in future projection of low-level clouds can affect future changes in the subtropical highs. Li et al. (2012, 2013) argued that the intensity of subtropical highs will increase in summer as a result of enhanced land-sea thermal contrast. However, LCF may decrease under the higher SST in the future (e.g., Qu et al. 2014, 2015; Myers and Norris 2016), which acts to accelerate future ocean warming and thereby weaken the subtropical highs. Thus, impacts of future changes in low-level clouds and their uncertainties on subtropical highs should be investigated more thoroughly.

It is also informative to apply our methodology in this study to the midlatitude and subpolar oceans, where low-level clouds are prevalent (e.g., Klein and Hartmann 1993; Wood and Bretherton 2004; Koshiro and Shiotani 2014; Chapter 2 of this study). The clouds may interact with eddy-driven jets and storm-track activity as well as remotely with the ITCZs (e.g., Frierson and Hwang 2012; Hwang and Frierson 2013; Ceppi and

Hartmann 2015; Li et al. 2015; Watt-Meyer and Frierson 2017; Grise et al. 2019). Furthermore, local LCF maxima (minima) along the warmer (cooler) flanks of the oceanic fronts are embedded with the large LCF across the basins as shown in Chapter 2. Those low-level clouds therefore act to relax the frontal SST gradient. Meanwhile, enhanced thickening of the ocean mixed layer on the warmer sides of the fronts induced by low-level clouds may amplify (damp) the frontolysis by the climatological-mean surface heat flux in summer (winter), leading to the complicated seasonality of the cloud impacts (e.g., Tozuka and Cronin 2014; Ohishi et al. 2016). Considering the anchoring effect of the SST fronts on storm-track activity (e.g., Nakamura et al. 2004, 2008; see also Chapter 3), high-resolution modelling is needed to extract the comprehensive impacts of low-level clouds including their frontal-scale structure, on large-scale atmospheric and oceanic conditions (c.f., Masunaga et al. 2020). It should be noted that large-scale controls of cloud water path are also necessary to understand, since they may be different from those of LCF (e.g., van der Dussen 2015). Around the SST fronts, cross-frontal differences in aerosol activation through shallow convection may also affect the cloud optical depth and thus the albedo effect of low-level clouds (Koike et al. 2012, 2016)

In Chapter 3, we have shown that the storm-track activity energized by the Agulhas SST front acts to maintain the wintertime subtropical Mascarene high and low-level clouds that form in the subtropics and around the Agulhas SST front. It suggests that improving the representation of the SST front in climate models (e.g., high-resolution modelling) contributes to the better representation of the subtropical high and low-level clouds, although problems in parameterization are typically dominant in causing model biases of low-level clouds. In fact, simulating the frontal-scale structure of LCF around the Agulhas SST front requires SST data capturing the front as the boundary conditions, as found in our AGCM experiments (see Section 2.4b). Masunaga et al. (2015) also showed the importance of high-resolution SST in realistic representation of cloudiness around the North Pacific SST fronts in ERA-Interim. Those cloud biases might in turn affect large-scale atmospheric and oceanic conditions. In addition, since input of wind stress curl associated with the subtropical high acts to accelerate the subtropical oceanic gyre, there may be possibility of the enhanced Agulhas SST front by the subtropical high. There is still a debate on the relationship between the surface winds and the Agulhas Current system, since nonlinear mesoscale dynamics plays a role on the determination of volume transport of the Agulhas leakage and the Agulhas Return Current, but some recent studies showed the strengthening of the Agulhas Return Current by the enhanced trade winds or midlatitude westerlies in the series of high-resolution ocean circulation model experiments (Durgadoo et al. 2013; Loveday et al. 2014). The enhanced Agulhas SST front acts to maintain storm-track activity and thus the subtropical high as well as low-level clouds, especially in winter. Thus there might be a further positive feedback loop via the feedback from the subtropical high to the Agulhas SST front in a fully coupled ocean-atmosphere system. Exploring the existence of such a positive feedback is attractive as our future work.

In Chapter 3, we have also found the existence of the remote influences from the tropics on the wintertime subtropical high, suggesting that the improved representation of tropical convective precipitation including the Asian summer monsoon is also important for the simulation of the wintertime subtropical high and low-level clouds. As indicated by Levitus (1987), monsoonal swirling of surface winds from the South Indian Ocean into the North Indian Ocean across the equator (Fig. 1.4) forces the southward ocean Ekman heat transport, acting to reduce the cross-equatorial SST gradient. This may weaken the amplitude of the seasonal cycle of the monsoon, constituting a negative feedback (Webster 2006). It is well known that the swirling winds across the equator are attributable to the diabatic heating associated with the Asian summer monsoon (e.g., Rodwell and Hoskins 1995, 1996), but the reinforcement of the wintertime subtropical Mascarene high by the Asian summer monsoon suggested by this study may further enhance this negative feedback through the associated southeasterly Trades. Thus our results can contribute to the deeper understanding of the ocean-land-atmosphere coupled system associated with the Asian summer monsoon and its variability.

Finally, our discussions on the subtropical high focus mainly on its maintenance. In reality, the subtropical Mascarene high undergoes such a significant seasonal transition that it reaches its maximum in the western portion of the basin in winter after the autumn minimum and then shifts eastward, constituting its summertime form (Figs. 3.11a-d). Thus investigating seasonal march of the subtropical high and the associated factors relevant to its maintenance, including low-level clouds, the Asian summer monsoon, the storm-track activity, underlying SST, and land heating over Australia, will lead to deeper and more comprehensive understanding of its formation and seasonal transition, which will be done in our future work.

Acknowledgments

I'd like to express my sincerest thanks to the supervisor Prof. H. Nakamura for his guidance and encouragement throughout the course of this study. I am also grateful for the referees of this dissertation (Dr. M. Koike, Prof. Y. Takayabu, Dr, T. Tozuka, and Dr. K. Suzuki), whose comments and suggestions have led to substantial improvement. I'd like to extend my thanks to the current or former faculty members (Dr. T. Miyasaka, Dr. K. Nishii, Dr. Y. Kosaka, Prof. B. Taguchi, and Dr. M. Mori) as well as visitors from the outside for their valuable comments and continuous supports. Chatting and discussing with my colleagues were indispensable for getting over the difficulties in my academic life, which I appreciate. Finally, I express my deepest gratitude to my family for their support and encouragement.

Appendix A

Estimation of degrees of freedom

To obtain confidence intervals, degrees of freedom for a given variable are needed. In this study, effective degrees of freedom N_e are estimated as

$$N_e = \frac{N}{T_e X_e Y_e}, \tag{A1}$$

where N denotes the total sample size, and T_e, X_e and Y_e temporal, zonal and meridional decorrelation scales, respectively. In Eq. (A1), T_e is evaluated by

$$T_e = 1 + 2\sum_{t=1}^{N_d}(1 - \frac{t}{N_d})R(t), \tag{A2}$$

where $R(t)$ is autocorrelation with time lag t. X_e and Y_e can be evaluated similarly. In our evaluation, N_d is set to 16 days for T_e, while 48° is assigned for both X_e and Y_e. Nevertheless Y_e is set to the meridional width of the domain if it is less than the above value. Table A.1 shows the domain-averaged T_e, X_e and Y_e for each of the variables (SHF, SST$-$SAT and scalar surface wind speed) within the two sectors of the South Indian

Ocean.

Table A.1: List of T_e (days; left), X_e (°; middle) and Y_e (°; right) for SHF, SST−SAT and scalar surface wind speed (top to bottom) for the domains around the Agulhas SST front (AF) and the subtropical South Indian Ocean (ST).

	AF			ST		
SHF	2	8	5	3	13	3
SST−SAT	2	9	5	4	11	3
surface wind speed	3	13	4	2	19	3

Appendix B

Analysis of multiple linear regression model

To quantify the relative importance of cloud controlling factors in seasonal variations of LCF, daily dependence of LCF on those factors is derived through multiple linear regression as used in recent studies of subtropical LCF (e.g., Qu et al. 2014, 2015; Seethala et al. 2015; Myers and Norris 2016; McCoy et al. 2017). In this study, a regression model is constructed from daily anomalies over the subtropical South Indian Ocean [55.5°E-114.5°E, 20.5°S-34.5°S], as local daily departures from the seasonal climatologies (for each of DJF, MAM, JJA and SON). As predictors for the daily LCF variations, EIS, SST, SHF, 700-hPa ω and RH are chosen, and their regression slopes against the LCF variations are then derived through inverting the covariance matrix. Our regression model is unlikely to suffer substantially from the covariability among the predictors, because the tolerance[2] of each variable is larger than 0.69, much larger than

---

[2] Tolerance : A commonly used measure of collinearity and multicollinearity. The tolerance of variable i (TOL$_i$) is $1 - R_i^2$, where R_i^2 is the coefficient of determination for the prediction of variable i by the other independent variables in the regression variate. As the tolerance value grows smaller, the variable is more highly predicted by the other independent variables (collinearity). Quoted from Hair et al. (2010).

0.2 below which multicollinearity is likely to occur (Hair et al. 2010).

As noted by McCoy et al. (2017), a multiple linear regression model cannot perfectly extract the impacts of individual large-scale forcing, since 1) it takes some time period for clouds to respond to the forcing, and 2) the clouds and boundary layer properties are advected spatially by large-scale ambient airflow. Nevertheless, the derived local dependence is useful for quantifying their local control on LCF.

The regression slope thus derived for each variable is shown in Table B.1. We have calculated confidence intervals following the supporting information by Qu et al. (2015) and found that the 2.5-97.5% confidence interval for each slope is smaller than the slope itself by one or two orders of magnitude due to large sample size. The slope $\partial \mathrm{LCF}/\partial \mathrm{SHF}$ is positive in the subtropics, which is consistent with the notion that enhanced heat supply from the ocean destabilizes the surface layer to facilitate the shallow convection (e.g., Mauger and Norris 2010). The positive slope $\partial \mathrm{LCF}/\partial \mathrm{EIS}$ is also in agreement with previous studies (e.g., Wood and Bretherton 2006; Koshiro and Shiotani 2014), in which enhanced inversion strength is shown to result in higher LCF. The mean slope in the subtropics is comparable to those obtained by Qu et al. (2014), Seethala et al. (2015) and McCoy et al. (2017) based on different satellite data and/or different time scales of variability. The strongly negative $\partial \mathrm{LCF}/\partial \mathrm{SST}$ seems consistent with LES experiments under the fixed relative humidity (Rieck et al. 2012; Bretherton et al. 2013), in which a decreasing tendency for subtropical LCF with warming SST is simulated. The mean slope of -1.4 % K^{-1} is also comparable to those obtained by Qu et al. (2014) and Seethala et al. (2015). The negative slope $\partial \mathrm{LCF}/\partial \omega$ is also consistent with Myers and Norris (2013), who showed that weakening of subsidence under the fixed inversion strength leads to larger LCF over the subtropical oceans. Finally, $\partial\text{LCF}/\partial\text{RH}$ is positive, which is supported by the notion that entrainment of drier air acts to reduce cloudiness (Bretherton et al. 2013; van der Dussen et al. 2015). The mean slope of 0.38 % $\%^{-1}$ is comparable to the value obtained by McCoy et al. (2017).

Table B.1: Regression slope for each of the predictors.

$\partial\text{LCF}/\partial\text{SHF}$ (% (W $\text{m}^{-2})^{-1}$)	$\partial\text{LCF}/\partial\text{EIS}$ (% K^{-1})	$\partial\text{LCF}/\partial\text{SST}$ (% K^{-1})	$\partial\text{LCF}/\partial\omega$ (% (hPa $\text{day}^{-1})^{-1}$)	$\partial\text{LCF}/\partial\text{RH}$ (% $\%^{-1}$)
0.64	2.6	-1.4	-0.055	0.38

Appendix C

Supplementary figures for chapter 2

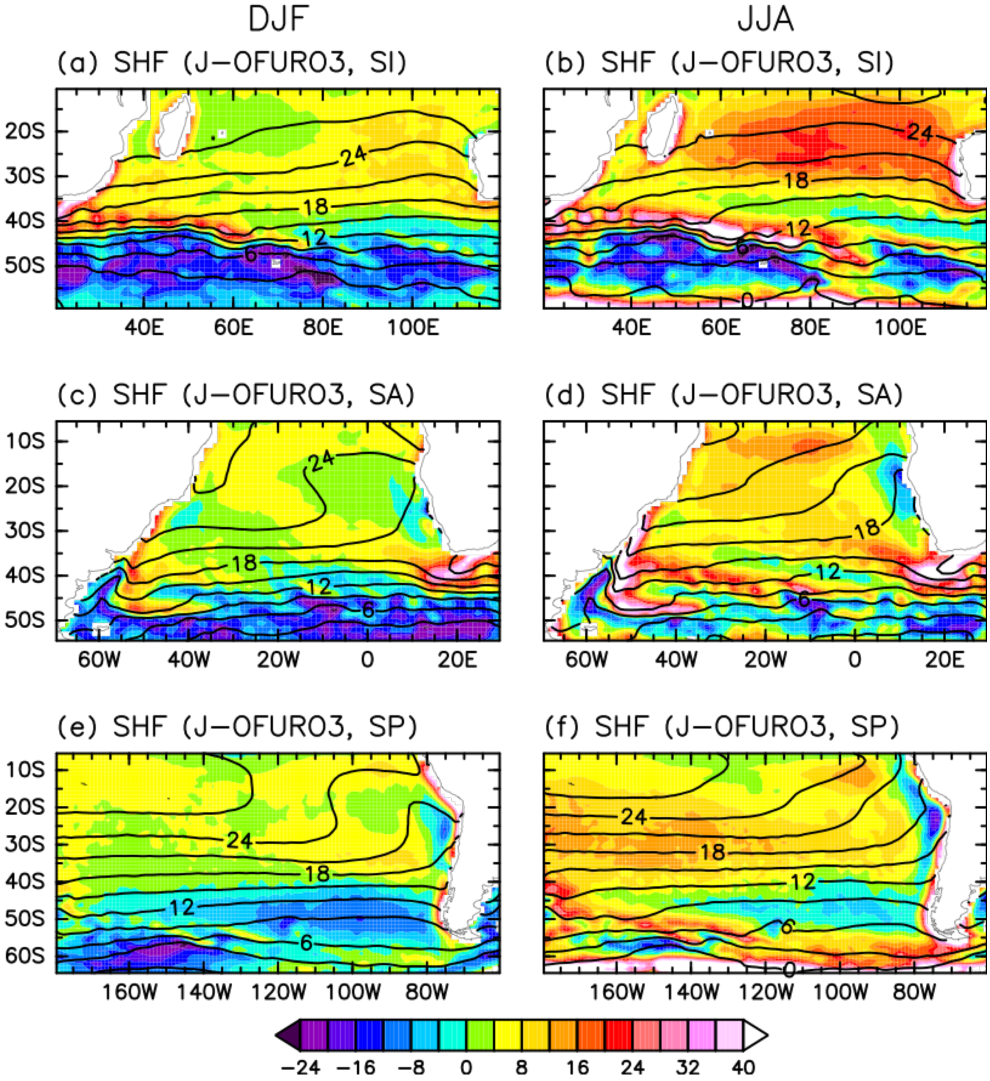

Figure C.1: Climatological distributions for austral summer (DJF) of maritime surface sensible heat flux (SHF; color shaded for every 4 W m^{-2}) over (a) the South Indian Ocean, (c) the South Atlantic, and (e) the South Pacific based on J-OFURO3. Superimposed with contours is SST (every 3 °C) in ERA-Interim. (b), (d) and (f) Same as in (a), (c) and (e), respectively, but for austral winter (JJA). (a)-(f) correspond to Figs. 2.5g, 2.5h, 2.23g, 2.23h, 2.24g and 2.24h, respectively.

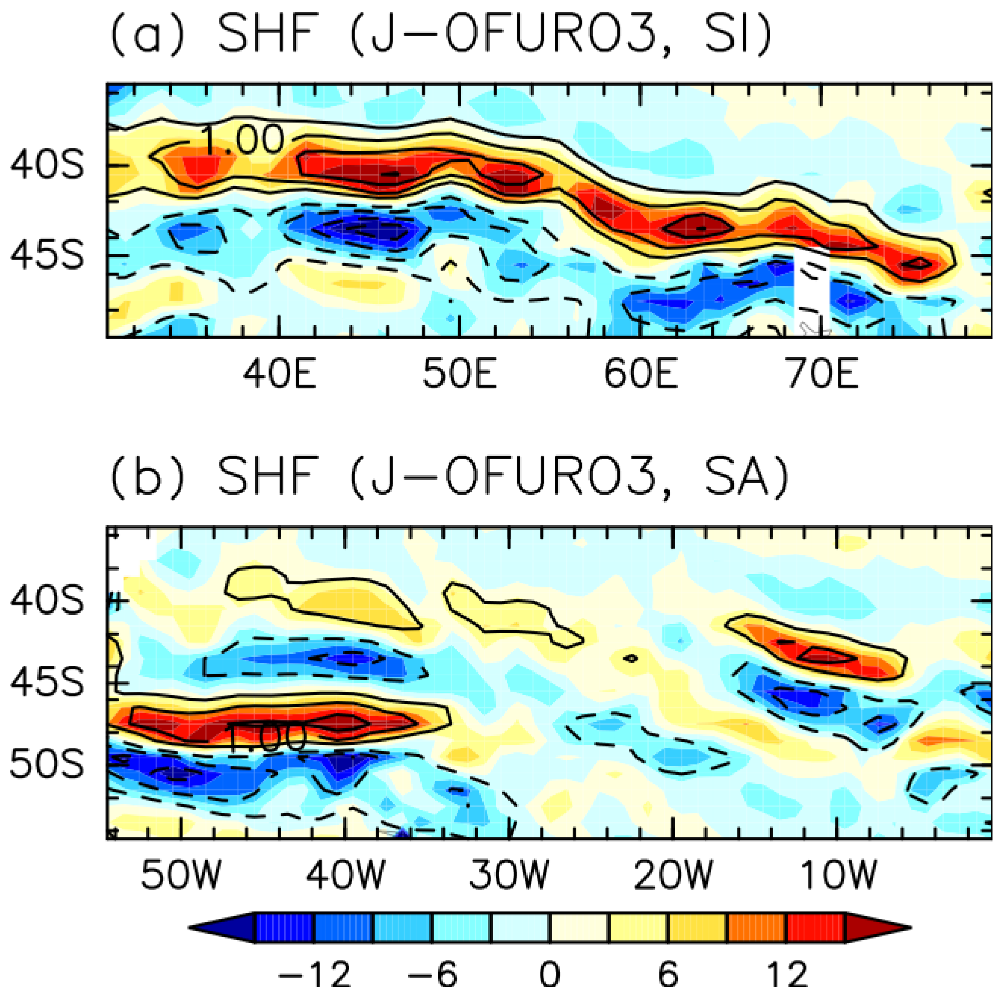

Figure C.2: Meridionally high-pass-filtered fields for austral summer (DJF) of SHF (color shaded for every 3 W m^{-2}) based on J-OFURO3 over (a) the South Indian Ocean and (b) the South Atlantic. Superimposed with the contours is meridionally high-pass-filtered SST in ERA-Interim (every 0.5 °C; solid and dashed lines for positive and negative values, respectively) for DJF. Local departures of each variable from its meridional nine-point running-mean values are regarded as the meridionally high-pass-filtered components. (a)-(b) correspond to Figs. 2.6d and 2.25c, respectively.

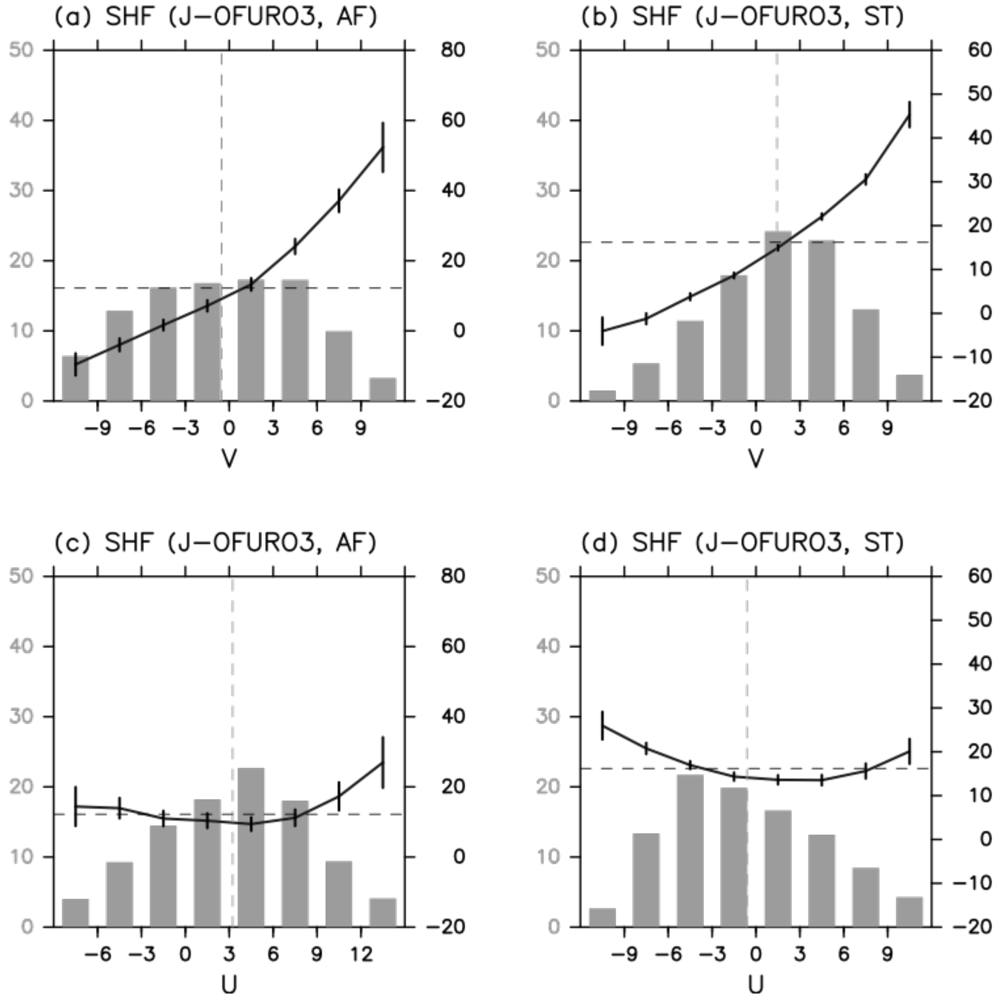

Figure C.3: (a) Dependence of daily SHF (W m^{-2}; right ordinate) in J-OFURO3 on surface meridional wind velocity in ERA-Interim in DJF. Grey bars are daily frequency (%; left ordinate) of surface meridional wind (m s^{-1}) at individual grid points within the domain on the equatorward flank of the Agulhas SST front [40.5°E-54.5°E, 37.5°S-41.5°S, AF]. Tick marks along the abscissa indicate bin boundaries. Leftmost and rightmost bars include all the samples of the strongest northerlies and southerlies, respectively. Black solid line indicates climatological-mean values of SHF (right ordinate) for individual bins with the 90% confidence intervals, while the climatological-mean SHF averaged over all the samples is represented by the black dashed horizontal line. The grey dashed vertical line indicates the climatological-mean meridional wind. (b) Same as in (a), but for the equatorward flank of the subtropical SST front [60.5°E-109.5°E, 27.5°S-29.5°S, ST] in JJA. (c)-(d) Same as in (a)-(b), respectively, but for the dependence of SHF on surface zonal wind velocity. (a)-(d) correspond to Figs. 2.8a, 2.11a, 2.8d and 2.11d, respectively.

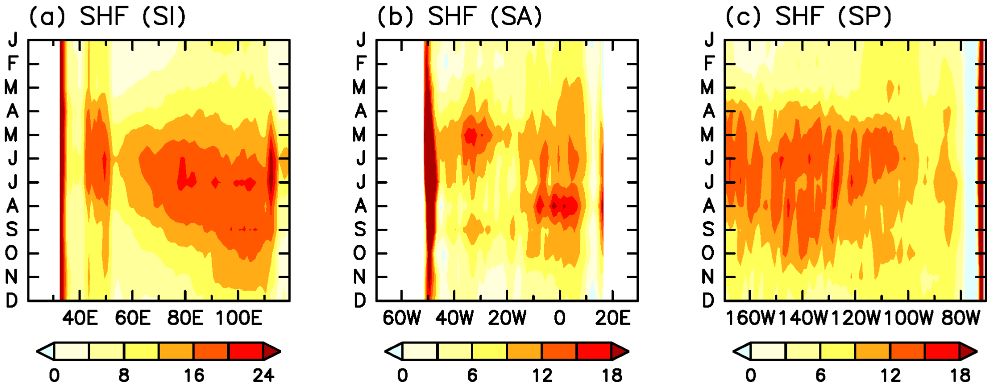

Figure C.4: Climatological-mean seasonal cycle of the longitudinal distribution of SHF (W m^{-2}; coloring convention is indicated at the bottom of each panel) in J-OFURO3 across the subtropical basin of (a) the South Indian Ocean averaged between 15.5°S and 29.5°S, the South Atlantic at 32.5°S and (d) the South Pacific at 28.5°S. (a)-(d) correspond to Figs. 2.10e, 2.26e and 2.26j, respectively.

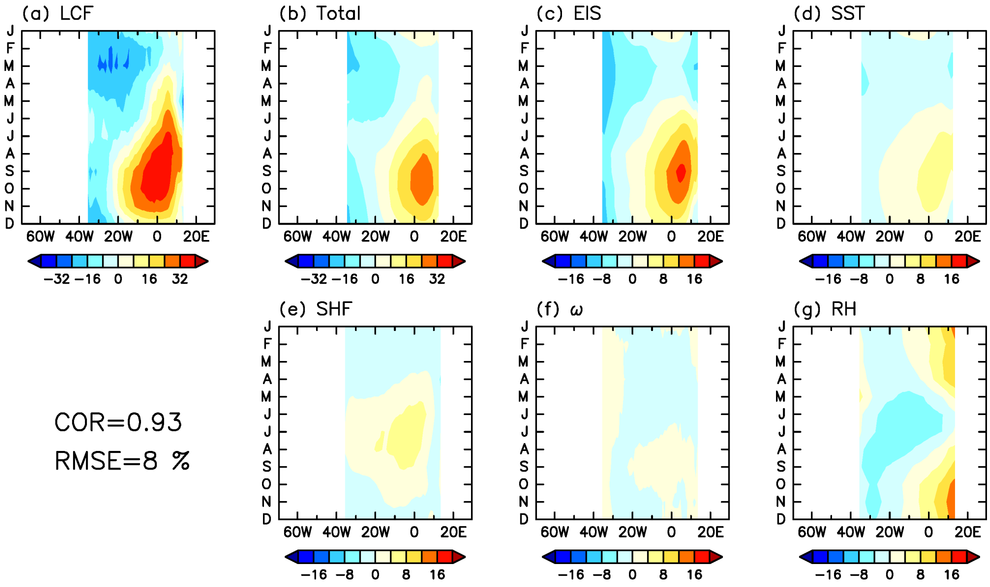

Figure C.5: (a) Climatological-mean seasonal cycle of the longitudinal distribution of low-cloud fraction (LCF, %) across the subtropical basin of the South Atlantic at 10.5°S. The annual-mean LCF within the domain has been removed. (b) Same as in (a), but for the corresponding LCF (%) predicted by the multiple linear regression model described in Appendix B. The correlation and root mean square error (RMSE) between (a) and (b) are shown below the panel (a). (c)-(g) Same as in (b) but for the contributions from EIS, SST, SHF, 700-hPa ω, and 700-hPa RH, respectively, to (b). For each of the panels coloring convention is indicated at the bottom.

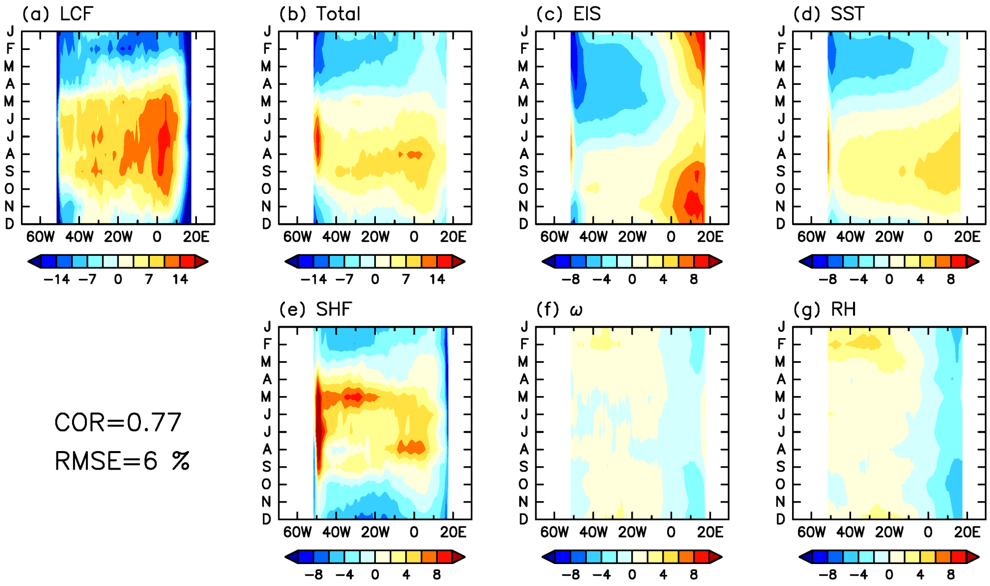

Figure C.6: Same as in Fig. C.5, but for the South Atlantic at 32.5°S.

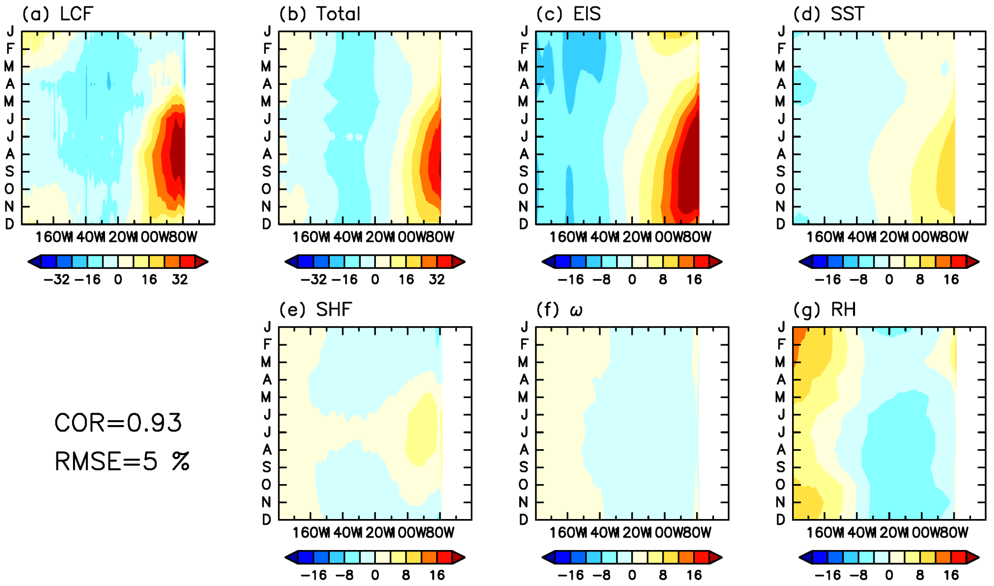

Figure C.7: Same as in Fig. C.5, but for the South Pacific at 10.5°S.

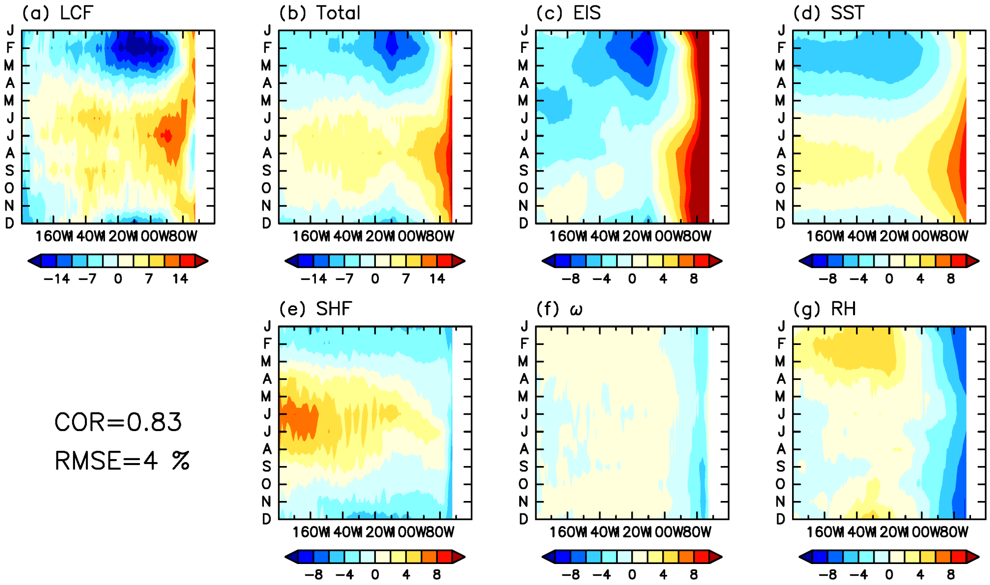

Figure C.8: Same as in Fig. C.5, but for the South Pacific at 28.5°S.

Appendix D

Supplementary figures for chapter 3

Unpublished materials

Appendix E

Mixed-layer heat budget analysis

Unpublished materials

Appendix F

Supplementary figures for chapter 4

Unpublished materials

Reference

Albern, N., A. Voigt, S. A. Buehler, and V. Grützun, 2018: Robust and nonrobust impacts of atmospheric cloud-radiative interactions on the tropical circulation and its response to surface warming. *Geophys. Res. Lett.*, **45**, 8577–8585, doi:10.1029/2018GL079599.

Balmaseda, M. A., K. Mogensen, and A. T. Weaver, 2013: Evaluation of the ECMWF ocean reanalysis system ORAS4. *Quart. J. Roy. Meteor. Soc.*, **139**, 1132–1161, doi:10.1002/qj.2063.

Beal, L. M., W. P. M. de Ruijter, A. Biastoch, R. Zahn, and SCOR/WCRP/IAPSO Working Group 136, 2011: On the role of the Agulhas system in ocean circulation and climate. *Nature*, **472**, 429–436, doi:10.1038/nature09983.

Behera, S. K., and T. Yamagata, 2001: Subtropical SST dipole events in the southern Indian Ocean. *Geophys. Res. Lett.*, **28**, 327–330, doi:10.1029/2000GL011451.

Bellomo, K., A. Clement, T. Mauritsen, G. Rädel, and B. Stevens, 2014: Simulating the role of subtropical stratocumulus clouds in driving Pacific climate variability. *J. Climate*, **27**, 5119–5131, doi:10.1175/JCLI-D-13-00548.1.

Bellomo, K., A. Clement, T. Mauritsen, G. Rädel, and B. Stevens, 2015: The influence of cloud feedbacks on equatorial Atlantic variability. *J. Climate*, **28**, 2725–2744, doi:10.1175/JCLI-D-14-00495.1.

Bennartz, R., 2007: Global assessment of marine boundary layer cloud droplet number concentration from satellite. *J. Geophys. Res.*, **112**, D02201, doi:10.1029/2006JD007547.

Bodas-Salcedo, A., P. G. Hill, K. Furtado, K. D. Williams, P. R. Field, J. C. Manners, P. Hyder, and S. Kado, 2016: Large contribution of supercooled liquid clouds to the solar radiation budget of the Southern Ocean. *J. Climate*, **29**, 4213–4228, doi:10.1175/jcli-d-15-0564.1.

Bony, S., and J.-L. Dufresne, 2005: Marine boundary layer clouds at the heart of tropical cloud feedback uncertainties in climate models. *Geophys. Res. Lett.*, **32**, L20806, doi:10.1029/2005GL023851.

Brenguier, J. L., H. Pawlowska, L. Schuller, R. Preusker, J. Fischer, and Y. Fouquart, 2000: Radiative properties of boundary layer clouds: Droplet effective radius versus number concentration. *J. Atmos. Sci.*, **57**, 803–821, doi:10.1175/1520-0469(2000)057⟨0803:RPOBLC⟩2.0.CO;2.

Bretherton, C. S., and P. N. Blossey, 2014: Low cloud reduction in a greenhouse-warmed climate: Results from Lagrangian LES of a subtropical marine cloudiness transition. *J. Adv. Model. Earth Syst.*, **6**, 91–114, doi:10.1002/2013MS000250.

Bretherton, C. S., P. N. Blossey, and C. R. Jones, 2013: Mechanisms of marine low cloud sensitivity to idealized climate perturbations: A single-LES exploration extending the CGILS cases. *J. Adv. Model. Earth Syst.*, **5**, 316–337, doi:10.1002/jame.20019.

Brient, F., and S. Bony, 2013: Interpretation of the positive low cloud feedback predicted by a climate model under global warming. *Climate Dyn.*, **40**, 2415–2431, doi:10.1007/s00382-011-1279-7.

Ceppi, P., and D. L. Hartmann, 2015: Connections between clouds, radiation, and midlatitude dynamics: A review. *Curr. Clim. Change Rep.*, **1**, 94–102, doi:10.1007/s40641-015-0010-x.

Ceppi, P., D. L. Hartmann, and M. J. Webb, 2016a: Mechanisms of the negative shortwave cloud feedback in middle to high latitudes. *J. Climate*, **29**, 139–157, doi:10.1175/JCLI-D-15-0327.1.

Ceppi, P., D. T. McCoy, and D. L. Hartmann, 2016b: Observational evidence for a negative shortwave cloud feedback in middle to high latitudes. *Geophys. Res. Lett.*, **43**, 1331–1339, doi:10.1002/2015GL067499.

Chelton, D. B., M. G. Schlax, M. H. Freilich, and R. F. Milliff, 2004: Satellite measurements reveal persistent small-scale features in ocean winds. *Science*, **303**, 978–983, doi:10.1126/science.1091901.

Chepfer, H., S. Bony, D. M. Winker, G. Cesana, J. Dufresne, P. Minnis, C. Stubenrauch, and S. Zeng, 2010: The GCM Oriented CALIPSO Cloud Product (CALIPSO-GOCCP). *J. Geophys. Res.*, **115**, D00H16, doi:10.1029/2009JD012251.

Clement, A. C., R. Burgman, and J. R. Norris, 2009: Observational and model evidence for positive low-level cloud feedback. *Science*, **325**, 460–464, doi:10.1126/science.1171255.

Crueger, T., and B. stevens, 2015: The effect of atmospheric radiative heating by clouds on the Madden-Julian oscillation. *J. Adv. Model. Earth Syst.*, **6**, 854–864, doi:10.1002/2015MS000434.

de Boyer Montégut, C., J. Vialard, S. S. C. Shenoi, D. Shankar, F. Durand, C. Ethé, and G. Madec, 2007: Simulated seasonal and interannual variability of the mixed layer heat budget in the northern Indian Ocean. *J. Climate*, **20**, 3249–3268, doi:10.1175/JCLI4148.1.

Dee, D. P., and Coauthors, 2011: The ERA-Interim reanalysis: configuration and performance of the data assimilation system. *Quart. J. Roy. Meteor. Soc.*, **137**, 553–597, doi:10.1002/qj.828.

Delworth, T. L., and Coauthors, 2006: GFDL's CM2 global coupled climate models. Part I: Formulation and simulation characteristics. *J. Climate*, **19**, 643–674, doi:10.1175/JCLI3629.1.

Durgadoo, J. V., B. R. Loveday, C. J. C. Reason, P. Penven, and A. Biastoch, 2013: Agulhas leakage predominantly responds to the Southern Hemisphere westerlies. *J. Phys. Oceanogr.*, **43**, 2113–2131, doi:10.1175/JPO-D-13-047.1.

Enomoto, T., A. Kuwano-Yoshida, N. Komori, and W. Ohfuchi, 2008: Description of AFES 2: Improvements for high-resolution and coupled simulations. *High Resolution Numerical Modelling of the Atmosphere and Ocean*, H. Kevin and O. Wataru, Eds., Springer, 77–97.

Fermepin, S., and S. Bony, 2014: Influence of low-cloud radiative effects on tropical circulation and precipitation. *J. Adv. Model. Earth Syst.*, **6**, 513–526, doi:10.1002/2013MS000288.

Frenger, I., N. Gruber, and M. Münnich, 2013: Imprint of Southern Ocean eddies on winds, clouds and rainfall. *Nat. Geosci.*, **6**, 608–612, doi:10.1038/NGEO1863.

Frierson, D. M. W., and Y.-T. Hwang, 2012: Extratropical influence on ITCZ shifts in slab ocean simulations of global warming. *J. Climate*, **25**, 720–733, doi:10.1175/JCLI-D-11-00116.1.

Gill, A. E., 1980: Some simple solutions for heat-induced tropical circulation. *Quart. J. Roy. Meteor. Soc.*, **106**, 447–462, doi:10.1002/qj.49710644905.

Gordon, C. T., A. Rosati, and R. Gudgel, 2000: Tropical sensitivity of a coupled model to specified ISCCP low clouds. *J. Climate*, **13**, 2239–2260, doi:10.1175/1520-0442(2000)013⟨2239:TSOACM⟩2.0.CO;2.

Graham, N. E., and T. P. Barnett, 1987: Sea surface temperature, surface wind divergence, and convection over tropical oceans. *Science*, **30**, 657–659, doi:10.1126/science.238.4827.657.

Graham, R. M., and A. M. De Boer, 2013: The dynamical subtropical front. *J. Geophys. Res.*, **118**, 5676–5685, doi:10.1002/jgrc.20408.

Grise, K. M., B. Medeiros, J. J. Benedict, and J. G. Olson, 2019: Investigating the influence of cloud radiative effects on the extratropical storm tracks. *Geophys. Res. Lett.*, **46**, 7700–7707, doi:10.1029/2019GL083542.

Grise, K. M., L. M. Polvani, and J. T. Fasullo, 2015: Reexamining the relationship between climate sensitivity and the southern hemisphere radiation budget in CMIP models. *J. Climate*, **28**, 9298–9312, doi:10.1175/JCLI-D-15-0031.1.

Grosvenor, D. P., and R. Wood, 2014: The effect of solar zenith angle on MODIS cloud optical and microphysical retrievals within marine liquid water clouds. *Atmos. Chem. Phys.*, **14**, 7291–7321, doi:10.5194/acp-14-7291-2014.

Hair Jr., J. F., W. C. Black, B. J. Babin, and R. E. Anderson, 2010: *Multivariate Data Analysis*. Pearson, 734 pp.

Harada, Y., and Coauthors, 2016: The JRA-55 reanalysis: Representation of atmospheric circulation and climate variability. *J. Meteor. Soc. Japan*, **94**, 269–302, doi:10.2151/jmsj.2016-015.

Hartmann, D. L., and D. A. Short, 1980: On the use of earth radiation budget statistics for studies of clouds and climate. *J. Atmos. Sci.*, **37**, 1233–1250, doi:10.1175/1520-0469(1980)037⟨1233:OTUOER⟩2.0.CO;2.

Holton, J. R., and G. J. Hakim, 2012: *An Introduction to Dynamic Meteorology*. Academic Press, 552 pp.

Hoskins, B. J., M. E. McIntyre, and A. W. Robertson, 1985: On the use and significance of isentropic potential vorticity maps. *J. Meteor. Soc. Japan*, **111**, 877–946, doi:10.1002/qj.49711147002.

Hosoda, S., T. Ohira, K. Sato, and T. Suga, 2010: Improved description of global mixed-layer depth using Argo profiling floats. *J. Oceanogr.*, **66**, 773–787, doi:10.1007/s10872-010-0063-3.

Hotta, D., and H. Nakamura, 2011: On the significance of sensible heat supply from the ocean in the maintenance of the mean baroclinicity along storm tracks. *J. Climate*, **24**, 3377–3401, doi:10.1175/2010JCLI3910.1.

Huang, B., and Z. Z. Hu, 2007: Cloud-SST feedback in southeastern tropical Atlantic anomalous events. *Geophys. Res. Lett.*, **112**, C03015, doi:10.1029/2006JC003626.

Hubanks, P., S. Platnick, M. King, and B. Ridgway, 2016: MODIS Atmosphere L3 Gridded Product Algorithm Theoretical Basis Document (ATBD) and Users Guide. [Available online at https://modis-images.gsfc.nasa.gov/_docs/L3_ATBD_C6.pdf.], 122 pp.

Huffman, G. J., and Coauthors, 2007: The TRMM Multisatellite Precipitation Analysis (TMPA): Quasi-global, multiyear, combined-sensor precipitation estimates at fine scales. *J. Hydrometeor.*, **77**, 38–55, doi:10.1175/JHM560.1.

Hwang, Y.-T., and D. M. W. Frierson, 2013: Link between the double-Intertropical Convergence Zone problem and cloud biases over the Southern Ocean. *Proc. Natl. Acad. Sci. (USA)*, **110**, 4935–4940, doi:10.1073/pnas.1213302110.

Inatsu, M., and B. Hoskins, 2004: The zonal asymmetry of the Southern Hemisphere winter storm track. *J. Climate*, **17**, 4882–4892, doi:10.1175/JCLI-3232.1.

Izumo, T., C. de Boyer Montégut, J. Luo, S. K. Behera, S. Masson, and T. Yamagata, 2008: The role of the western Arabian Sea upwelling in Indian monsoon rainfall variability. *J. Climate*, **21**, 5603–5623, doi:10.1175/2008JCLI2158.1.

Johnson, N. C., and S.-P. Xie, 2010: Changes in the sea surface temperature threshold for tropical convection. *Nat. Geosci.*, **3**, 842–845, doi:10.1038/ngeo1008.

Kamae, Y., T. Ogura, H. Shiogama, and M. Watanabe, 2016: Recent progress toward reducing the uncertainty in tropical low cloud feedback and climate sensitivity: A review. *Geosci. Lett.*, **3**, 17, doi:10.1186/s40562-016-0053-4.

Kanamitsu, M., W. Ebisuzaki, J. Woollen, S.-K. Yang, J. J. Hnilo, M. Fiorino, and G. L. Potter, 2002: NCEP-DOE AMIP-II Reanalysis (R-2). *Bull. Amer. Meteor. Soc.*, **83**, 1631–1643, doi:10.1175/BAMS-83-11-1631.

Karlsson, J., G. Svensson, and H. Rodhe, 2008: Cloud radiative forcing of subtropical low level clouds in global models. *Climate Dyn.*, **30**, 779–788, doi:10.1007/s00382-007-0322-1.

Kataoka, T., T. Tozuka, S. Behera, and T. Yamagata, 2014: On the Ningaloo Niño/Niña. *Climate Dyn.*, **43**, 1463–1482, doi:10.1007/s00382-013-1961-z.

Kawai, H., T. Koshiro, and M. J. Webb, 2017: Interpretation of factors controlling low cloud cover and low cloud feedback using a unified predictive index. *J. Climate*, **30**, 9119–9131, doi:10.1175/JCLI-D-16-0825.1.

Kawamura, R., T. Matsuura, and S. Iizuka, 1988: Role of equatorially asymmetric sea surface temperature anomalies in the Indian Ocean in the Asian summer monsoon and El Niño-Southern Oscillation coupling. *J. Geophys. Res.*, **106**, 4681–4693, doi:10.1029/2000JD900610.

King, M. D., S. Platnick, P. A. Hubanks, G. T. Arnold, E. G. Moody, G. Wind, and B. Wind, 2006: Collection 005 change summary for the MODIS cloud optical property (06_OD) algorithm. NASA Rep., Version 3.1 23pp.

Klein, S., and C. Jakob, 1999: Validation and sensitivities of frontal clouds simulated by the ECMWF model. *Mon. Wea. Rev.*, **127**, 2514–2531, doi:10.1175/1520-0493(1999)127⟨2514:VASOFC⟩2.0.CO;2.

Klein, S. A., A. Hall, J. R. Norris, and R. Pincus, 2017: Low-cloud feedbacks from cloud-controlling factors: A review. *Surv. Geophys.*, **38**, 1307–1329, doi:10.1007/s10712-017-9433-3.

Klein, S. A., and D. L. Hartmann, 1993: The seasonal cycle of low stratiform clouds. *J. Climate*, **6**, 1587–1606, doi:10.1175/1520-0442(1993)006⟨1587:TSCOLS⟩2.0.CO;2.

Kobayashi, S., and Coauthors, 2015: The JRA-55 reanalysis: General specifications and basic characteristics. *J. Meteor. Soc. Japan*, **93**, 5–48, doi:10.2151/jmsj.2015-001.

Koike, M., N. Asano, H. Nakamura, S. Sakai, T. M. Nagao, and T. Y. Nakajima, 2016: Modulations of aerosol impacts on cloud microphysics induced by the warm kuroshio current under the East Asian winter monsoon. *J. Geophys. Res.*, **121**, 282–297, doi:10.1002/2016JD025375.

Koike, M., and Coauthors, 2012: Measurements of regional-scale aerosol impacts on cloud microphysics over the East China Sea: Possible influences of warm sea surface temperature over the Kuroshio Ocean Current. *J. Geophys. Res.*, **117**, D17205, doi:10.1029/2011JD017324.

Komurcu, M., and Coauthors, 2014: Intercomparison of the cloud water phase among global climate models. *J. Geophys. Res.*, **119**, 3372–3400, doi:10.1002/2013JD021119.

Koseki, S., T. Nakamura, H. Mitsudera, and Y. Wang, 2012: Modeling low-level clouds over the Okhotsk Sea in summer: Cloud formation and its effects on the Okhotsk high. *J. Geophys. Res.*, **117**, D05208, doi:10.1029/2011JD016462.

Koshiro, T., and M. Shiotani, 2014: Relationship between low stratiform cloud amount and estimated inversion strength in the lower troposphere over the global ocean in terms of cloud types. *J. Meteor. Soc. Japan*, **92**, 107–120, doi:10.2151/jmsj.2014-107.

Koshiro, T., S. Yukimoto, and M. Shiotani, 2017: Interannual variability in low stratiform cloud amount over the summertime North Pacific in terms of cloud types. *J. Climate*, **30**, 6107–6121, doi:10.1175/JCLI-D-16-0898.1.

Kraucunas, I., and D. L. Hartmann, 2007: Tropical stationary waves in a nonlinear shallow-water model with realistic basic states. *J. Atmos. Sci.*, **64**, 2540–2557, doi:10.1175/JAS3920.1.

Kraus, E. B., and J. S. Turner, 1967: A one-dimensional model of the seasonal thermocline II. *Tellus*, **19**, 98–106, doi:10.3402/tellusa.v19i1.9753.

Kuwano-Yoshida, A., T. Enomoto, and W. Ohfuchi, 2010: An improved PDF cloud scheme for climate simulations. *Quart. J. Roy. Meteor. Soc.*, **136**, 1583–1597, doi:10.1002/qj.660.

Kwon, Y.-O., M. A. Alexander, N. A. Bond, C. Frankignoul, H. Nakamura, B. Qiu, and L. Thompson, 2010: Role of the Gulf Stream and Kuroshio-Oyashio systems in large-scale atmosphere-ocean interaction: A review. *J. Climate*, **23**, 3249–3281, doi:10.1175/2010JCLI3343.1.

Lana, A., and Coauthors, 2011: An updated climatology of surface dimethlysulfide concentrations and emission fluxes in the global ocean. *Global Biogeochemical Cycles*, **25**, GB1004, doi:10.1029/2010GB003850.

Lee, S.-K., C. R. Mechoso, C. Wang, and J. D. Neelin, 2013: Interhemispheric influence of the northern summer monsoons on southern subtropical anticyclones. *J. Climate*, **26**, 10 193–10 204, doi:10.1175/JCLI-D-13-00106.1.

Levitus, S., 1987: Meridional Ekman heat fluxes for the world ocean and individual ocean basins. *J. Phys. Oceanogr.*, **17**, 1484–1492, doi:10.1175/1520-0485(1987)017⟨1484:MEHFFT⟩2.0.CO;2.

Li, J., J. Huang, K. Stamnes, T. Wang, Q. Lv, and H. Jin, 2015a: A global survey of cloud overlap based on CALIPSO and CloudSat measurements. *Atmos. Chem. Phys.*, **10**, 519–536, doi:10.5194/acp-15-519-2015.

Li, W., L. Li, M. Ting, and Y. Liu, 2012: Intensification of Northern Hemisphere subtropical highs in a warming climate. *Nat. Geosci.*, **5**, 830–834, doi:10.1038/NGEO1590.

Li, W., and Coauthors, 2013: Intensification of the Southern Hemisphere summertime subtropical anticyclones in a warming climate. *Geophys. Res. Lett.*, **40**, 5959–5964, doi:10.1002/2013GL058124.

Li, Y., D. W. J. Thompson, and S. Bony, 2015b: The influence of atmospheric cloud radiative effects on the large-scale atmospheric circulation. *J. Climate*, **28**, 7263–7278, doi:10.1175/JCLI-D-14-00825.1.

Li, Y., D. W. J. Thompson, S. Bony, and T. M. Merlis, 2019: Thermodynamic control on the poleward shift of the extratropical jet in climate change simulations: The role of rising high clouds and their radiative effects. *J. Climate*, **32**, 917–934, doi:10.1175/JCLI-D-18-0417.1.

Li, Y., D. W. J. Thompson, and Y. Huang, 2017: The influence of atmospheric cloud radiative effects on the large-scale stratospheric circulation. *J. Climate*, **30**, 5621–5635, doi:10.1175/JCLI-D-16-0643.1.

Lilly, D. K., 1968: Models of cloud-topped mixed layers under a strong inversion. *Quart. J. Roy. Meteor. Soc.*, **94**, 292–309, doi:10.1002/qj.49709440106.

Lindzen, R. S., and A. V. Hou, 1988: Hadley circulations for zonally averaged heating centered off the equator. *J. Atmos. Sci.*, **45**, 2416–2427, doi:10.1175/1520-0469(1988)045⟨2416:HCFZAH⟩2.0.CO;2.

Lindzen, R. S., and S. Nigam, 1987: On the role of sea surface temperature gradients in forcing low-level winds and convergence in the tropics. *J. Atmos. Sci.*, **44**, 2418–2436, doi:10.1175/1520-0469(1987)044⟨2418:OTROSS⟩2.0.CO;2.

Liu, J., T. Xiao, and L. Chen, 2011: Intercomparisons of air-sea heat fluxes over the Southern Ocean. *J. Climate*, **24**, 1198–1211, doi:10.1175/2010JCLI3699.1.

Liu, J.-W., S.-P. Xie, J. R. Norris, and S.-P. Zhang, 2014: Low-level cloud response to the Gulf Stream front in winter using CALIPSO. *J. Climate*, **27**, 4421–4432, doi:10.1175/JCLI-D-13-00469.1.

Loveday, B. R., J. V. Durgadoo, C. J. C. Reason, A. Biastoch, and P. Penven, 2014: Decoupling of the Agulhas leakage from the Agulhas Current. *J. Phys. Oceanogr.*, **44**, 1776–1797, doi:10.1175/JPO-D-13-093.1.

Ma, C.-C., C. R. Mechoso, W. A. Robertson, and A. Arakawa, 1996: Peruvian stratus clouds and the tropical Pacific circulation: A coupled ocean-atmosphere GCM study. *J. Climate*, **9**, 1635–1645, doi:10.1175/1520-0442(1996)009⟨1635:PSCATT⟩2.0.CO;2.

Marchand, R., T. Ackerman, M. Smyth, and W. B. Rossow, 2010: A review of cloud top height and optical depth histograms from MISR, ISCCP, and MODIS. *J. Geophys. Res.*, **115**, D16206, doi:10.1029/2009JD013422.

Masunaga, R., H. Nakamura, T. Miyasaka, K. Nishii, and Y. Tanimoto, 2015: Separation of climatological imprints of the Kuroshio Extension and Oyashio fronts on the wintertime atmospheric boundary layer: Their sensitivity to SST resolution prescribed for atmospheric reanalysis. *J. Climate*, **28**, 1764–1787, doi:10.1175/JCLI-D-14-00314.1.

Masunaga, R., H. Nakamura, B. Taguchi, and T. Miyasaka, 2020: Processes shaping the frontal-scale time-mean surface wind convergence patterns around the Kuroshio Extension in winter. *J. Climate*, **33**, 3–25, doi:10.1175/JCLI-D-19-0097.1.

Matsuno, T., 1966: Quasi-geostrophic motions in the equatorial area. *J. Meteor. Soc. Japan*, **44**, 25–43, doi:10.2151/jmsj1965.44.1_25.

Mauger, G. S., and J. R. Norris, 2010: Assessing the impact of meteorological history on subtropical cloud fraction. *J. Climate*, **23**, 2926–2940, doi:10.1175/2010JCLI3272.1.

McCoy, D. T., S. M. Burrows, R. Wood, D. P. Grosvenor, S. M. Elliott, P.-L. Ma, P. J. Rasch, and D. L. Hartmann, 2015a: Natural aerosols explain seasonal and spatial patterns of Southern Ocean cloud albedo. *Sci. Adv.*, **1**, e1500157, doi:10.1126/sciadv.1500157.

McCoy, D. T., R. Eastman, D. L. Hartmann, and R. Wood, 2017: The change in low cloud cover in a warmed climate inferred from AIRS, MODIS, and ERA-Interim. *J. Climate*, **30**, 3609–3620, doi:10.1175/JCLI-D-15-0734.1.

McCoy, D. T., D. L. Hartmann, and D. P. Grosvenor, 2014: Observed Southern Ocean cloud properties and shortwave reflection. Part I: Calculation of SW flux from observed cloud properties. *J. Climate*, **27**, 8836–8857, doi:10.1175/JCLI-D-14-00287.1.

McCoy, D. T., D. L. Hartmann, M. D. Zelinka, P. Ceppi, and D. P. Grosvenor, 2015b: Mixed-phase cloud physics and Southern Ocean cloud feedback in climate models. *J. Geophys. Res.*, **120**, 9539–9554, doi:10.1002/2015JD023603.

McCoy, D. T., I. Tan, D. L. Hartmann, M. D. Zelinka, and T. Storelvmo, 2016: On the relationships among cloud cover, mixed-phase partitioning, and planetary albedo in GCMs. *J. Adv. Model. Earth Syst.*, **8**, 650–668, doi:10.1002/2015MS000589.

Merlis, T. M., 2015: Direct weakening of tropical circulations from masked CO_2 radiative forcing. *Proc. Natl. Acad. Sci. (USA)*, **112**, 13 167–13 171, doi:10.1173/pnas.1508268112.

Miyamoto, A., H. Nakamura, and T. Miyasaka, 2018: Influence of the subtropical high and storm track on low-cloud fraction and its seasonality over the south Indian Ocean. *J. Climate*, **31**, 4017–4039, doi:10.1175/JCLI-D-17-0229.1.

Miyasaka, T., and H. Nakamura, 2005: Structure and formation mechanisms of the Northern Hemisphere summertime subtropical highs. *J. Climate*, **18**, 5046–5065, doi:10.1175/JCLI3599.1.

Miyasaka, T., and H. Nakamura, 2010: Structure and mechanisms of the Southern Hemisphere summertime subtropical anticyclones. *J. Climate*, **23**, 2115–2130, doi:10.1175/2009JCLI3008.1.

Morioka, Y., J. V. Ratnam, W. Sasaki, and Y. Masumoto, 2013: Generation mechanism of the South Pacific subtropical dipole. *J. Climate*, **26**, 6033–6045, doi:10.1175/JCLI-D-12-00648.1.

Morioka, Y., T. Tozuka, and T. Yamagata, 2010: Climate variability in the southern Indian Ocean as revealed by self-organizing maps. *Climate Dyn.*, **35**, 1059–1072, doi:10.1007/s00382-010-0843-x.

Morioka, Y., T. Tozuka, and T. Yamagata, 2011: On the growth and decay of the subtropical dipole mode in the South Atlantic. *J. Climate*, **24**, 5538–5554, doi:10.1175/2011JCLI4010.1.

Myers, T. A., C. R. Mechoso, and M. J. DeFlorio, 2018: Coupling between marine boundary layer clouds and summer-to-summer sea surface temperature variability over the North Atlantic and Pacific. *Climate Dyn.*, **50**, 955–969, doi:10.1007/s00382-017-3651-8.

Myers, T. A., and J. R. Norris, 2013: Observational evidence that enhanced subsidence reduces subtropical marine boundary layer cloudiness. *J. Climate*, **26**, 7507–7524, doi:10.1175/JCLI-D-12-00736.1.

Myers, T. A., and J. R. Norris, 2015: On the relationships between subtropical clouds and meteorology in observations and CMIP3 and CMIP5 models. *J. Climate*, **28**, 2945–2967, doi:10.1175/JCLI-D-14-00475.1.

Myers, T. A., and J. R. Norris, 2016: Reducing the uncertainty in subtropical cloud feedback. *Geophys. Res. Lett.*, **43**, 2144–2148, doi:10.1002/2015GL067416.

Nakamura, H., 1992: Midwinter suppression of baroclinic wave activity in the Pacific. *J. Atmos. Sci.*, **49**, 1629–1642, doi:10.1175/1520-0469(1992)049⟨1629:MSOBWA⟩2.0.CO;2.

Nakamura, H., 2012: Atmospheric science: Future oceans under pressure. *Nat. Geosci.*, **5**, 768–769, doi:10.1038/ngeo1623.

Nakamura, H., T. Miyasaka, Y. Kosaka, and K. T. M. Honda, 2010: Northern Hemisphere extratropical tropospheric planetary waves and their low-frequency variability: Their vertical structure and interaction with transient eddies and surface thermal contrasts. *Climate Dynamics: Why Does Climate Vary?*, *Geophys. Monogr.*, Vol. 189, Amer. Geophys.Union, 149–179, doi:10.1029/2008GM000789.

Nakamura, H., T. Sampe, A. Goto, W. Ohfuchi, and S.-P. Xie, 2008: On the importance of midlatitude oceanic frontal zones for the mean state and dominant variability in the tropospheric circulation. *Geophys. Res. Lett.*, **35**, L15709, doi:10.1029/2008GL034010.

Nakamura, H., T. Sampe, Y. Tanimoto, and A. Shimpo, 2004: Observed associations among storm tracks, jet streams and midlatitude oceanic fronts. *Earth's Climate The Ocean-Atmosphere Interaction*, *Geophys. Monogr.*, Vol. 147, Amer. Geophys.Union, 329–345.

Nakamura, H., and A. Shimpo, 2004: Seasonal variations in the Southern Hemisphere storm tracks and jet streams as revealed in a reanalysis dataset. *J. Climate*, **17**, 1828–1844, doi:10.1175/1520-0442(2004)017⟨1828:SVITSH⟩2.0.CO;2.

Nam, C., S. Bony, J.-L and Dufresne, and H. Chepfer, 2012: The 'too few, too bright' tropical low-cloud problem in CMIP5 models. *Geophys. Res. Lett.*, **39**, L21801, doi:10.1029/2012GL053421.

Nigam, S., 1997: The annual warm to cold phase transition in the eastern equatorial Pacific: Diagnosis of the role of stratus cloud-top cooling. *J. Climate*, **10**, 2447–2467, doi:10.1175/1520-0442(1997)010⟨2447:TAWTCP⟩2.0.CO;2.

Nonaka, M., H. Nakamura, B. Taguchi, N. Komori, A. Kuwano-Yoshida, and K. Takaya, 2009: Air-sea heat exchanges characteristic of a prominent midlatitude oceanic front in the South Indian Ocean as simulated in a high-resolution coupled GCM. *J. Climate*, **22**, 6515–6535, doi:10.1175/2009JCLI2960.1.

Norris, J. R., 1998: Low cloud type over the ocean from surface observations. Part II: Geographical and seasonal variations. *J. Climate*, **11**, 383–403, doi:10.1175/1520-0442(1998)011⟨0383:LCTOTO⟩2.0.CO;2.

Norris, J. R., and S. F. Iacobellis, 2005: North Pacific cloud feedbacks inferred from synoptic-scale dynamic and thermodynamic relationships. *J. Climate*, **18**, 4862–4878, doi:10.1175/JCLI3558.1.

Norris, J. R., and S. A. Klein, 2000: Low cloud type over the ocean from surface observations. Part III: Relationship to vertical motion and the regional surface synoptic environment. *J. Climate*, **13**, 245–256, doi:10.1175/1520-0442(2000)013⟨0245:LCTOTO⟩2.0.CO;2.

Norris, J. R., and C. B. Leovy, 1994: Interannual variability in stratiform cloudiness and sea surface temperature. *J. Climate*, **7**, 1915–1925, doi:10.1175/1520-0442(1994)007⟨1915:IVISCA⟩2.0.CO;2.

Oettli, P., Y. Morioka, and T. Yamagata, 2016: A regional climate mode discovered in the North Atlantic: Dakar Niño/Niña. *Sci. Rep.*, **6**, doi:10.1038/srep18782.

Ogawa, F., H. Nakamura, K. Nishii, and T. M. A. Kuwano-Yoshida, 2012: Dependence of the climatological axial latitudes of the tropospheric westerlies and storm tracks on the latitude of an extratropical oceanic front. *Geophys. Res. Lett.*, **39**, L05804, doi:10.1029/2011GL049922.

Ogawa, F., and T. Spengler, 2019: Prevailing surface wind direction during air-sea heat exchange. *J. Climate*, **32**, 5601–5617, doi:10.1175/JCLI-D-18-0752.1.

Ohfuchi, W., and Coauthors, 2004: 10-km mesh meso-scale resolving simulations of the global atmosphere on the Earth Simulator - preliminary outcomes of AFES (AGCM for the Earth Simulator). *J. Earth SImul.*, **1**, 8–34.

Ohfuchi, W., H. Sasaki, Y. Masumoto, and H. Nakamura, 2007: ”virtual” atmospheric and oceanic circulations in the Earth Simulator. *Bull. Amer. Meteor. Soc.*, **88**, 861–866, doi:10.1175/BAMS-88-6-861.

Ohishi, S., T. Tozuka, and N. Komori, 2016: Frontolysis by surface heat flux in the Agulhas Return Current region with a focus on mixed layer processes: Observation and a high-resolution CGCM. *Climate Dyn.*, **47**, 3993–4007, doi:10.1007/s00382-016-3056-0.

O’Neill, L. W., S. K. Esbensen, N. Thum, R. M. Samelson, and D. B. Chelton, 2010: Dynamical analysis of the boundary layer and surface wind responses to mesoscale SST perturbations. *J. Climate*, **23**, 559–581, doi:10.1175/2009JCLI2662.1.

Onogi, K., and Coauthors, 2007: The JRA-25 reanalysis. *J. Meteor. Soc. Japan*, **85**, 369–432, doi:10.2151/jmsj.85.369.

O’Reilly, C. H., S. Minobe, A. Kuwano-Yoshida, and T. Woollings, 2017: The Gulf Stream influence on wintertime North Atlantic jet variability. *Quart. J. Roy. Meteor. Soc.*, **143**, 173–183, doi:10.1002/qj.2907.

Paulson, C. A., and J. J. Simpson, 1977: Irradiance measurements in the upper ocean. *J. Phys. Oceanogr.*, **7**, 952–956, doi:10.1175/1520-0485(1977)007⟨0952:IMITUO⟩2.0.CO;2.

Philander, S. C., H. D. Gu, D. Halpern, G. Lambert, N.-C. Lau, T. Li, and R. C. Pacanowski, 1996: Why the ITCZ is mostly north of the equator. *J. Climate*, **9**, 2958–2972, doi:10.1175/1520-0442(1996)009⟨2958:WTIIMN⟩2.0.CO;2.

Pincus, R., S. Platnick, S. A. Ackerman, R. S. Hemler, and R. J. P. Hofmann, 2012: Reconciling simulated and observed views of clouds: MODIS, ISCCP, and the limits of instrument simulators. *J. Climate*, **25**, 4699–4720, doi:10.1175/JCLI-D-11-00267.1.

Plumb, R. A., 1985: On the three-dimensional propagation of stationary waves. *J. Atmos. Sci.*, **42**, 217–229, doi:10.1175/1520-0469(1985)042⟨0217:OTTDPO⟩2.0.CO;2.

Qiu, B., and K. A. Kelly, 1993: Upper-ocean heat balance in the Kuroshio Extension region. *J. Phys. Oceanogr.*, **23**, 2027–2041, doi:10.1175/1520-0485(1993)023⟨2027:UOHBIT⟩2.0.CO;2.

Qu, X., A. Hall, S. A. Klein, and P. M. Caldwell, 2014: On the spread of changes in marine low cloud cover in climate model simulations of the 21st century. *Climate Dyn.*, **42**, 2603–2626, doi:10.1007/s00382-013-1945-z.

Qu, X., A. Hall, S. A. Klein, and A. M. DeAngelis, 2015: Positive tropical marine low-cloud cover feedback inferred from cloud-controlling factors. *Geophys. Res. Lett.*, **42**, 7767–7775, doi:10.1002/2015GL065627.

Rädel, G., T. Mauritsen, B. Stevens, D. Dommenget, D. Matei, K. Bellomo, and A. Clement, 2016: Amplification of El Niño by cloud longwave coupling to atmospheric circulation. *Nat. Geosci.*, **9**, 106–111, doi:10.1038/NGEO2630.

Randall, D. A., J. A. Coakley Jr., C. W. Fairall, R. A. Kropfli, and D. H. Lenschow, 1984: Outlook for research on subtropical marine stratification clouds. *Bull. Amer. Meteor. Soc.*, **65**, 1290–1301, doi:10.1175/1520-0477(1984)065⟨1290:OFROSM⟩2.0.CO;2.

Randall, D. A., Harshvardhan, D. A. Dazlich, and T. G. Corsett, 1989: Interactions among radiation, convection, and large-scale dynamics in a general circulation model. *J. Atmos. Sci.*, **46**, 1943–1970, doi:10.1175/1520-0469(1989)046⟨1943:IARCAL⟩2.0.CO;2.

Reynolds, R. W., C. Liu, D. B. Chelton, K. S. Casey, and M. G. Schlax, 2007: Daily high-resolution-blended analyses for sea surface temperature. *J. Climate*, **20**, 5473–5496, doi:10.1175/2007JCLI1824.1.

Richter, I., and C. R. Mechoso, 2004: Orographic influences on the annual cycle of Namibian stratocumulus clouds. *Geophys. Res. Lett.*, **31**, L24108, doi:10.1029/2004GL020814.

Richter, I., and C. R. Mechoso, 2006: Orographic influences on subtropical stratocumulus. *J. Atmos. Sci.*, **63**, 2585–2601, doi:10.1175/JAS3756.1.

Richter, I., and C. R. Mechoso, 2008: What determines the position and intensity of the South Atlantic anticyclone in austral winter?—An AGCM study. *J. Climate*, **21**, 214–229, doi:10.1175/2007JCLI1802.1.

Rieck, M., L. Nuijens, and B. Stevens, 2012: Marine boundary layer cloud feedbacks in a constant relative humidity atmosphere. *J. Atmos. Sci.*, **69**, 2538–2550, doi:10.1175/JAS-D-11-0203.1.

Rodwell, M. J., and B. J. Hoskins, 1995: A model of the Asian summer monsoon. Part II: Cross-equatorial flow and PV behavior. *J. Atmos. Sci.*, **52**, 1341–1356, doi:10.1175/1520-0469(1995)052⟨1341:AMOTAS⟩2.0.CO;2.

Rodwell, M. J., and B. J. Hoskins, 1996: Monsoons and the dynamics of deserts. *Quart. J. Roy. Meteor. Soc.*, **122**, 1385–1404, doi:10.1002/qj.49712253408.

Rodwell, M. J., and B. J. Hoskins, 2001: Subtropical anticyclones and summer monsoons. *J. Climate*, **14**, 3192–3211, doi:10.1175/1520-0442(2001)014⟨3192:SAASM⟩2.0.CO;2.

Schott, F. A., and J. P. McCreary Jr., 2001: The monsoon circulation of the Indian Ocean. *Prog. Oceanogr.*, **51**, 1–123.

Schott, F. A., S.-P. Xie, and J. P. McCreary Jr., 2009: Indian ocean circulation and climate variablity. *Rev. Geophys.*, **47**, RG1002, doi:10.1029/2007RG000245.

Seager, R., R. Murtugudde, N. Naik, A. Clement, N. Gordon, and J. Miller, 2003: Air-sea interaction and the seasonal cycle of the subtropical anticyclones. *J. Climate*, **16**, 1948–1966, doi:10.1175/1520-0442(2003)016⟨1948:AIATSC⟩2.0.CO;2.

Seethala, C., J. R. Norris, and T. A. Myers, 2015: How has subtropical stratocumulus and associated meteorology changed since the 1980s? *J. Climate*, **28**, 8396–8410, doi:10.1175/JCLI-D-15-0120.1.

Senior, C. A., and J. F. B. Mitchell, 1993: Carbon dioxide and climate: The impact of cloud parameterization. *J. Climate*, **6**, 393–418, doi:10.1175/1520-0442(1993)006⟨0393:cdacti⟩2.0.co;2.

Shannon, L. V., A. J. Boyd, G. B. Bundrit, and J. Taunton-Clark, 1986: On the existence of an El niño type phenomenon in the Benguela system. *J. Mar. Sci.*, **44**, 495–520, doi:10.1357/002224086788403105.

Shimada, T., and S. Minobe, 2011: Global analysis of the pressure adjustment mechanism over sea surface temperature fronts using AIRS/Aqua data. *Geophys. Res. Lett.*, **38**, L06704, doi:10.1029/2010GL046625.

Slingo, A., and J. M. Slingo, 1988: The response of a general circulation model to cloud longwave radiative forcing. I:Introduction and initial experiments. *Quart. J. Roy. Meteor. Soc.*, **114**, 1027–1062, doi:10.1002/qj.49711448209.

Slingo, A., and J. M. Slingo, 1991: The response of a general circulation model to cloud longwave radiative forcing. II:Further studies. *Quart. J. Roy. Meteor. Soc.*, **117**, 333–364, doi:10.1002/qj.49711749805.

Smith, R. L., A. Huyer, J. S. Godfrey, and J. A. Church, 1991: The Leeuwin Current off Western Australia, 1986-1987. *J. Phys. Oceanogr.*, **21**, 323–345, doi:10.1175/1520-0485(1991)021⟨0323:TLCOWA⟩2.0.CO;2.

Smith, S. R., P. J. Hughes, and M. A. Bourassa, 2011: A comparison of nine monthly air-sea flux products. *Int. J. Climatol.*, **31**, 1002–1027, doi:10.1002/joc.2225.

Stevens, B., S. Bony, and M. J. Webb, 2012: Clouds On-Off Klimate Intercomparison Experiment (COOKIE). [Available online at http://www.euclipse.eu/downloads/Cookie.pdf.], 12 pp.

Szczodrak, M., P. H. Austin, , and P. B. Krummel, 2001: Variability of optical depth and effective radius in marine stratocumulus clouds. *J. Atmos. Sci.*, **58**, 2912–2926, doi:10.1175/1520-0469(2001)058⟨2912:VOODAE⟩2.0.CO;2.

Taguchi, B., H. Nakamura, M. Nonaka, and S.-P. Xie, 2009: Influences of the Kuroshio/Oyashio Extensions on air–sea heat exchanges and storm-track activity as revealed in regional atmospheric model simulations for the 2003/4 cold season. *J. Climate*, **22**, 6536–6560, doi:10.1175/2009JCLI2910.1.

Takayabu, Y. N., S. Shige, W. Tao, and N. Hirota, 2010: Shallow and deep latent heating modes over tropical oceans observed with TRMM PR spectral latent heating data. *J. Climate*, **23**, 2030–2046, doi:10.1175/2009JCLI3110.1.

Tan, I., T. Storelvmo, and M. D. Zelinka, 2016: Observational constraints on mixed-phase clouds imply higher climate sensitivity. *Science*, **352**, 224–227, doi:10.1126/science.aad5300.

Tanimoto, Y., and S.-P. Xie, 2002: Inter-hemispheric decadal variations in SST, surface wind, heat flux and cloud cover over the Atlantic Ocean. *J. Meteor. Soc. Japan*, **80**, 1199–1219, doi:10.2151/jmsj.80.1199.

Tanimoto, Y., S.-P. Xie, K. Kai, H. Okajima, H. Tokinaga, T. Murayama, M. Nonaka, and H. Nakamura, 2009: Observations of marine atmospheric boundary layer transitions across the summer Kuroshio Extension. *J. Climate*, **22**, 1360–1374, doi:10.1175/2008JCLI2420.1.

Terai, C. R., S. A. Klein, and M. D. Zelinka, 2016: Constraining the low-cloud optical depth feedback at middle and high latitudes using satellite observations. *J. Geophys. Res.*, **121**, 9696–9716, doi:10.1002/2016JD025233.

Tokinaga, H., Y. Tanimoto, and S.-P. Xie, 2005: SST-induced surface wind variations over the Brazil-Malvinas confluence: Satellite and in situ observations. *J. Climate*, **18**, 3470–3482, doi:10.1175/JCLI3485.1.

Tokinaga, H., Y. Tanimoto, S.-P. Xie, T. Sampe, H. Tomita, and H. Ichikawa, 2009: Ocean frontal effects on the vertical development of clouds over the western North Pacific: In situ and satellite observations. *J. Climate*, **22**, 4241–4260, doi:10.1175/2009JCLI2763.1.

Tomita, H., T. Hihara, S. Kako, M. Kubota, and K. Kutsuwada, 2019: An introduction to J-OFURO3, a third-generation Japanese ocean flux data set using remote-sensing observations. *J. Oceanogr.*, **75**, 171–194, doi:10.1007/s10872-018-0493-x.

Tozuka, T., and M. F. Cronin, 2014: Role of mixed layer depth in surface frontogenesis: The Agulhas Return Current front. *Geophys. Res. Lett.*, **41**, 2447–2453, doi:10.1002/2014GL059624.

Trenberth, K. E., 1986: An assessment of the impact of transient eddies on the zonal flow during a blocking episode using localized Eliassen-Palm flux diagnosis. *J. Atmos. Sci.*, **43**, 2070–2087, doi:10.1175/1520-0469(1986)043⟨2070:AAOTIO⟩2.0.CO;2.

Tsushima, Y., and Coauthors, 2006: Importance of the mixed-phase cloud distribution in the control climate for assessing the response of clouds to carbon dioxide increase: A multi-model study. *Climate Dyn.*, **27**, 113–126, doi:10.1007/s00382-006-0127-7.

van der Dussen, J. J., S. R. de Roode, S. D. Gesso, and A. P. Siebesma, 2015: An LES model study of the influence of the free tropospheric thermodynamic conditions on the stratocumulus response to a climate perturbation. *J. Adv. Model. Earth Syst.*, **7**, 670–691, doi:10.1002/2014MS000380.

Wallace, J. M., T. P. Mitchell, and C. Deser, 1989: The influence of sea-surface temperature on surface wind in the eastern equatorial Pacific: Seasonal and interannual variability. *J. Climate*, **2**, 1492–1499, doi:10.1175/1520-0442(1989)002⟨1492:TIOSST⟩2.0.CO;2.

Wang, B., and Z. Fan, 1999: Choice of south Asian summer monsoon indices. *Bull. Amer. Meteor. Soc.*, **80**, 629–638, doi:10.1175/1520-0477(1999)080⟨0629:COSASM⟩2.0.CO;2.

Wang, B., R. Wu, and K.-M. Lau, 2001: Interannual variability of the Asian summer monsoon: Contrasts between the Indian and the Western North Pacific-East Asian monsoons. *J. Climate*, **14**, 4073–4090, doi:10.1175/1520-0442(2001)014⟨4073:IVOTAS⟩2.0.CO;2.

Wang, L., Y. Wang, A. Lauer, and S.-P. Xie, 2011: Simulation of seasonal variation of marine boundary layer clouds over the eastern Pacific with a regional climate model. *J. Climate*, **24**, 3190–3210, doi:10.1175/2010JCLI3935.1.

Wang, Y., S.-P. Xie, B. Wang, and H. Xu, 2005: Large-scale atmospheric forcing by southeast Pacific boundary layer clouds: A regional model study. *J. Climate*, **18**, 934–951, doi:10.1175/JCLI3302.1.

Watanabe, M., and M. Kimoto, 2000: Atmosphere- ocean thermal coupling in the North Atlantic: A positive feedback. *Quart. J. Roy. Meteor. Soc.*, **126**, 3343–3369, doi:10.1002/qj.49712657017.

Watanabe, M., and M. Kimoto, 2001: Corrigendum. *Quart. J. Roy. Meteor. Soc.*, **127**, 733–734, doi:10.1002/qj.49712757223.

Watt-Meyer, O., and D. M. W. Frierson, 2017: Local and remote impacts of atmospheric cloud radiative effects onto the eddy- driven jet. *Geophys. Res. Lett.*, **44**, 10 036–10 044, doi:10.1002/2017GL074901.

Weare, B. C., 2000: Near-global observations of low clouds. *J. Climate*, **13**, 1255–1268, doi:10.1175/1520-0442(2000)013⟨1255:NGOOLC⟩2.0.CO;2.

Webb, M., C. Senior, S. bony, and J. J. Morcrette, 2001: Combining ERBE and ISCCP data to assess clouds in the Hadley Centre, ECMWF and LMD atmospheric climate models. *Climate Dyn.*, **17**, 905–922, doi:10.1007/s003820100.

Webster, P. J., 2006: The coupled monsoon system. *The Asian Monsoon*, B. Wang, Eds., Springer, 3–66, doi:10.1007/3-540-37722-0.

Wielicki, B. A., B. R. Barkstrom, E. F. Harrison, R. B. Lee III, G. L. Smith, and J. E. Cooper, 1996a: Clouds and the Earth's Radiant Energy System (CERES): An Earth observing system experiment. *Bull. Amer. Meteor. Soc.*, **77**, 853–868, doi:10.1175/1520-0477(1996)077⟨0853:CATERE⟩2.0.CO;2.

Wielicki, B. A., B. R. Barkstrom, E. F. Harrison, R. B. Lee III, G. L. Smith, and J. E. Cooper, 1996b: Clouds and the Earth's Radiant Energy System (CERES): An Earth observing system experiment. *Bull. Amer. Meteor. Soc.*, **77**, 853–868, doi:10.1175/1520-0477(1996)077⟨0853:CATERE⟩2.0.CO;2.

Williams, E., and N. Renno, 1993: An analysis of the conditional instability of the tropical atmosphere. *Mon. Wea. Rev.*, **121**, 21–36, doi:10.1175/1520-0493(1993)121⟨0021:AAOTCI⟩2.0.CO;2.

Wood, R., 2012: Stratocumulus clouds. *Mon. Wea. Rev.*, **140**, 2373–2423, doi:10.1175/MWR-D-11-00121.1.

Wood, R., and C. S. Bretherton, 2006: On the relationship between stratiform low cloud cover and lower-tropospheric stability. *J. Climate*, **19**, 6425–6432, doi:10.1175/JCLI3988.1.

Wu, G., and Y. Liu, 2003: Summertime quadruplet heating pattern in the subtropics and the associated atmospheric circulation. *Geophys. Res. Lett.*, **30**, 1201, doi:10.1029/2002GL016209.

Xie, S.-P., H. Annamalai, F. A. Schott, and J. P. McCreary Jr., 2002: Structure and mechanisms of South Indian Ocean climate variability. *J. Climate*, **15**, 864–878, doi:10.1175/1520-0442(2002)015⟨0864:SAMOSI⟩2.0.CO;2.

Xie, S.-P., and S. G. H. Philander, 1994: A coupled ocean-atmosphere model of relevance to the ITCZ in the eastern pacific. *Tellus*, **46A**, 340–350, doi:10.3402/tellusa.v46i4.15484.

Xu, H., S.-P. Xie, and Y. Wang, 2005: Subseasonal variability of the southeast Pacific stratus cloud deck. *J. Climate*, **18**, 131–142, doi:10.1175/JCLI3250.1.

Xu, H., Y. Wang, and S. Xie, 2004: Effects of the Andes on eastern Pacific climate: A regional atmospheric model study. *J. Climate*, **17**, 589–602, doi:10.1175/1520-0442(2004)017⟨0589:EOTAOE⟩2.0.CO;2.

Yokoi, T., T. Tozuka, and T. Yamagata, 2008: Seasonal variation of the Seychelles Dome. *J. Climate*, **21**, 3740–3754, doi:10.1175/2008JCLI1957.1.

Yokoi, T., T. Tozuka, and T. Yamagata, 2009: Seasonal variations of the Seychelles Dome simulated in the CMIP3 models. *J. Phys. Oceanogr.*, **39**, 449–457, doi:10.1175/2008JPO3914.1.

Yu, L., Z. Zhang, S. Zhong, M. Zhou, Z. Gao, H. Wu, and B. Sun, 2011: An inter-comparison of six latent and sensible heat flux products over the Southern Ocean. *Polar Research*, **30**, 10 167, doi:10.3402/polar.v30i0.10167.

Yu, J.-Y., and C. R. Mechoso, 1999: Links between annual variations of Peruvian stratocumulus clouds and of SST in the eastern equatorial Pacific. *J. Climate*, **12**, 3305–3318, doi:10.1175/1520-0442(1999)012⟨3305:LBAVOP⟩2.0.CO;2.

Yuan, C., and T. Yamagata, 2014: California Niño/Niña. *Sci. Rep.*, **4**, doi:10.1038/srep04801.

Yuan, T. L., L. Oreopoulos, M. Zelinka, H. Yu, J. R. Norris, M. Chin, S. Platnick, and K. Meyer, 2016: Positive low cloud and dust feedbacks amplify tropical North Atlantic Mutidecadal Oscillation. *Geophys. Res. Lett.*, **43**, 1349–1356, doi:10.1002/2016GL067679.

Zuidema, P., and Coauthors, 2016: Challenges and prospects for reducing coupled climate model SST biases in the eastern tropical Atlantic and Pacific Oceans: The U.S. CLIVAR Eastern Tropical Oceans Synthesis Working Group. *Bull. Amer. Meteor. Soc.*, **97**, 2305–2327, doi:10.1175/BAMS-D-15-00274.1.